Classical and quantum scattering in optical systems
Puentes, G.

Citation
Puentes, G. (2007, May 16). *Classical and quantum scattering in optical systems*. *Casimir PhD Series*. Physics Department/ Huygens Laboratory/ Quantum Optics Group, Faculty of Mathematics and Natural Sciences, Leiden University. Retrieved from https://hdl.handle.net/1887/11956

Classical and quantum scattering in optical systems

PROEFSCHIRFT

ter verkrijging van
de graad van Doctor aan de Universiteit Leiden,
op gezag van Rector Magnificus Prof. Mr. P. F. van der Heijden,
volgens besluit van het College voor Promoties
te verdedigen op woensdag 16 mei 2007
klokke 16.15 uur

door

Graciana Puentes
geboren te Buenos Aires (Argentina)
op 3 januari 1977

Promotiecommissie:

Promotor: Prof. dr. J. P. Woerdman
Referent: Prof. dr. G. Nienhuis
Leden: Prof. dr. A. Lagendijk (Universiteit van Amsterdam / AMOLF)
          Dr. R. J. C. Spreeuw   (Universiteit van Amsterdam)
          Prof. dr. G. 't Hooft
          Dr. M. P. van Exter
          Prof. dr. C. W. J. Beenakker
          Prof. dr. J. M. van Ruitenbeek

The image on the cover shows the exit basin diagram associated with light rays scattered by an optical cavity with a stochastic ray-splitting mechanism. The fractal nature of the basins is a typical feature of chaotic scattering. This is explained in detail in Chapter 3 (this Thesis).

Contents

Introduction

1.1 Classical scattering in optical systems

Light scattering is a very broad topic which has a scientific history of over a century [1]. Generally speaking, light is scattered whenever it propagates in a material medium, because of its interaction with the molecules constituting the medium, which act as scattering centers. As a consequence, most of the light that we observe in daily life is scattered light. However, the arrangement of these molecules strongly determines the effectiveness of the scattering for a given input wave. For instance, in a perfect crystal the molecular scattering centra are so orderly arranged that the scattered output waves interfere destructively in such a way that only the propagation velocity of the incident wave is changed. Conversely, in a gas or a fluid, the statistical fluctuations of the molecular arrangement can cause significant scattering. Depending on the nature of the interaction processes, light can be scattered elastically or inelastically [2]. In elastic (Rayleigh) scattering, the frequency of the scattered light is equivalent to that of the incident light. On the other hand, inelastic (Raman) scattering results in scattered light of different frequency than the incident. In this Thesis we will concentrate on elastic scattering processes where the frequency of the incident light is conserved. Additionally, we will restrict our analysis to linear scattering processes, where this linearity refers to the amplitude of the light field. A scattering process can be consider linear when, for a sum of incident input waves, the scattered output wave is a linear superposition of the incident ones. Such linear processes can be described by a scattering matrix, which maps input and output waves. In this context, we take a broad definition of an elastic light scattering process; namely, any optical process that changes the direction of the wave-vector of the light. Thus a scattering process can range from Rayleigh scattering by a point particle to refraction by a lens.

Formally, light can be described by an electromagnetic field satisfying Maxwell's equa-

tions. The interaction of such a field with the molecules in a material medium can modify its spatial distribution, frequency or polarization. The exact way in which these degrees of freedom are modified depend on the specific properties of the scattering medium, which can be described at different length scales. For example in Ref. [3], three levels of description are identified based upon three length scales. These levels are classified as macroscopic: on scales much larger than the mean free path l, mesoscopic: on scales of the order of the mean free path l and microscopic: on scales comparable to the wavelength of the light λ. However, in this Thesis we are exclusively interested in the changes produced by the scattering process on the electromagnetic field, thus regarding the scattering medium as a black box. Within such approach, the medium can be described by a phenomenological set of parameters, usually arranged to form a matrix. The size and properties of such matrix depend on the particular degrees of freedom of the field one is interested in. For example, when dealing with polarization degrees of freedom, the scattering process can be represented by a 4×4 real-valued matrix, the so called Mueller matrix [4]. On the other hand, when dealing with propagation of rays of light through an astigmatic paraxial optical device, the information about the medium is contained in a 2×2 real-valued symplectic matrix, the so called *ABCD* matrix [5]. In the following subsections we give explicit expressions for the Mueller matrix and the *ABCD* matrix of a generic optical system, which are used in the context of polarization scattering and ray scattering, respectively.

1.1.1 Polarization scattering

The basic elements of a classical light scattering experiment are an incident field which illuminates a scattering medium and a detector which measures the intensity of the scattered field (see Fig. 1.1). For a single spatial mode of the incident field ($\mathbf{k}_{\text{in}}$), here represented by a plane-wave propagating in a given direction $\hat{k}_{\text{in}}$, the effect of a single scattering event is to change the direction of propagation of the field, so that the scattered field is in the output plane-wave mode ($\mathbf{k}_{\text{out}}$) characterized by the direction $\hat{k}_{\text{out}}$. Here $|\mathbf{k}_{\text{in}}| = |\mathbf{k}_{\text{out}}|$, since we are considering elastic scattering processes. The electric field, which determines the polarization,
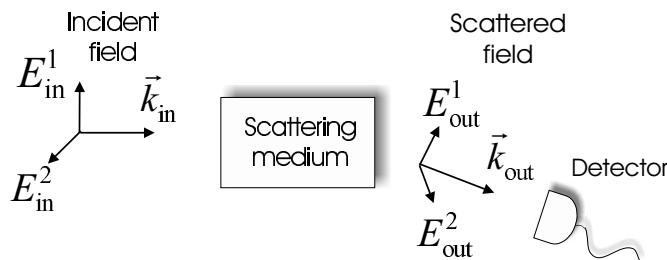

Figure 1.1: *Geometry for describing a single mode scattering process. The incident and scattered fields are described by plane-waves, which are characterized by their directions of propagation $\hat{k}_{\text{in}}$ and $\hat{k}_{\text{out}}$. After the scattering event takes place, the scattered field intensity is measured at the detector.*

is here represented by the complex vector $\mathbf{E} \in \mathbb{C}^2 : \mathbf{E} = E_1 \hat{1} + E_2 \hat{2}$, on a plane orthogonal to the direction of propagation $\hat{k}$. Note that the three real-valued unit vectors $\{\hat{1}, \hat{2}, \hat{k}\}$ define an orthogonal Cartesian frame. Since the polarization $\mathbf{E}$ is a transverse degree of freedom, a transformation on the spatial properties of the light beam (by scattering) is always accompanied by an intrinsic transformation on the polarization of the light beam. Any linear transformation of the polarization properties of the beam by scattering can be represented in the Mueller-Stokes formalism. Within this formalism, the electric field is fully specified by the real-valued 4-dimensional Stokes vector $\mathbf{S} \in \mathbb{R}^2 : \mathbf{S} = (S_0, S_1, S_2, S_3)$; namely:

$$
\begin{aligned}
S_0 &\equiv |E_1|^2 + |E_2|^2 \propto I \\
S_1 &\equiv |E_2|^2 - |E_1|^2 \propto I_{0°} - I_{90°} \\
S_2 &\equiv E_1 E_2^* + E_2 E_1^* \propto I_{45°} - I_{-45°} \\
S_3 &\equiv i(E_1 E_2^* - E_2 E_1^*) \propto I_{RHC} - I_{LHC}.
\end{aligned}
$$

$$(1.1)$$

If we identify the directions $\hat{1}$ and $\hat{2}$ with vertical ($90°$) and horizontal ($0°$) polarizations respectively, then S_0 is proportional to the total intensity of the beam, S_1 is proportional to the difference in intensities between horizontal and vertical linearly polarized components, S_2 is proportional to the difference in intensities between linearly polarized components oriented at $45°$ and $-45°$ and S_3 is proportional to the difference in intensities between right hand *RHC* and left hand *LHC* circularly polarized components. It should be stressed that the real valued 4-dimensional Stokes vector contains the same information as the complex valued 2×2 coherency matrix J [6]. The advantage of the Mueller-Stokes formalism is that it is directly related with measurable quantities, i.e., intensities. The only restriction for a Stokes vector to represent a physical polarization state is that $\sum_i (S_i)^2 \leq (S_0)^2$ ($i = 1, 2, 3$). Additionally, any optical system, which transforms an input Stokes vector $\mathbf{S}_{in}$ into an output Stokes vector $\mathbf{S}_{out}$, can be characterized by a 4×4 Mueller matrix (M), whose 16 real elements map the polarization state of the input and output beams by:

$$\mathbf{S}_{out} = M\mathbf{S}_{in}. \tag{1.2}$$

In this Thesis we considered only passive or non-amplifying optical media such that the output intensity is not larger than the input intensity, in other words for all our scattering media $S_{0,out} \leq S_{0,in}$. However, it should be noted that an active medium, i.e., a medium with gain, can in principle also be represented by a Mueller matrix. This is because classically, a medium with gain, is formally equivalent to a medium with absorption, up to a sign, and scattering media with polarization dependent absorption, i.e., dichroic scattering media, are fully described in the Mueller-Stokes formalism.

The Mueller-Stokes formalism is suitable for a single spatial mode description of the field, i.e., for paraxial angles of propagation of the field. In this context, depolarization mainly occurs due to coupling of polarization degrees of freedom with temporal domain, for instance by propagation through dynamic media. However, it is possible to extend this formalism to the multi-spatial-mode case, this is explained in detail in Chapter 4. When the scattering process involves many modes (either spectral or spatial) of the field and the polarization

properties of the outgoing beam are measured with a mode-insensitive device, the scattered field might appear partially depolarized. The degree of polarization (P_F) of a light beam is defined by

$$P_F = \frac{\sqrt{(S_1)^2 + (S_2)^2 + (S_3)^2}}{S_0},$$ (1.3)

where $0 \leq P_F \leq 1$. Fully polarized light has $P_F = 1$ while unpolarized light has $P_F = 0$, the intermediate values for P_F correspond to partially polarized light. The main mechanism of depolarization that we analyze in this Thesis is given by the coupling of polarization and spatial degrees of freedom. A typical example of this is the case of a beam of light initially prepared in a single plane-wave mode ($\mathbf{k}_{\text{in}}$) that is incident on an inhomogeneous medium. Due to the spatial inhomogeneities in the medium, the beam suffers multiple scattering and, as a result, it emerges as a (partially) incoherent superposition of many plane-waves ($\mathbf{k}_{\text{out}}$). Even when each of the output modes is fully polarized, the output beam appears to be (partially) depolarized when its spatial information is averaged out in a multi-mode detection set-up.

1.1.2 Ray scattering

Figure 1.2: *The input canonical variables* $(q_{\text{in}}, \theta_{\text{in}})$, *specifying a ray on a reference plane* R_1, *are mapped by the ABCD matrix into the output canonical variables* $(q_{\text{out}}, \theta_{\text{out}})$ *of a ray on a reference plane* R_2.

In the short wavelength limit, a ray-like beam is fully described by two canonical variables; namely, its position q (on a given reference plane) and its slope θ (see Fig. 1.2). Additionally, the change in q and θ of an optical ray upon propagation through a wide variety of optical scattering devices can be written, in the paraxial limit and for a single transverse dimension, in terms of the 2×2 *ABCD* or ray matrix [5] by:

$$\begin{pmatrix} q_{\text{out}} \\ \theta_{\text{out}} \end{pmatrix} = \begin{pmatrix} A & B \\ C & D \end{pmatrix} \begin{pmatrix} q_{\text{in}} \\ \theta_{\text{in}} \end{pmatrix}.$$ (1.4)

It should be stressed that the only condition for an *ABCD* matrix to represent a physical transformation upon a ray is that its determinant should be equal to one (i.e., a symplectic transformation). Therefore, within this limit, an optical transformation can range from deflection of light by a particle to refraction of light by a lens. In Chapter 2 and Chapter 3 we analyzed the dynamical properties of an optical cavity with a stochastic beam splitter. The

round trip of a ray inside such a cavity can be represented, in the paraxial approximation, by an *ABCD* matrix and can thus be interpreted as a linear optical ray scattering process.

1.2 Quantum scattering in optical systems

The quantum aspects of scattering in optical systems that are highlighted in our work refer to the quantum nature of the light that is incident on different scattering media. At the single-photon level, the quantum nature of light is revealed by the quantum field fluctuations, which can be seen as a consequence of the Heisenberg uncertainty relations between the electric and magnetic fields [7]. In this regard, the effect of multiple scattering on single-photon spatial correlations has been recently investigated in Ref. [8]. For photon pairs the quantum nature of light can also manifest itself by the mutual entanglement between the two photons belonging to the pair; this topic is addressed in this Thesis.

1.2.1 Entangled photons

A pair of photons is considered 'entangled' when a measurement on one of the two photons belonging to the pair completely determines the outcome of measurements on the other one, regardless of the distance between the photons. These non-local correlations, referred to as quantum entanglement, can not be explained in terms of any local classical theory and have puzzled many physicist starting by Einstein, Podolosky and Rosen [9], in 1935. In our scattering experiments with quantum light, we have concentrated on entangled photon pairs, where the incident state of light is entangled in the polarization degrees of freedom. A typical example is the polarization-singlet Bell state:

$$|\psi^-\rangle = \frac{|H_1 V_2\rangle - |V_1 H_2\rangle}{\sqrt{2}}, \tag{1.5}$$

where 1 and 2 label the two photons belonging to the pair, and (H, V) label horizontal and vertical polarizations, respectively. In fact, this state contains maximal information about the correlations of the two photons but minimal information about the polarization state of each individual photon. Thus if we measure the polarization of photon 1, and we find that it is vertical V, then we automatically know that the outcome of a similar measurement on photon 2 would yield H. Note that the anti-correlation between the polarization state of each photon belonging to the singlet is valid in *any* polarization basis.

1.2.2 Light scattering with entangled photons

Quantum theory predicts that the quantum correlations between entangled photons should be maintained over arbitrary distances. This prediction was verified on free-space propagation over distances of up to 144 km [10, 11], with polarization entangled photons. Moreover, the robustness of polarization entanglement has also been proven upon some particular scattering processes [12]. Generally speaking, scattering processes should not affect polarization entanglement as long as they are linear (thus describable by a scattering matrix) and as long

as the photons are detected in a single spatial mode [13, 14]. Therefore, it appears to be relevant to characterize entanglement decay upon linear scattering processes in combination with multi-mode detection, and that is indeed the central topic of this Thesis.

The main concept behind light scattering with polarization entangled photons is that a scattering process can couple polarization and spatial degrees of freedom of light. The details of this coupling depend on the specific scattering medium. If the scattered photons are then detected in a momentum insensitive way (multi-mode detection), all the spatial information of the scattering process encoded in the photons is averaged or traced over, leaving each photon in a mixed polarization state. As one might expect, this transition from pure to mixed state reduces the degree of entanglement; this has been theoretically explored in recent papers [13, 14].

The output polarization state of the scattered photons can be calculated once we know the phenomenological polarization matrix (i.e., the Mueller matrix M) characterizing the scattering medium. For an input state given by a pair of photons, initially prepared in the polarization singlet state

$$\rho_{\text{in}} = |\psi^-\rangle\langle\psi^-|, \tag{1.6}$$

and for a local scattering medium, i.e., a medium acting on a single photon of the entangled pair, the scattered photon-pair, which is in the mixed polarization state ρ_{out}, can be written in a *reshuffled* basis, here denoted by the superscript (R), as [15]:

$$\rho_{\text{out}}^R = \mathscr{M}\rho_{\text{in}}^R, \tag{1.7}$$

where the matrix $\mathscr{M}$ maps the input and output polarization states of the photon pairs. $\mathscr{M}$ is linearly related to the classical Mueller matrix M of the scattering medium, this is explained in detail in Chapter 8.

Eq.(1.7) suggests that the study of a local scattering process acting on a pair of photons is an alternative (and rather sophisticated) way of studying a depolarizing process. In other words, it is a non-standard way of measuring the Mueller matrix M (or $\mathscr{M}$) of a depolarizing medium. We stress that the fact that a scattering experiment with two-photon light reveals the same amount of information on the scattering medium as a similar experiment with a classical beam of light is only true as long as we analyze, as we do in this Thesis, *local* scattering media. That is, scattering media located on the path of a single photon of the entangled pair. Nevertheless, although we only experimented with local media, our mathematical formalism still applies to bi-local scattering media, which can be written as the (outer) product of two Mueller matrices acting on each photon of the pair, and to non-local scattering media, which can be written as an inseparable (two-photon) Mueller matrix [15].

Finally, it is important to stress that one of the main goals in our scattering experiments with entangled photons was to engineer (mixed) quantum states of light in a controllable way (see Chapter 7 and Chapter 8). As a consequence, in most of our experiments with quantum light, our target is the two-photon scattered state ρ_{out} rather than the classical Mueller matrix $\mathscr{M}$. This is what we consider novel in our approach.

1.3   Thesis overview

In this Thesis we analyzed the effect of a large variety of linear scattering processes both on classical light (Chapter 4-5) and on two-photon quantum light (Chapter 6-9). The main part of this analysis refers to the polarization degrees of freedom of scattered light where the medium parameters are phenomenologically described within the Mueller matrix formalism. The main tool used for this characterization is multi-spatial-mode optical polarization tomography, both in its classical and quantum versions.

Additionally, in fact as a starter for this Thesis, we have numerically investigated dynamical properties of ray scattering in optical cavities by using Hamiltonian optics (Chapter 2-3). The paraxial description of light rays in such optical cavities is described within the *ABCD* matrix formalism.

We describe the contents of the Chapters in more detail below:

- In Chapter 2 we report a numerical investigation of the *paraxial* ray dynamics of light scattered by an optical cavity with a stochastic ray-splitting mechanism. We show the results obtained for the paraxial map of the system, applying standard tools from non-linear dynamics. A discussion on the mixing properties of the system and their relation with the Kolmogorov-Sinai (KS) entropy is included.

- In Chapter 3 we presents the *exact* ray dynamics in an optical cavity with a ray splitting mechanism, similar to the one introduced in Chapter 2. By using exact Hamiltonian optics, we show that such a simple scattering device presents a surprisingly rich chaotic ray dynamics.

- In Chapter 4 we describe the theoretical background related to our experiments on classical light depolarization due to multi-mode scattering. The key theoretical concept we introduce is the effective Mueller matrix, which describes our spatial multi-mode detection set-up.

- In Chapter 5 we show experimental results on classical light depolarization due to multi-mode scattering. By means of polarization tomography, we characterize the depolarizing power and the polarization entropy of a broad class of optically scattering media.

- In Chapter 6 we report experimental results on a controllable source of spatial decoherence for polarization entangled photons, based upon commercially available wedge depolarizers. A full characterization of the scattered states, by means of quantum tomography, shows that such a scattering device can be used for synthesizing Werner-like states on demand.

- In Chapter 7 we present experimental results on the effect of different scattering process on polarization entangled photons. The scattering media are grouped in isotropic, birefringent and dichroic scattering. We compare the experimental results with a phenomenological model based upon the description of a scattering process as a quantum map.

- In Chapter 8 we present a full theoretical framework for the description of a scattering process as a quantum map. Within this framework, we show how scattering processes

can be used for entangled-mixed state engineering. We report an experimental scheme suitable for maximally entangled mixed states engineering and the corresponding experimental results.

- In Chapter 9 we review some of our experimental results on multi-mode scattering of entangled photon pairs and their description in terms of trace-preserving and non-trace-preserving quantum maps. We show that non-trace-preserving quantum maps can lead to apparent violations of causality, when the two-photon states are post-selected by coincidence measurements. A brief discussion on relativistic causality is included.

With the exceptions of Chapters 1 and 4, all the Chapters contained in this Thesis are based on independent publications and can be read separately. As a consequence there is some overlap between them. Although within a Chapter each physical quantity has a unique symbol, some symbols are used for different physical quantities in different Chapters.

CHAPTER 2

Paraxial ray dynamics in an optical cavity with a beam-splitter.

In this Chapter [1] we present a numerical investigation of the ray dynamics in an optical cavity when a ray splitting mechanism is present; we focus mainly on the paraxial limit. The cavity is a conventional two-mirror stable resonator and the ray splitting is achieved by inserting an optical beam splitter perpendicular to the cavity axis. We show the results obtained for the paraxial map of the system [16], applying standard tools from non-linear dynamics, such as Poincaré Surface of Section (SOS), exit basin diagrams, escape rate and Lyapunov exponents. Furthermore, a discussion about the mixing properties of the system and their relation with the Kolmogorov-Sinai (KS) entropy is included. In the paraxial limit the ray dynamics is irregular and both the Lyapunov exponent and the KS entropy are positive; however, chaos does not occur.

---

[1]Based on G. Puentes, A. Aiello and J. P. Woerdman, Phys. Rev. E **69**, 036209 (2004).

2.1   Introduction

A beam splitter (BS) is an ubiquitous optical device in wave optics experiments, used e.g., for optical interference, homodyning, etc. In the context of geometrical optics, the action of a BS is to split a light ray into a transmitted or a reflected ray. Ray splitting provides a useful mechanism to generate chaotic dynamics in pseudointegrable [17] and soft-chaotic [18–21] closed systems. In this Chapter we exploit the ray splitting properties of a BS in order to build an open paraxial cavity which shows irregular ray dynamics as opposed to the regular dynamics displayed by a paraxial cavity when the BS is absent.
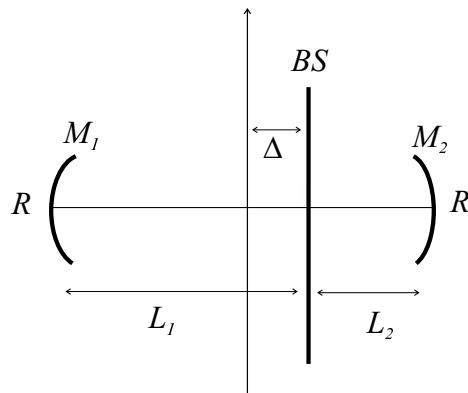
Figure 2.1: *Schematic diagram of the cavity model. Two subcavities of length L_1 and L_2 are coupled by a BS. The total cavity is globally stable for $L = L_1 + L_2 < 2R$. $\Delta = L_1 - L/2$ represents the displacement of the BS with respect to the center of the cavity.*

Optical cavities can be classified as *stable* or *unstable* depending on the focussing properties of the elements that compose it [5]. An optical cavity formed by 2 concave mirrors of radii R separated by a distance L is stable when $L < 2R$ and unstable otherwise. If a light ray is injected inside the cavity through one of the mirrors it will remain confined indefinitely inside the cavity when the configuration is stable but it will escape after a finite number of bounces when the cavity is unstable (this number depends on the degree of instability of the system). Both stable and unstable cavities have been extensively investigated since they form the basis of laser physics [5]. Our interest is in a composite cavity which has both aspects of stability and instability. The cavity is made by two identical concave mirrors of radii R separated by a distance L, where $L < 2R$ so that the cavity is globally stable. We then introduce a beam splitter (BS) inside the cavity, oriented perpendicular to the optical axis (Fig. 2.1). In this way the BS defines two subcavities. The main idea is that depending on the position of the BS the left (right) subcavity becomes *unstable* for the reflected rays when L_1 (L_2) is bigger than R, whereas the cavity as a whole remains always *stable* ($L_1 + L_2 < 2R$) (Fig. 2.2).

Our motivation to address this system originates in the nontrivial question whether there will be a balance between trapped rays and escaping rays. The trapped rays are those which bounce infinitely long in the stable part of the cavity, while the escaping ones are those which stay for a finite time, due to the presence of the unstable subcavity. If such balance exists it could eventually lead to transient chaos since it is known in literature that instability (positive
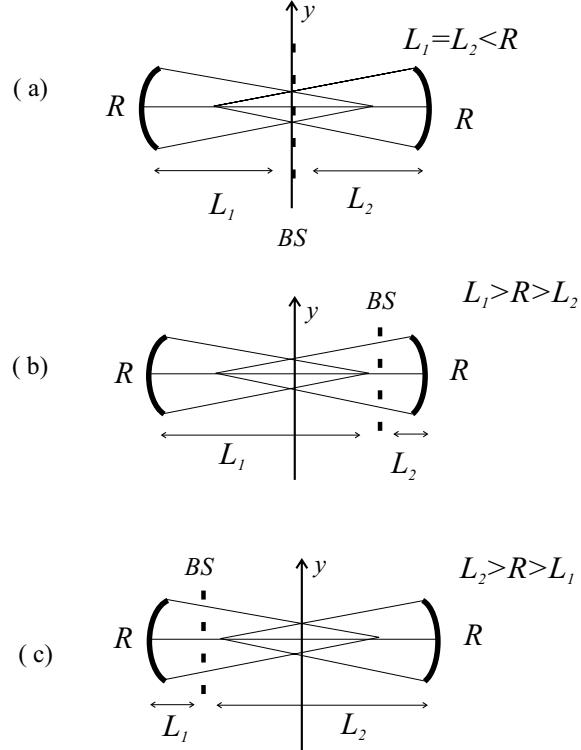
Figure 2.2: *The different positions of the beam splitter determine the nature of the subcavities. In (a) the BS is in the middle, so the 2 subcavities are stable, in (b) the left cavity is unstable and the right one is stable, and (c) the unstable (stable) cavity is on the right (left) (b).*

Lyapunov exponents) and mixing (confinement inside the system) form the skeleton of chaos [22].

The BS is modelled as a stochastic ray splitting element [18] by assuming the reflection and transmission coefficients as random variables. Within the context of wave optics this model corresponds to the neglect of all interference phenomena inside the cavity; this would occur, for instance when one injects inside the cavity a wave packet (or cw broad band light) whose longitudinal coherence length is very much shorter than the smallest characteristic length of the cavity. The stochasticity is implemented by using a Monte Carlo method to determine whether the ray is transmitted or reflected by the BS [18]. When a ray is incident on the ray splitting surface of the BS, it is either transmitted through it with probability p or reflected with probability $1 - p$, where we will assume $p = 1/2$, i.e., we considered a 50/50 beam splitter (Fig. 2.3). We then follow a ray and at each reflection we use a random number generator with a uniform distribution to randomly decide whether to reflect or transmit the incident ray.
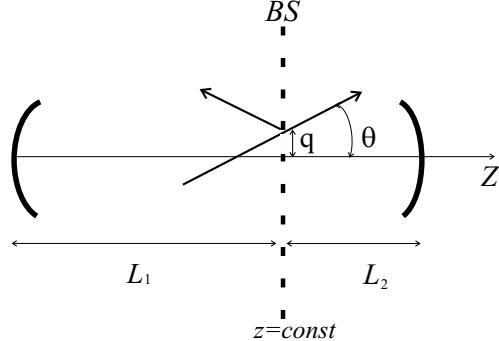
Figure 2.3: *A ray on a reference plane ($z = const$) perpendicular to the optical axis (Z) is specified by two parameters: the height q above the optical axis and the angle θ between the direction of propagation and the same axis. When a ray hits the surface of the BS, which we choose to coincide with the reference plane, it can be either reflected or transmitted with equal probability (p). For a $50/50$ beam splitter $p = 1/2$.*

Our system bears a close connection with the stability of a periodic guide of paraxial lenses as studied by Longhi [30]. While in his case a *continuous* stochastic variable ε_n represents a perturbation of the periodic sequence along which rays are propagated, in our case we have a *discrete* stochastic parameter p_n which represents the response of the BS to an incident ray. As will be shown in section 2.2, this stochastic parameter can take only two values, either +1 for transmitted rays or -1 for reflected rays; in this sense, our system (displayed as a paraxial lens guide in Fig. 2.4) allows a surprisingly simple realization of a bimodal stochastic dynamics.

2.2   Ray dynamics and the paraxial map

The time evolution of a laser beam inside a cavity can be approximated classically by using the ray optics limit, where the wave nature of light is neglected. Generally, in this limit the propagation of light in a uniform medium is described by rays which travel in straight lines, and which are either sharply reflected or refracted when they hit a medium with a different refractive index. To fully characterize the trajectory of a ray in a strip resonator or in a resonator with rotational symmetry around the optical axis, we choose a reference plane $z = constant$ (perpendicular to the optical axis $\hat{z}$), so that a ray is specified by two parameters: the height q above the optical axis and the angle θ between the trajectory and the same axis. Therefore we can associate a ray of light with a two dimensional vector $\vec{r} = (q, \theta)$. This is illustrated in the two mirror cavity show in Fig. 2.3, where the reference plane has been chosen to coincide with the beam splitter (BS). Given such a reference plane z, which is also called Poincaré Surface of Section (SOS) [23], a round trip (evolution between two successive reference planes) of the ray inside the cavity can be calculated by the monodromy matrix M_n, in other words $\vec{r}_{n+1} = M_n \vec{r}_n$, where the index n determines the number of round trips. The monodromy matrix M_n describes the linearized evolution of a ray that deviates from a

reference periodic orbit. A periodic orbit is said to be *stable* if $|\mathrm{Tr}M_n| < 2$. In this case nearby rays oscillate back and forth around the stable periodic orbit with bounded displacements both in q and θ. On the other hand when $|\mathrm{Tr}M_n| \geq 2$ the orbit is said to be unstable and rays that are initially near this reference orbit become more and more displaced from it.

For paraxial trajectories, where the angle of propagation relative to the axis is taken to be very small (i.e., $\sin(\theta) \cong \tan(\theta) \cong \theta$), the reference periodic trajectory coincides with the optical axis and the monodromy matrix is identical to the ABCD matrix of the system. The ABCD matrix or paraxial map of an optical system is the simplest model one can use to describe the discrete time evolution of a ray in the optical system [5]. Perhaps the most interesting and important application of ray matrices comes in the analysis of periodic focusing (PF) systems in which the same sequence of elements is periodically repeated many times down in cascade. An optical cavity provides a simple way of recreating a PF system, since we can think of a cavity as a periodic series of lenses (see Fig. 2.4). In the framework of geometric ray optics, PF systems are classified, as are optical cavities, as either stable or unstable.
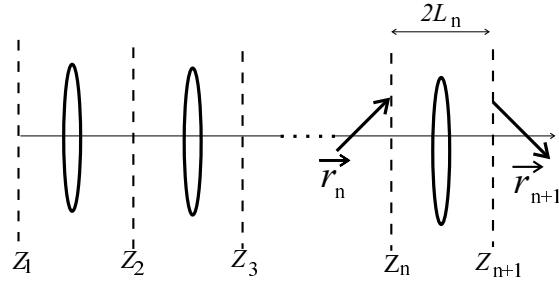
Figure 2.4: *A ray bouncing inside an optical cavity can be represented by a sequence of lenses of focus $f = 2/R$, followed by a free propagation over a distances L_n. Due to the presence of the BS, the distance L_n varies stochastically between L_1 or L_2.*

Without essential loss of generality we restrict ourselves to the case of a symmetric cavity (i.e., two identical spherical mirrors of radius of curvature R). We take the SOS coincident with the surface of the BS. After intersecting a given reference plane z_i, a transmitted (reflected) ray will undergo a free propagation over a distance L_2 (L_1), followed by a reflection on the curved mirror M_2 (M_1), and continue propagating over the distance L_2 (L_1), to hit the surface of the beam splitter again at z_{i+1}. In Fig. 2.4 the sequence of z_i represents the successive reference planes after a round trip. In the paraxial approximation each round trip (time evolution between two successive intersections of a ray with the beam splitter) is represented by:

$$\begin{aligned} q_{n+1} &= A_n q_n + B_n \theta_n, \\ \theta_{n+1} &= C q_n + D_n \theta_n, \end{aligned} \tag{2.1}$$

where

$$A_n = 1 - 2L_n/R, \qquad B_n = 2L_n(1 - L_n/R),$$

$$C = -2/R, \qquad D_n = 1 - 2L_n/R$$

and

$$L_n = \frac{L + p_n a}{2}.$$

We have defined $L = L_1 + L_2$ and $a = L_2 - L_1$; the stochastic parameter p_n is distributed equally among -1 and $+1$ for our 50/50 BS, and determines whether the ray is transmitted ($p_n = 1$) or is reflected ($p_n = -1$).

The elements of the ABCD matrix depend on the index n because of the stochastic response of the BS, which determines the propagation for the ray in subcavities of different length (either L_1 or L_2). In this way a random sequence of reflections ($p_n = 1$) and transmissions ($p_n = -1$) represents a particular geometrical realization of a focusing system. If we want to study the evolution of a set of rays injected in the cavity with different initial conditions (q_0, θ_0), we have two possibilities, either use the *same* random sequence of reflections and transmissions for all rays in the set or use a *different* random sequence for each ray. In the latter case, we are basically doing an ensemble average over different geometrical configurations of focusing systems. As we shall see later it is convenient, for computational reasons, to adopt the second method.

The paraxial map of Eq. (2.1) describes an unbounded system. That is, a system for which rays are allowed to go infinitely far from the cavity axis. In order to describe a physical paraxial cavity we have to keep the phase space bounded, i.e., it is necessary to artificially introduce boundaries for the position and the angle of the ray [31]. The phase space boundaries that we have adopted to decide whether a ray has escaped after a number of bounces or not are the beam waist (w_0) and the diffraction half-angle (Θ_0) [5] of a gaussian beam confined in a globally stable two-mirror cavity. Measured at the center of the cavity, the waist and the corresponding diffraction half-angle result in:

$$w_0^2 = \frac{L \lambda_{light}}{\pi} \sqrt{\frac{2R - L}{4L}} \tag{2.2}$$

$$\Theta_0 = \arctan\left(\frac{\lambda_{light}}{\pi w_0}\right) \tag{2.3}$$

Where we refer to the optical wavelength as λ_{light} in order to avoid confusion with the Lyapunov exponent λ. For our cavity configuration we assume $R = 0.15$ m, $L = 0.2$ m and $\lambda_{light} = 500$ nm, from which follows that $w_0 = 5.3 \times 10^{-5}$ m and $\Theta_0 = 0.15 \times 10^{-3}$ rad. One should keep in mind that this choice is somewhat arbitrary and other choices are certainly possible. The effect of this arbitrariness on our results will be discussed in detail in subsection 2.3.4.

In the next section we report several dynamical quantities that we have numerically calculated for paraxial rays in this system, using the map described above (Eq. 2.1). The behavior of these quantities; namely, the SOSs, the exit basins, the Lyapunov exponent and the escape rate, is analyzed as a function of the displacement (Δ) of the BS with respect to the center of the cavity (see Fig. 2.1).

2.3 Numerical results

2.3.1 Poincaré surface of section (SOS)

We have first calculated the SOS for different positions of the BS. In order to get a qualitative idea of the type of motion, we have chosen as transverse phase space variables $y = q$ and $v_y = \sin(\theta) \approx \theta$. The successive intersections of a trajectory with initial transverse coordinates $q_0 = 1 \times 10^{-5}$ m, $\theta_0 = 0$ are represented by the different black points in the surface of section. The different SOSs are shown in Fig. 2.5. In Fig. 2.5 (a) we show the SOS for $\Delta = 0$, while in (b) $\Delta = 1 \times 10^{-3}$ m and in (c) $\Delta = 2 \times 10^{-2}$ m. In (a) it is clear that the motion is completely regular (non-hyperbolic); the on-axis trajectory represents an elliptic fixed point for the map. In (b), where the BS is slightly displaced from the center ($\Delta = 1 \times 10^{-3}$ m) we can see that this same trajectory becomes unstable because of the presence of the BS, and spreads over a finite region of the phase space to escape after a large number of bounces ($n = 5 \times 10^4$). In this case we may qualify the motion as azimuthally ergodic. The fact that the ray-splitting mechanism introduced by the BS produces ergodicity is a well known result [18] for a closed billard. We find here an analogue phenomenon, with the difference that in our case the trajectory does not explore uniformly (but only azimuthally) the available phase space, because the system is open. Finally, in (c) we see that the fixed point in the origin becomes hyperbolic, and the initial orbit escapes after relatively few bounces ($n = 165$).
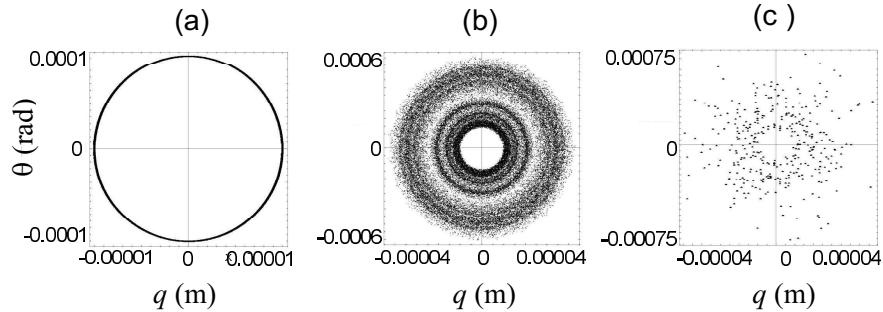
Figure 2.5: *SOS for (a) $\Delta = 0$ where the ray does not escape, (b) $\Delta = 0.001$ m, where the ray escapes after $n = 5 \times 10^4$ bounces and (c) $\Delta = 0.02$ m, where the ray escapes after $n = 165$ bounces.*

2.3.2 Exit basin diagrams

It is well known that chaotic Hamiltonian systems with more than one exit channel exhibit irregular escape dynamics which can be displayed, e.g., by plotting the exit basin [24]. For our open system we have calculated the exit basin diagrams for three different positions of the BS (Fig. 2.6). These diagrams can be constructed by defining a fine grid (2200×2200) of initial conditions (q_0, θ_0). We then follow each ray for a sufficient number of bounces so that it escapes from the cavity. When it escapes from above ($\theta_n > 0$) we plot a black dot in

the corresponding initial condition, whereas when it escapes from below ($\theta_n < 0$) we plot a white dot.

In Fig. 2.6 (a) we show the exit basins for $\Delta = 0.025$ m, the uniformly black or white regions of the plot correspond to rays which display a regular dynamics before escaping, and the dusty region represents the portion of phase space where there is sensitivity to initial conditions. In Fig. 2.6 (b), we show the same plot for $\Delta = 0.05$ m, and in (c) for $\Delta = 0.075$ m.

The exit basin plots in Fig. 2.6 illustrate how the scattering becomes more irregular as the BS is displaced from the center. In particular, we see how regions of regular and irregular dynamics become more and more interwoven as Δ increases. As a reverse trend, for small values of Δ as in Fig. 2.6 (a), there is a single dusty region with a uniform distribution of white and black dots in which no islands of regularity are present.
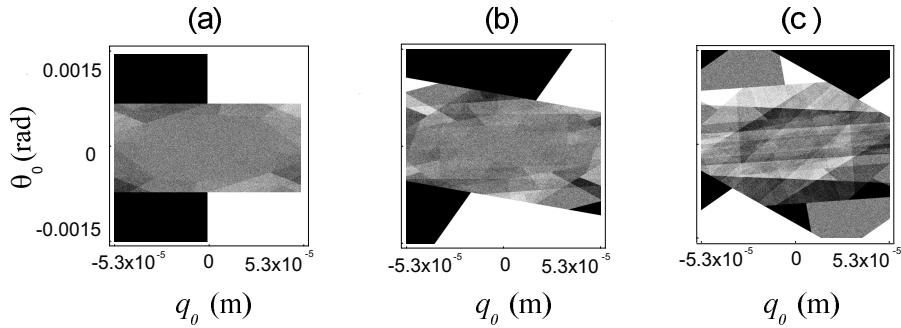
Figure 2.6: *Exit basins for (a) $\Delta = 0.025$ m, (b) $\Delta = 0.05$ m and (c) $\Delta = 0.075$ m.*

2.3.3 Escape rate and Lyapunov exponent

The dynamical quantities that we have calculated next are the escape rate γ and the Lyapunov exponent λ. The escape rate is a quantity that can be used to measure the degree of openness of a system [31]. For hard chaotic systems (hyperbolic), the number N_n of orbits still contained in the phase space after a long time (measured in number of bounces n) decreases as $N_0 \exp(-\gamma n)$ [32]. The Lyapunov exponent is the rate of exponential divergence of nearby trajectories.

Since both λ and γ are asymptotic quantities they should be calculated for very long times. In our system long living trajectories are rare. In order to pick them among the grid of initial conditions (N_0) one has to increase N_0 beyond our computational capability. To overcome this difficulty we choose a different random sequence for each initial condition. In this way we greatly increase the probability of picking long living orbits given by particularly stable random sequences. These long living orbits in turn make possible the calculation of asymptotic quantities such as λ or γ.

The escape rate γ was determined by measuring N_n, as the slope of a $\lg(N_n/N_0)$ versus n plot; the total number of initial conditions N_0 being chosen as 2200×2200.

16

We have calculated the dependence of γ on the displacement of the BS (Δ) from the center of the cavity, where $0 \leq \Delta \leq L/2$. Since for $\Delta > R - L/2$ the left subcavity becomes unstable, it would seem natural to expect that this position of the BS would correspond to a critical point. However, we have found by explicit calculation of both the Lyapunov exponent and the escape rate, that such a critical point does not manifest itself in a sharp way, rather we have observed a finite transition region (as opposed to a single point) in which the functional dependence of λ and γ changes in a smooth way. In Fig. 2.7 (a) we show the typical behavior of N_n/N_0 vs n in semi-logarithmic plot for three different positions of the BS. The displacements of the BS are $\Delta = 0.0875$ m, 0.05 m and 0.03125 m, and the corresponding slopes (escape rate γ measured in units of the inverse number of bounces n) of the linear fit are $\gamma = 0.17693\ n^{-1}$, $0.05371\ n^{-1}$ and $0.01206\ n^{-1}$ respectively. We have found that the decay is exponential only up to a certain time (approximately $70 - 1000$ bounces depending on the geometry of the cavity) due the discrete nature of the grid of initial conditions.

In Fig. 2.7 (b) we see that γ increases with Δ, revealing that for more unstable configurations there is a higher escape rate, as expected. It is also interesting to notice that the exponential decay fits better when the beam splitter is further from the center position, since this leads to smaller stability of the periodic orbits of the system. However, the dependence of the escape rate with the position of the BS is smooth and reveals that the only critical displacement, where the escape rate becomes positive, is $\Delta = 0$.

As a next step, we have calculated the Lyapunov exponent λ for the paraxial map; λ is a quantity that measures the degree of stability of the reference periodic orbit. For a two-dimensional hamiltonian map there are two Lyapunov exponents (λ_1, λ_2) such that $\lambda_1 + \lambda_2 = 0$. In the rest of the Chapter we shall indicate with λ the positive Lyapunov exponent which quantifies the exponential sensitivity to the initial conditions. We have calculated λ for the periodic orbit on axis, using the standard techniques [33], and we have found that the Lyapunov exponent grows from zero with the distance of the BS from the center (Fig. 2.7 (c)). Therefore, the only critical point revealed by the ray dynamics is again the center of the cavity ($\Delta = 0$), where the magnitudes change from zero to a positive value.

The fact that the Lyapunov exponent of our paraxial system *does* become positive (for $\Delta \neq 0$) is rather surprising on its own right. Apparently, the presence of the BS with its stochastic nature introduces exponential sensitivity to initial conditions in the system for every $\Delta \neq 0$, even when both subcavities are stable. This surprise can be explained by taking into account the probabilistic theorem by Furstenberg on the asymptotic limit of the rate of growth of a random product of matrices (RPM) [34]. From this theorem we expect that the asymptotic behavior of the product of a uniform random sequence M_n of $D \times D$ matrices, and for any nonzero vector $\vec{y} \in \Re^D$:

$$\lim_{n \to \infty} \frac{1}{n} \langle \ln |M_n \vec{y}| \rangle_\Omega = \lambda_1 > 0, \tag{2.4}$$

where λ_1 is the maximum Lyapunov exponent of the system, and the angular brackets indicate the average over the ensemble Ω of all possible sequences. This means that for RPM the Lyapunov exponent is a non-random positive quantity. In general, it can be said that there is a subspace Ω^* of random sequences which has a full measure (probability 1) over the whole space of sequences Ω for which nearby trajectories deviate exponentially at a rate λ_1. Although there exist very improbable sequences in Ω which lead to a different asymptotic
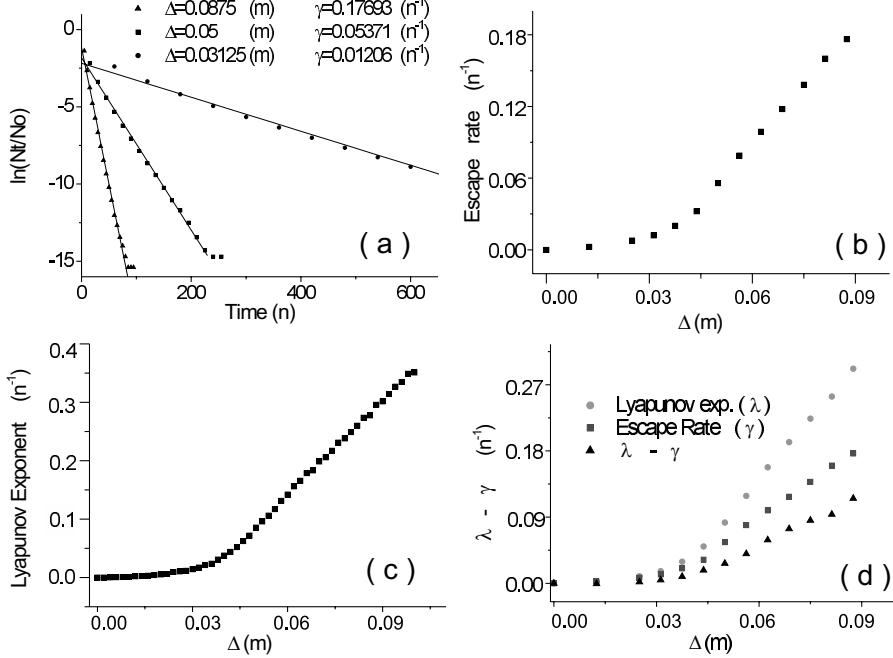
Figure 2.7: *(a) Linear fits used to calculate the escape rate for three different geometrical configurations of the cavity given by $\Delta = 0.03125$ m, $\Delta = 0.05$ m and $\Delta = 0.0875$ m. The time is measured in number of bounces (n). The slope γ is in units of the inverse of time (n^{-1}). Fig. (b) shows the escape rate γ (n^{-1}) as a function of Δ. Fig. (c) corresponds to different Lyapunov exponents λ (n^{-1}) as the BS moves from the center $\Delta = 0$ to the leftmost side of the cavity $\Delta = 0.10$ m. Fig. (d) shows the difference between $\lambda - \gamma$ (n^{-1}), which is a positive bounded function.*

limit, they do not change the logarithmic average (Eq. 2.4) [35]. We have verified this result, calculating the value of λ for different random sequences ω_i, in the asymptotic limit $n = 100000$ bounces, and we obtained in all cases the same Lyapunov exponent.

2.3.4 Mixing properties

Dynamical randomness is characterized by a positive Kolmogorov-Sinai (KS) entropy per unit time h_{KS} [36]. In closed systems, it is known that dynamical randomness is a direct consequence of the exponential sensitivity to initial conditions given by a positive Lyapunov exponent. On the other hand, in open dynamical systems with a single Lyapunov exponent λ, the exponential sensitivity to initial conditions can be related to h_{KS} through the escape rate γ, by the relation [27]:

$$\lambda = h_{KS} + \gamma. \tag{2.5}$$

This formula reveals the fact that in an open dynamical system the exponential sensitivity to initial conditions induces two effects: one is the escape of trajectories out of the neighbor-

hood of the unstable reference periodic orbit at an exponential rate γ, and the other one is a dynamical randomness because of transient chaotic motion near this unstable orbit [27]. This dynamical randomness is a measure of the degree of mixing of the system and as mentioned before is quantified by h_{KS}. Therefore, for a given λ, the larger the mixing is, the smaller the escape rate, and viceversa. From Figs. 2.7 (b,c) it is evident that the Lyapunov exponent and the escape rate have the same smooth dependence on the BS displacement Δ and that $\gamma \leq \lambda$. We have calculated the difference $\lambda - \gamma > 0$ for our system and the result is shown in Fig. 2.7 (d).

The actual value of $\gamma(\Delta)$ depends, for a fixed value of Δ, on the size of the phase space accessible to the system [31], that is, it depends on w_0 and θ_0. We verified this behavior by successively decreasing w_0 and θ_0 by factors of 10 (see Table 2.1), and calculating γ for each of these phase space boundaries. It is clear from these results that γ increases when the size of phase space decreases; in fact for $w_0, \theta_0 \approx 0$, one should get $\lambda \rightarrow \gamma$ and the cavity mixing property should disappear. It should be noted that the increase of γ when decreasing the size of the accessible phase space (ω_0, θ_0) is a general tendency, independent of the chosen boundaries. It is important to stress that, although the randomness introduced

(w_0, θ_0)	$\times 10^0$	$\times 10^{-1}$	$\times 10^{-2}$	$\times 10^{-3}$
γ	0.17639	0.17596	0.19559	0.25259

Table 2.1: *Escape rate for different phase space boundaries. As the boundary shrinks $\gamma(\Delta)$ tends to the corresponding value of $\lambda(\Delta) = 0.29178n^{-1}$. In these calculations the displacement of the BS was $\Delta = 0.0875m$.*

by the stochastic BS is obviously independent from the cavity characteristics, λ and γ show a clear dependence on the BS position. When the BS is located at the center of the cavity it is evident for geometrical reasons that the ray splitting mechanism becomes ineffective: $\lambda = 0 = \gamma$. These results confirm what we have already shown in the SOS (Fig. 2.5).

2.4   Summary

In this Chapter we have characterized the ray dynamics of our paraxial optical cavity with ray splitting by using standard techniques in non-linear dynamics. In particular we have found, both through the SOS and the exit basin diagrams, that the stochastic ray splitting mechanism destroys the regular motion of rays in the globally stable cavity. The irregular dynamics introduced by the beam splitter was quantified by calculating the Lyapunov exponent λ; it grows from zero as the beam splitter is displaced from the center of the cavity. Therefore, the center of the cavity constitutes the only point where the dynamics of the rays is not affected by the stochasticity of the BS. The escape rate γ has been calculated and it has revealed a similar dependence with the position of the beam splitter to that of λ. Furthermore, we have verified that the absolute value of the escape rate tends to that of the Lyapunov exponent as the size of the available phase space goes to zero. This result confirms the fact that the escape rate and therefore the mixing properties of a map depend sensitively on the choice of the boundary [31]. Because of this dependence we cannot claim that our system is chaotic,

despite the positiveness of λ. However, as mentioned before, in the next Chapter we shall demonstrate that ray chaos *can* be achieved for the same class of optical cavities when *non*-paraxial ray dynamics is allowed [37].

CHAPTER 3

Chaotic ray dynamics in an optical cavity with a beam-splitter

In this Chapter we investigate the exact ray dynamics in an optical cavity when a ray splitting mechanism is present [1]. The cavity is a conventional two-mirror stable resonator and the ray splitting is achieved by inserting an optical beam splitter perpendicular to the cavity axis. Using exact Hamiltonian optics, we show that such a simple device presents a surprisingly rich chaotic ray dynamics.

---

[1]Based on G. Puentes, A. Aiello and J. P. Woerdman, Opt. Lett. **29**, 929 (2004).

3.1   Introduction

In this Chapter we present a very simple optical cavity whose ray dynamics is nevertheless fully chaotic. Our starting point is the fact that a two-mirror optical cavity can be *stable* or *unstable* depending on its geometrical configuration [5]. If a light ray is injected inside the cavity it will remain confined indefinitely when the configuration is stable but it will escape after a finite number of bounces when the cavity is unstable. Our interest is in a cavity which has both aspects of stability and instability (Fig. 3.1). The cavity is modelled as a strip resonator [5] made of two identical concave mirrors of radius of curvature R separated by a distance L, where $L < 2R$ so that the cavity is globally stable. We then introduce a beam splitter (BS) inside the cavity, oriented perpendicular to the optical axis. In this way the BS defines two planar-concave subcavities: one on the left and one on the right with respect to the BS, with length L_1 and L_2, respectively. The main idea is that depending on the position of the BS the left (right) subcavity becomes *unstable* for the reflected rays when L_1 (L_2) is bigger than R, while the cavity as a whole remains always *stable* ($L_1 + L_2 < 2R$).

Consideration of this system raises the nontrivial question whether there will be an "equilibrium" between the number of trapped rays and escaping rays. The trapped rays are those which bounce for infinitely long times due to the global stability of the cavity and the escaping ones are those which stay only for a finite time. If such equilibrium exists it could eventually lead to transient chaos since it is known in literature that instability (positive Lyapunov exponents) and mixing (confinement inside the system) form the skeleton of chaotic dynamics [22]. In this Chapter we show that under certain conditions such equilibrium can be achieved in our cavity and that chaotic ray dynamics is displayed.

3.2   Our model

In our system the BS plays a crucial role. It is modelled as a stochastic ray splitting element by assuming the reflection and transmission coefficients as random variables [18]. Within the context of wave optics this model corresponds to the neglect of all interference phenomena inside the cavity, as required by the ray (zero-wavelength) limit. The stochasticity is implemented by using a Monte Carlo method to determine whether the ray is transmitted or reflected [18]. When a ray is incident on the ray splitting surface of the BS, it is either transmitted through it, with probability p, or reflected with probability $1 - p$, where we assume $p = 1/2$ for a 50/50 beam splitter as shown in Fig. 3.1. We then dynamically evolve a ray and at each reflection we use a random number generator with a uniform distribution to randomly decide whether to reflect or transmit the incident ray.

In the context of Hamiltonian optics, to characterize the trajectory of a ray we first choose a reference plane perpendicular to the optical axis $\hat{Z}$, coinciding with the surface of the BS. The intersection of a ray with this plane is specified by two parameters: the height y above the optical axis and the angle θ between the trajectory and the same axis. We consider the rays as point particles, as in standard billiard theory where the propagation of rays correspond to the trajectories of unit mass point particles moving freely inside the billiard and reflecting elastically at the boundary. In particular, we study the evolution of the transversal component of the momentum of the ray, i.e. $v_y = |\vec{v}| \sin(\theta)$ so that we associate a ray of light with the
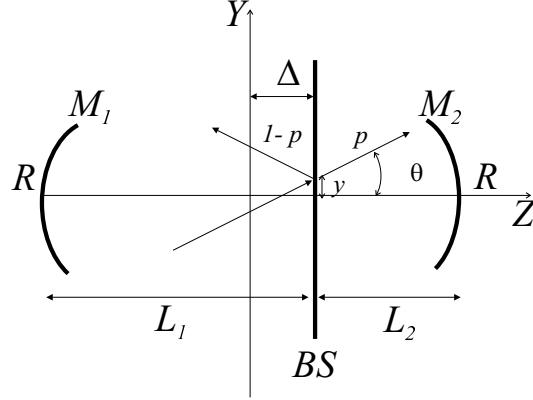
Figure 3.1: *Schematic diagram of the cavity model; R indicates the radius of curvature of the mirrors. Two subcavities of length L_1 and L_2 are coupled by a BS. The total cavity is globally stable for $L = L_1 + L_2 < 2R$. $\Delta = L_1 - L/2$ represents the displacement of the BS with respect to the center of the cavity. When a ray hits the surface of the BS, which we choose to coincide with the reference plane, it can be either reflected or transmitted with equal probability (p); for a 50/50 beam splitter $p = 1/2$.*

two-dimensional vector $\vec{r} = (y, v_y)$. It is important to stress that we use exact 2D-Hamiltonian optics, i.e. we do *not* use the paraxial approximation.

The evolution of a set of rays injected in the cavity with different initial conditions (y_0, v_{y_0}), is obtained by using a ray tracing algorithm. For each initial condition, the actual ray trajectory is determined by a random sequence {...rrttrrrrt..} which specifies if the ray is reflected (r) or transmitted (t) by the BS. When one evolves the whole set of initial conditions, one can choose between two possibilities, either use the *same* random sequence for all rays in the set of initial conditions or use a *different* random sequence for each ray. In this Chapter we use the *same* random sequence for all injected rays in order to uncover the dynamical randomness of the cavity.

3.3 Numerical Results

3.3.1 Poincaré Surface of Section (SOS)

The three quantities that we have calculated to demonstrate the chaotic ray dynamics inside the cavity are the Poincaré Surface of Section (SOS), the exit basin diagrams and the escape time function [23]. In all calculations we have assumed $L_1 + L_2 = 0.16$ m and the radius of curvature of the mirrors $R = 0.15$ m; the diameter d of the two mirrors was $d = 0.05$ m. In addition, the displacement Δ of the BS with respect to the center of the cavity was chosen as 0.02 m (unless specified otherwise), and the time was measured in number of bounces n.

In Fig. 3.2, the successive intersections of a ray with initial transverse coordinates $y_0 = 1 \times 10^{-5}$ m, $v_{y_0} = 0$ are represented by the black points in the SOSs. For $\Delta = 0$ the cavity

23

configuration is symmetric and the dynamics is completely regular (Fig. 3.2 (a)); the on-axis trajectory represents an elliptic fixed point and nearby stable trajectories lie on continuous tori in phase space. In Fig. 3.2 (b), the BS is slightly displaced from the center ($\Delta = 0.02$ m), the same initial trajectory becomes unstable and spreads over a finite region of the phase space before escaping after a large number of bounces ($n = 75328$). In view of the ring structure of Fig. 3.2 (b) we may qualify the motion as azimuthally ergodic. The fact that the ray-splitting mechanism introduced by the BS produces ergodicity is a well known result for a closed billard [18]. We find here an analogue phenomenon, with the difference that in our case the trajectory does not explore uniformly but only azimuthally the available phase space, as an apparent consequence of the openness of the system.
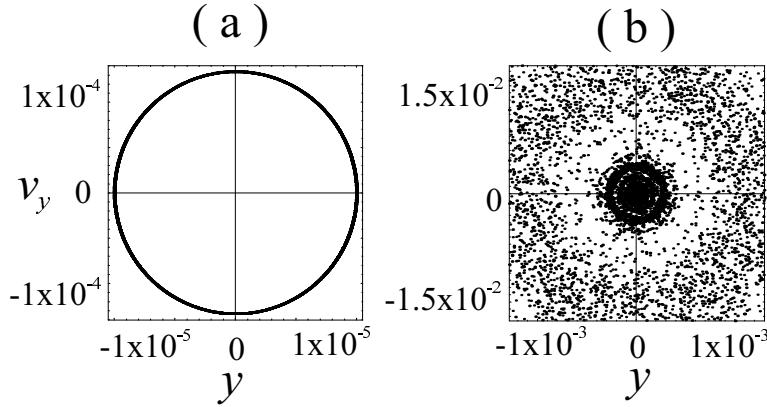

Figure 3.2: *SOS for (a) $\Delta = 0$: the ray dynamics is stable and thus confined on a torus in phase space. (b) $\Delta = 0.002$ m, the dynamics becomes unstable and the ray escapes after $n = 75328$ bounces. Note the ring structure in this plot.*

3.3.2 Exit basin diagrams

It is well known that chaotic hamiltonian systems with more than one exit channel exhibit irregular escape dynamics which can be displayed, e.g., by plotting the exit basin diagram [24]. In our system, this diagram was constructed by defining a fine grid (2200×2200) of initial conditions (y_0, v_{y_0}). Each ray is followed until it escapes from the cavity. When it escapes from above ($v_y > 0$) we plot a black dot in the corresponding initial condition, whereas when it escapes from below ($v_y < 0$) we plot a white dot. This is shown in Fig. 3.3, the uniform regions in the exit basin diagram correspond to rays which display a regular dynamics, whereas the dusty regions correspond to portions of phase space where there is sensitivity to initial conditions, since two initially nearby points can escape from opposite exits. Moreover, in Fig. 3.3 one can see how the boundary between black and white regions becomes less and less smooth as one approaches the center of these diagrams. It is known that this boundary is actually a fractal set [25] whose convoluted appearance is a typical feature

of chaotic scattering systems [26].

Zoom
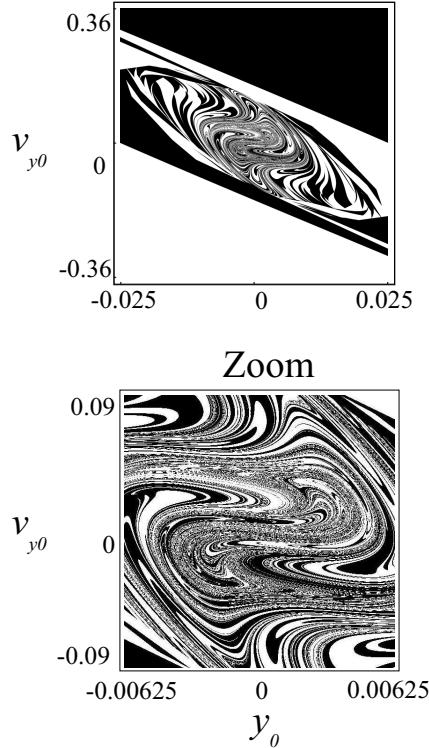
Figure 3.3: *Exit basin for $\Delta = 0.02$ m. The fractal boundaries are a typical feature of chaotic scattering systems.*

3.3.3 Escape time function

Besides sensitivity to initial conditions, another fundamental ingredient of chaotic dynamics is the presence of infinitely long living orbits which are responsible for the mixing properties of the system. This set of orbits is usually called repeller [27], and is fundamental to generate a truly chaotic scattering system. To verify the existence of this set we have calculated the escape time or time delay function [28] for a one-dimensional set of initial conditions specified by the initial position y_0 (impact parameter) taken on the mirror M_1 and the initial velocity $v_{y_0} = 0$. The escape time was calculated in the standard way, as the time (in number of bounces n) it takes a ray to escape from the cavity.

Fig. 3.4 (a) shows the escape time function. The singularities of this function are a clear signature of the existence of long living orbits and the presence of peaks followed by flat regions are a signature of the exponential sensitivity to initial conditions. In order to verify the presence of an *infinite* set of long living orbits, we have zoomed in on the set of impact parameters y_0 in three different intervals (Fig. 3.4 (b), (c) and (d)). Each zoom reveals the
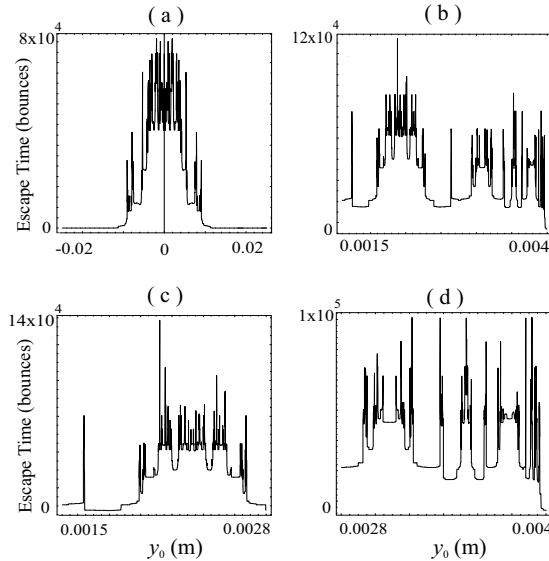
**Figure 3.4:** *(a) Escape time as a function of the initial condition y_0. (b) Blow up of a small interval along the horizontal axis in (a). (c) and (d) Blow ups of consecutive intervals along the set of impact parameters y_0 shown in (b).*

existence of new infinitely long living orbits. Infinite delay times correspond to orbits that are asymptotically close to an unstable periodic orbit. If we would continue to increase the resolution we would find more and more infinitely trapped orbits. The repeated existence of singular points is a signature of the mixing mechanism of the system due to the global stability of the cavity.

3.4   Summary

In conclusion, in this Chapter we have demonstrated that our simple optical system displays chaotic ray dynamics. It is important to stress that a key component for the development of chaos is the inclusion of non-paraxial rays which add the mixing properties to the system [29]. In fact, it has been previously shown that paraxial ray dynamics can be unstable but not chaotic, in systems with stochastic perturbations [16, 30]. In our case, it is the stochastic ray splitting mechanism induced by the BS that destroys the regular motion of rays in the globally stable (but non-paraxial) cavity, as shown by the SOSs. Moreover, by calculating the exit basin diagrams we have found that they show fractal boundaries, which is a typical feature of chaotic ray dynamics [24]. Finally, through the singularities in the escape time function, we have verified the presence of infinitely long living orbits, which in turn revealed the mixing mechanism of our optical cavity. An experimental confirmation of the fractal properties of the exit basin can be performed, e.g., in the way suggested in [26], by injecting a narrow laser beam into the cavity either in a regular or in a dusty region of phase space. In

26

the former case one expects the beam to leave the cavity either from above or below, while in the latter case both exits should appear illuminated. This proposed experiment is fully within the context of geometrical optics (interference plays no role) so that our stochastic model of the BS is adequate.
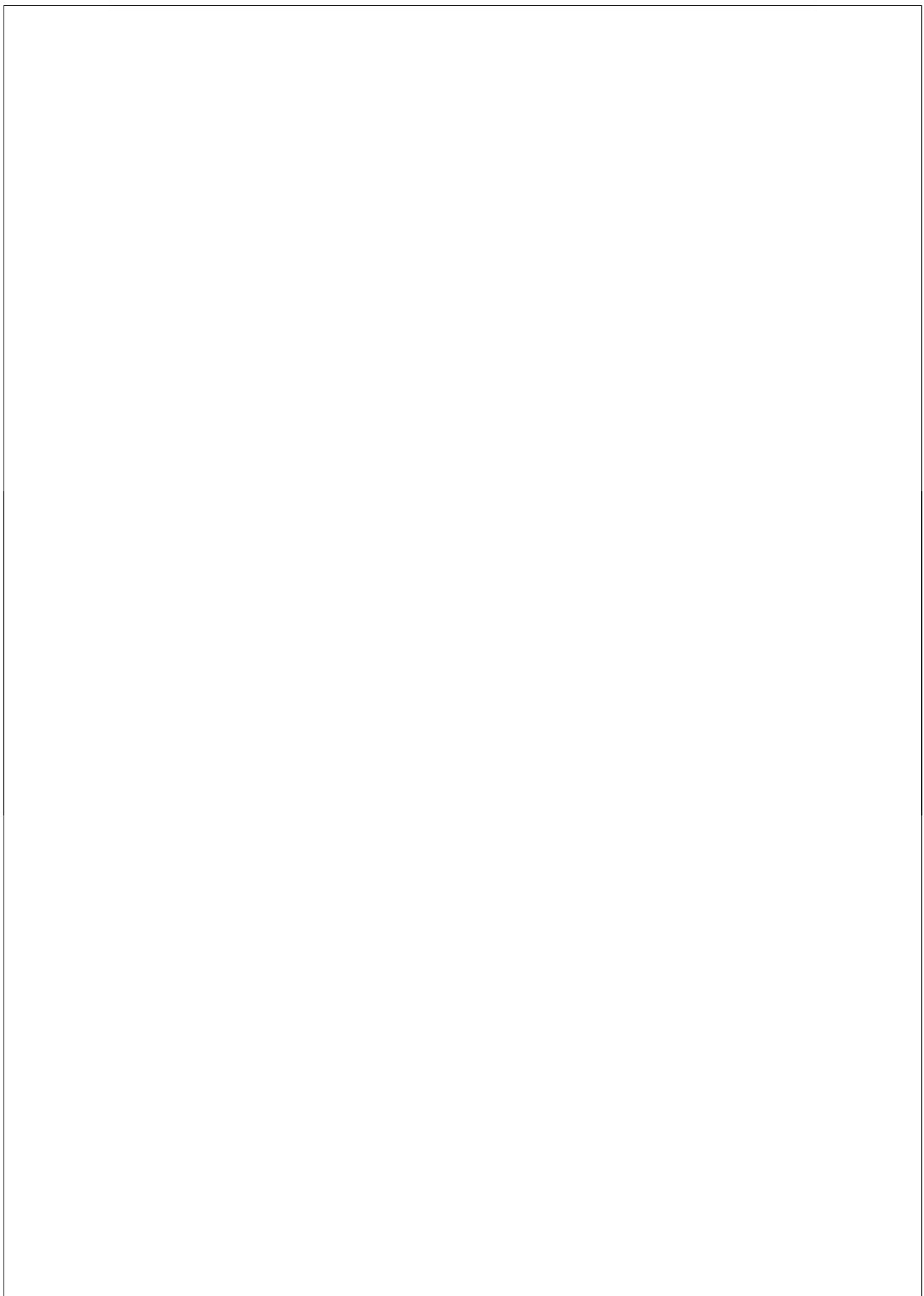
CHAPTER **4**

Universality in the polarization entropy and depolarizing power of light scattering media: Theory

In this Chapter we present the theoretical background related to our experiments on light depolarization due to multi-mode scattering [44]. The key theoretical concept we introduce is the effective Mueller matrix, which describes our spatial multi-mode detection set-up.

4.1   Introduction

In classical optics, a light beam is said to be polarized when its polarization direction describes a stationary curve during the measurement time, and depolarized when its polarization direction varies rapidly with respect to other degrees of freedom that are not resolved during the experiment, such as wavelength, time or position of the beam [4]. Moreover, depolarization also occurs when a single-mode input beam is coupled to a multi-mode (either spectral or spatial) optical system and the polarization properties of the outgoing beam are measured with a mode-insensitive device. The main mechanism of depolarization that we analyze in this Chapter is given by the coupling of polarization with spatial degrees of freedom. A typical example of this is the case of a beam of light initially prepared in a single spatial-mode ($\mathbf{k}_{\mathrm{in}}$) that is incident on an optically passive inhomogeneous medium. Due to the spatial inhomogeneities in the medium, the beam suffers multiple scattering and, as a result, it emerges as a (partially) incoherent superposition of spatial modes ($\mathbf{k}_{\mathrm{out}}$). Even when each of the output modes is fully polarized, the output beam appears to be (partially) depolarized when its spatial information is averaged out in a multi-mode detection set-up.

There exist several formalisms that enable to represent the polarization state of light. Among them, the Mueller-Stokes formalism is particularly well suited for the description of partially polarized light. Within this formalism, the polarization state of the light field is completely characterized by the 4 dimensional Stokes vector $\mathbf{S} = (S_0, S_1, S_2, S_3)$, where S_0 is to the total intensity of the beam, and $S_{i=1,2,3}$ are the relative intensities in the V/H, $45°/-45°$, and RHC/LHC bases. The only restriction for a Stokes vector to represent a physical polarization state is that $\sum_i S_i^2 \leq S_0^2$. Additionally, any passive optical system can be characterized by a 4×4 Mueller matrix, whose 16 real elements map the polarization state of the input and output beams. At this point, it might be good to stress that there exists a considerable ambiguity in the terminology used to characterize different scattering systems; this ambiguity arises from to the overlap of scientific communities working in the polarimetric properties of light. We specify that in this contribution we will use the standard notation in optics introduced by L. Mandel and E. Wolf [45]. This means, we shall consider as scattering system, any passive optical system that can be characterized by a Mueller matrix (or scattering matrix). In other words, any medium that transforms an input Stokes vector $\mathbf{S}_{\mathrm{in}}$ into an output Stokes vector $\mathbf{S}_{\mathrm{out}}$, provided that the transformation is linear. Thus, the ensemble of scattering media may comprise a single element, such as a lens, a polarizer, a retarder, a spatial light modulator, or an optical fiber, as well as a cascade of optical elements or a solution of micro-particles. These different media may be grouped in two broad classes: *deterministic* and *non-deterministic* [45]. To the first class belong all media that do not depolarize the input light, in this particular case, the Mueller matrix representing the medium is a Mueller-Jones matrix [46]. To the second class belong all media that do indeed depolarize the input light and whose Mueller matrix has to be written as a sum of (at most) four Mueller-Jones matrices [46].

For a given depolarizing mechanism, the amount of depolarization can be quantified by calculating either the entropy (E_F) or the degree of polarization (P_F) of the scattered field [4]. It is possible to show that the field quantities E_F and P_F are related by a monotonous single-valued function. For example, polarized light ($P_F = 1$) has $E_F = 0$ while partially polarized light ($0 \leq P_F < 1$) has $1 \geq E_F > 0$. In this sense low (high) polarization entropy implies the

existence of a strongly (weakly) polarized structure in the light field [47]. When the incident beam is purely polarized and the output beam is partially polarized, the medium is said to be depolarizing. Depolarization is called isotropic when the degree of polarization $0 \leq P_F' < 1$ of the scattered field is the same for any input pure state $P_F = 1$ [48]. In this particular case, the medium can be characterized by a single parameter, related to the magnitude of its depolarizing power. However, most media depolarize in different amounts different input states of polarization. When this is the case, they are termed anisotropic depolarizers and a single parameter can not fully characterize them. An average measure of the depolarizing power of a medium is given by the so called index of depolarization D_M [49], where the average refers to different pure input states. Non-depolarizing media are characterized by $D_M = 1$, while depolarizing media have $0 \leq D_M < 1$.

A depolarizing scattering process is always accompanied by an increase of the entropy of the light, the increase being due to the interaction of the field with the medium, which couples the polarization degrees of freedom of the field with the multi-dimensional degrees of freedom of the scatterer (either spatial or temporal). These extra degrees of freedom are traced over during the polarization measurement, and leave the polarization degrees of freedom of the scattered field in a (partially) mixed state. In general, for an anisotropic depolarizer the entropy added to the light field by the medium will depend on the input state. An average measure of the entropy that a given random medium can add to the entropy of the incident light beam, is given by the polarization entropy E_M [48], where the average again refers to different pure polarization input states. Non-depolarizing media are characterized by $E_M = 0$, while depolarizing media satisfy $0 < E_M \leq 1$. As the field quantities E_F and P_F are related to each other, so are the medium quantities E_M and D_M, with the main difference that they are related through a *multi-valued* function, the reason being that the corresponding relation for the field parameters is non-linear.

In Ref. [50] it was shown that there exists a universal relation $E_M(D_M)$ between the polarization entropy E_M and the index of depolarization D_M valid for any scattering medium. More specifically, E_M is related to D_M by a multi-valued function which covers the full range from zero to total depolarization. This universal relation provides a simple characterization of the polarization properties of *any* medium. We emphasize that the results found in [50] apply both to classical and quantum (single photon) scattering processes, and might therefore become relevant for quantum communication optical applications, where depolarization is associated with the loss of quantum coherence [51].

In the next section we review the Mueller-Stokes formalism, suitable for a single spatial mode description of the light field. In particular we formally introduce the concepts of deterministic and non-deterministic Mueller matrices, which correspond to non-depolarizing and depolarizing media respectively.

4.2 Mueller-Stokes formalism

Consider a quasi-monochromatic beam of light of mean angular frequency ω [52]. Let us denote with $\mathbf{x}, \mathbf{y}, \mathbf{z}$ the axes of a Cartesian coordinate system, with the $\mathbf{z}$-axis along the direction of propagation of the beam whose angular spread around $\mathbf{z}$ is assumed to be small enough to

satisfy the *paraxial* approximation. Let

$$E_x(x,y,z_0,t_0) \equiv E_0(x,y)e^{-i\omega(t_0-z_0/c)}, \quad E_y(x,y,z_0,t_0) \equiv E_1(x,y)e^{-i\omega(t_0-z_0/c)}, \qquad (4.1)$$

be the components of the complex paraxial electric field vector in the **x**- and **y**-direction respectively, at the point (x,y) located in the transverse plane $z = z_0$ at time t_0. If the field is *uniform* on the transverse plane, then E_x and E_y are independent of x and y, and a complete description of the field can be achieved in terms of a doublet **E** of complex variables (with possibly stochastic temporal fluctuations):

$$\mathbf{E} = \begin{pmatrix} E_0 \\ E_1 \end{pmatrix}, \qquad (4.2)$$

where E_0 and E_1 are now complex-valued functions of z_0 and t_0 only (the subscripts 0 and 1 correspond to the cartesian directions **x** and **y** respectively). A complete study of the propagation of **E** along **z** can be found in [45]. However, the main result we need is that propagation through non-depolarizing media can be described by a *deterministic* Mueller (or Mueller-Jones) matrix M^J, while to describe the propagation of a light beam through a depolarizing medium it is necessary to use a *non-deterministic* Mueller matrix M.

4.2.1 Deterministic Mueller matrix M^J: non-depolarizing media

In a broad sense, a *deterministic* linear scatterer as, e.g., a quarter-wave plate, a rotator or a polarizer, is an optical system which can be described by a 2×2 complex Jones [4] matrix

$$T = \begin{pmatrix} T_{00} & T_{01} \\ T_{10} & T_{11} \end{pmatrix}. \qquad (4.3)$$

By this we mean that if **E** and **E**$'$ describe the polarization state of the field immediately before and immediately after the scatterer respectively, then they are linearly related by the Jones matrix T:

$$\mathbf{E}' = T\mathbf{E}. \qquad (4.4)$$

Therefore a deterministic scattering process, where there are no fluctuations of E with respect to other degrees of freedom (either spatial or temporal), can be described by a Jones matrix. To account for the possible fluctuations of the field, we can introduce the coherency matrix of the field J defined as [6]

$$J_{ij} = \langle E_i E_j^* \rangle, \qquad (i,j = 0,1), \qquad (4.5)$$

where the angular brackets denote the statistical average over different realizations of the fluctuations of the field. The coherency matrix is Hermitian and positive semi-definite by construction. By imposing as normalization condition $\mathrm{Tr}\{J\} = 1$, J can be interpreted as a quantum density matrix [53]; which evidences the analogy between the classical description of a partially polarized beam with the quantum description of a single photon in a mixed state [50]. Given the coherency or covariance matrix J one can calculate the entropy of the field E_F through [4]

$$E_F = -\mathrm{Tr}\{J\log_2(J)\}, \qquad (4.6)$$

where the symbol $\text{Tr}\{\cdot\}$ denotes the trace operation, and $0 \leq E_F \leq 1$ by definition. From Eq. (4.6) we see that E_F is equivalent to the von Neumann definition of entropy of a single-photon state [54].

An alternative description can be given in terms of the Stokes parameters of the beam. The four Stokes parameters S_μ ($\mu = 0, \ldots, 3$) of the beam are defined as

$$S_\mu = \text{Tr}\{J\sigma_\mu\}, \qquad (\mu = 0, \ldots, 3), \tag{4.7}$$

where the $\{\sigma_\mu\}$ are the normalized Pauli matrices:

$$\sigma_0 = \tfrac{1}{\sqrt{2}}\begin{pmatrix} 1 & 0 \\ 0 & 1 \end{pmatrix}, \qquad \sigma_1 = \tfrac{1}{\sqrt{2}}\begin{pmatrix} 0 & 1 \\ 1 & 0 \end{pmatrix},$$
$$\sigma_2 = \tfrac{1}{\sqrt{2}}\begin{pmatrix} 0 & -i \\ i & 0 \end{pmatrix}, \qquad \sigma_3 = \tfrac{1}{\sqrt{2}}\begin{pmatrix} 1 & 0 \\ 0 & -1 \end{pmatrix}. \tag{4.8}$$

Now, if with S_μ and S'_μ we denote the Stokes parameters of the beam before and after the scatterer respectively, it is easy to show that they are linearly related by the real-valued 4×4 Mueller-Jones matrix M^J as

$$S'_\mu = M^J_{\mu\nu} S_\nu, \tag{4.9}$$

where summation on repeated indices is understood and

$$M^J = \Lambda^\dagger (T \otimes T^*) \Lambda, \tag{4.10}$$

where the symbol "$\otimes$" denotes the outer matrix product and the *unitary* matrix Λ is defined as

$$\Lambda = \frac{1}{\sqrt{2}} \begin{pmatrix} 1 & 0 & 0 & 1 \\ 0 & 1 & -i & 0 \\ 0 & 1 & i & 0 \\ 1 & 0 & 0 & -1 \end{pmatrix}. \tag{4.11}$$

The columns of Λ are given by the elements of the Pauli matrices. From the structure of M^J it follows that a deterministic medium does not depolarize, that is $P_F(S) = P_F(S')$ where the degree of polarization P_F of the field is defined as

$$P_F(S) = \frac{\sqrt{S_1^2 + S_2^2 + S_3^2}}{S_0}. \tag{4.12}$$

By writing the coherency matrix J in terms of the Stokes parameters, and imposing the normalization condition $\text{Tr}\{J\} = 1$, it is possible to show that the degree of polarization P_F is related to the entropy of the field E_F by (see Fig. 4.1):

$$E_F = -\frac{1+P_F}{2}\log_2\left(\frac{1+P_F}{2}\right) - \frac{1-P_F}{2}\log_2\left(\frac{1-P_F}{2}\right). \tag{4.13}$$

Let us conclude by noticing that for deterministic media the two descriptions in terms of T or M^J are completely equivalent in the sense that the 16 real elements of M^J do not contain more information than the 4 complex elements of T.
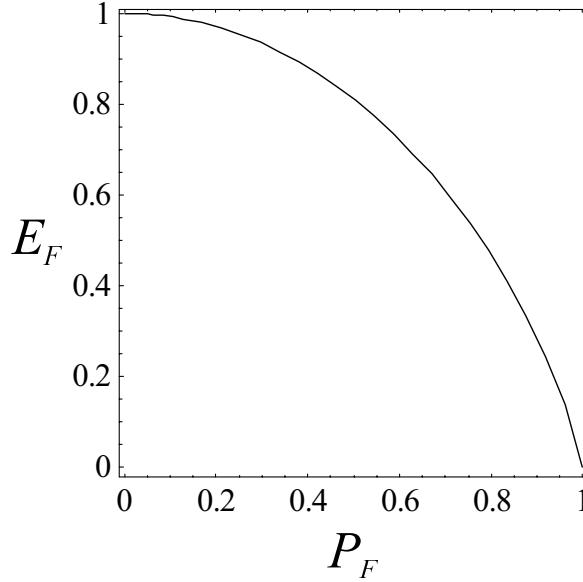
Figure 4.1: *Entropy (E_F) vs degree of polarization (P_F) for the light field.*

4.2.2 Non-deterministic Mueller matrix M: depolarizing media

A *non*-deterministic scatterer is, in a broad sense, an optical system which *cannot* be described by a Mueller-Jones matrix. In this class fall any depolarizing optical systems, such as multi-mode optical fibers, particles in suspension, etc. It has been shown [61, 62] that it is possible to describe a non-deterministic optical system as an ensemble of deterministic systems, in such a way that each realization $\mathscr{E}$ in the ensemble is characterized by a well-defined Jones matrix $T(\mathscr{E})$ occurring with probability $p_{\mathscr{E}} \geq 0$. This ensemble representation, in turn, reflects some uncertainty in the description of the medium which can be explained in terms of unobserved degrees of freedom of the probe beam. Then, the Mueller matrix M of the system can be written as

$$M = \Lambda^{\dagger}(\overline{T \otimes T^*})\Lambda, \tag{4.14}$$

where the $\overline{}$ bar symbol denotes the average with respect to the ensemble representing the medium:

$$\overline{T \otimes T^*} = \sum_{\mathscr{E}} p_{\mathscr{E}} T(\mathscr{E}) \otimes T^*(\mathscr{E}). \tag{4.15}$$

At this point it is useful to introduce the auxiliary 4×4 Hermitian matrix H defined as the system dynamical matrix [47]:

$$H = \frac{1}{2} \sum_{\mu,\nu}^{0,3} M_{\mu\nu}(\sigma_{\mu} \otimes \sigma_{\nu}^*), \tag{4.16}$$

34

where Tr$H = 1$, $M_{\mu\nu}$ are the elements of the Mueller matrix and σ_i ($i = 0, 1, 2, 3$) the normalized Pauli matrices (see Eq. 4.8). H is by definition, positive semi-definite, that is, all its eigenvalues $\{\lambda_0, \lambda_1, \lambda_2, \lambda_3\}$ are non-negative. It is possible to demonstrate [46] that any Mueller matrix can be decomposed as a sum of at most four Mueller-Jones matrices:

$$M = \sum_{i=0}^{3} \lambda_i M_i^J, \tag{4.17}$$

where λ_i are the eigenvalues of H (Eq. 4.16). This positive decomposition allows us to give a probabilistic interpretation to λ_i by considering each of them as the probability of occurrence of the Mueller-Jones matrix M_i^J. Further, it is through (Eq. 4.17) that the statistical nature of a depolarizing process is revealed, and it becomes clear that two different media can be described by two different ensembles of Mueller-Jones matrices with exactly the same coefficients λ_i. These eigenvalues can, in turn, be combined to form a single scalar quantity that is a measure of the polarimetric disorder added to the field by the system, i.e., the entropy of the medium E_M:

$$E_M = -\sum_{\nu=0}^{3} \lambda_\nu \log_4(\lambda_\nu). \tag{4.18}$$

Moreover, it is possible to show that the index of depolarization (or depolarizing power) D_M of the medium can be written as:

$$D_M = \left[\frac{1}{3} \left(4 \sum_{\nu=0}^{3} \lambda_\nu^2 - 1 \right) \right]^{1/2}. \tag{4.19}$$

For a non-depolarizing system, $E_M = 0$, $D_M = 1$, and H has a single eigenvalue equal to one, and the rest equal to zero. This means that its corresponding Mueller matrix is a Mueller-Jones matrix, as expected. Conversely, for a totally depolarizing medium $E_M = 1$, $D_M = 0$ and H has four eigenvalues equal to 1/4.

In Ref. [50], a universal relation between E_M and D_M was found. This universal character can be explained by noticing that both E_M and D_M only depend on the four eigenvalues (λ_i) of H. By using the normalization condition Tr$\{H\} = 1$, we see there are only three independent parameters. We choose then to write $E_M(D_M, \lambda_1, \lambda_2)$, where $0 \leq \lambda_{1,2} \leq 1$ are two independent eigenvalues of H. By varying $\lambda_{1,2}$ it is possible to obtain a whole domain en the $E_M - D_M$ plane (see Fig. 4.2). The analytical curves that determine this domain are detailed in Ref. [50]. Cuspid points in Fig. 4.2 separate different types polarization dependent scattering processes.

In subsection 4.2.1, Eq. (4.6), we pointed out the analogy between the definition of *polarization entropy* and the von Neumann entropy of a quantum system. In the case of bipartite systems, the von Neumann entropy quantifies the degree of entanglement of the subsystems for pure states, and it is a measure of the degree of mixture for non-pure states. It is worth noticing that it is possible as well to relate the *degree of polarization* of a system of dimension N, with its linear entropy, which is an alternative measure of the degree of mixedness of a system (and is generally easier to calculate than the Von Neumann entropy) [55, 56]. Namely, given the density matrix of the system ρ, one can define the degree of polarization P_N by:

$$P_N = \sqrt{\frac{N \text{Tr}\{\rho^2\} - 1}{N - 1}}. \tag{4.20}$$
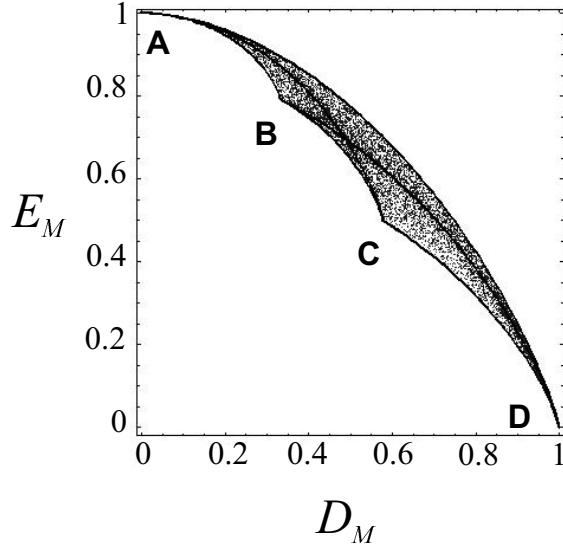
Figure 4.2: *Numerically determined domain for the entropy (E_M) vs index of depolarization (D_M) corresponding to any scattering process. The solid lines are given by analytical curves [50]. The four cuspid points are given by* $\mathbf{A} = (0,1)$, $\mathbf{B} = (1/3, \log_4 3)$, $\mathbf{C} = (1/\sqrt{3}, 1/2)$, *and* $\mathbf{D} = (1,0)$.

Recalling that the linear entropy is defined as [55]:

$$S_N = \frac{N}{N-1}[1 - \text{Tr}\{\rho^2\}], \tag{4.21}$$

and combining Eq. (4.20), and Eq. (4.21) it is simple to show that:

$$S_N = 1 - P_N^2. \tag{4.22}$$

The mathematical space where medium parameters E_M and D_M are defined is equivalent to that of a quantum system with a Hilbert space of dimension $N = 4$, i.e., the polarization state space of two photons. Within this analogy, E_M can be interpreted as the von Neumann entropy of a four dimensional ($N = 4$) quantum system. Additionally, for $N = 4$ we have $D_M = P_4$, and $S_4 = 1 - D_M^2$. Equations (4.21) and (4.22) are also valid in the case of a single photon taking $N = 2$.

In the next section we formally introduce the concept of *effective* Mueller matrix which serves as a theoretical tool to describe our depolarization experiments.
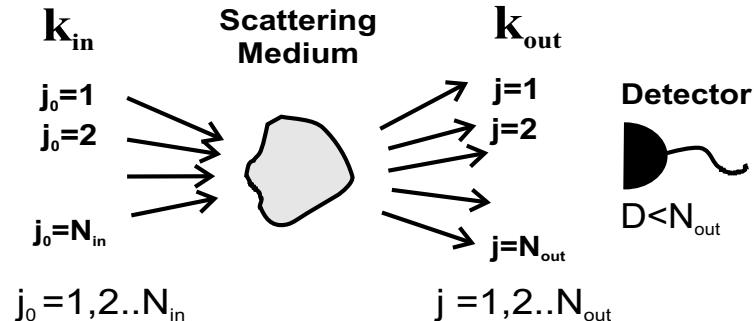
Figure 4.3: *An input beam with N_{in} spatial modes label by j_0 impinge on a scattering medium. The scattering process spans the outgoing beam in N_{out} spatial modes labelled by j. Eventually D ($D < N_{\text{out}}$) modes are detected.*

4.3 The effective Mueller matrix

The Mueller-Stokes formalism described in the previous section is suitable for a single spatial mode description of the field, where depolarization occurs due to coupling of polarization degrees of freedom with temporal domain, for instance by propagation on dynamic media. However, it is possible to extend this formalism to the multi-spatial-mode case. To this end, let us consider the case of a scattering process in which a coupling between polarization and spatial modes of the field occurs and a multi-mode detection scheme is employed. This idea is schematized in Fig. 4.3, where N_{in} spatial modes of the field impinge on a scatterer, N_{out} leave from it and D modes are eventually detected. We make the assumption that different spatial modes of the field are uncorrelated, that is, we will consider for simplicity that the source is spatially incoherent. Moreover, without loss of generality, we assume $N_{\text{in}} = N_{\text{out}} = N$. Let $\mathbf{S}(j) \equiv \{S_0(j), S_1(j), S_2(j), S_3(j)\}$ be a generic 4-Dim Stokes vector defined with respect to the mode j, where $j \in \{1, \ldots, N\}$. For a N-mode field we have a collection (N) of 4-Dim Stokes vectors that can be arranged in a single $4N$-Dim "super" Stokes vector $\mathbb{S} = \{\mathbf{S}(1), \ldots, \mathbf{S}(N)\}$. Generally speaking, when the N-mode light beam undergoes a polarization-sensitive scattering process, the Stokes vectors $\{\mathbf{S}_{\text{in}}(j_0)\}$ of the input beam are related to the set of vectors $\{\mathbf{S}_{\text{out}}(j)\}$ of the output beam by:

$$\mathbf{S}_{\text{out}}(j) = \sum_{j_0=1}^{N} M^J(j, j_0) \mathbf{S}_{\text{in}}(j_0), \qquad (j = 1, \ldots, N), \tag{4.23}$$

37

where $M^J(j, j_0)$ is the 4×4 Mueller-Jones matrix that describes the scattering from the input mode j_0 to the output mode j. If we introduce a "super" $4N \times 4N$ Mueller matrix defined as

$$\mathbb{M} \equiv \begin{pmatrix} M^J(1,1) & \dots & M^J(1,N) \\ \vdots & \ddots & \vdots \\ M^J(N,1) & \dots & M^J(N,N) \end{pmatrix}, \tag{4.24}$$

where each block $M^J(j_1, j_2)$ is a 4×4 Mueller-Jones matrix, then we can rewrite Eq. (4.23) in a compact form as

$$\mathbb{S}_{\text{out}} = \mathbb{M} \cdot \mathbb{S}_{\text{in}}. \tag{4.25}$$

After the scattering process took place, we have to detect its products. In Ref. [13], it was shown that when D modes of the field are detected out of N scattered modes ($D < N$), a mode-insensitive polarization analyzer put in front of a bucket-detector can be described by a $4N \times 4N$ block-diagonal matrix $\mathbb{A}$:

$$\mathbb{A} \equiv \begin{pmatrix} A(1) & & & \\ & \ddots & & \\ & & A(D) & \\ & & & \mathbf{0} \end{pmatrix}, \tag{4.26}$$

where $A(j)$, $(j = 1, \dots, D)$ are the 4×4 transmission Mueller-Jones matrices, of the polarization analyzer, whose elements depend on the different geometrical projections of the impinging mode-directions $\mathbf{j}$ [13]. The 4×4 real-valued positive semi-definite transmission matrices are in fact projectors, and $\mathbf{0}$ is a null $(N-D) \times (N-D)$ matrix. In the paraxial limit ($D << N$) each $A(j)$ reduces to the 4×4 identity matrix, and the polarization state of the scattered beam after the analyzer, is described by the super-Stokes-4D vector $\mathbb{S}_D \equiv \{\mathbf{S}_D(1), ..., \mathbf{S}_D(D)\}$ given by

$$\mathbb{S}_D = \mathbb{A} \cdot \mathbb{M} \cdot \mathbb{S}_{\text{in}}. \tag{4.27}$$

Finally, because of the mode-insensitive detection, the sum over all the detected modes D reduces the number of degrees of freedom of the field from $4D$ to 4, producing the *detected* 4-Dim Stokes vector $\mathbf{S}_D$:

$$\mathbf{S}_D = \sum_{j=1}^{D} \mathbf{S}_D(j) \equiv M_{\text{eff}} \mathbf{S}_{\text{in}}(1), \tag{4.28}$$

where we have assumed that the input light beam is prepared in the single mode $j_0 = 1$, so that $\mathbf{S}_{\text{in}}(j_0) = \delta_{j_0 1} \mathbf{S}_{\text{in}}(1)$ and with M_{eff} we have denoted an effective 4×4 Mueller matrix defined as

$$M_{\text{eff}} = \sum_{j=1}^{D} A(j) M^J(j, 1), \tag{4.29}$$

which is written as a sum of D Mueller-Jones matrices. It is important to notice that while the product of Mueller-Jones matrices is still a Mueller-Jones matrix (in physical terms: a cascade of non-depolarizing optical elements is still a non-depolarizing optical system), a sum, in general, is not. This causes depolarization. Moreover, since the "matrix coefficients"

$A(j)$ are non-negative, the matrix M_{eff} in Eq. (4.29) is an explicit version of the Mueller matrix written in Eq. (4.14). Thus we have shown, by an explicit derivation, how to build the statistical ensemble representing the depolarizing medium, for this particular case. It is worth noticing, that because of the dependence of the effective Mueller matrix on the number of detected modes D, it is possible to obtain different Mueller matrices for a given system, by increasing (or decreasing) the number of detected modes.

4.4 Summary

In this Chapter we have presented the Mueller-Stokes formalism and its extension to the multi-mode case via the formal definition of the the effective Mueller matrix. This theoretical framework provides a suitable description of the depolarization experiments that shall be discussed in the next Chapter.
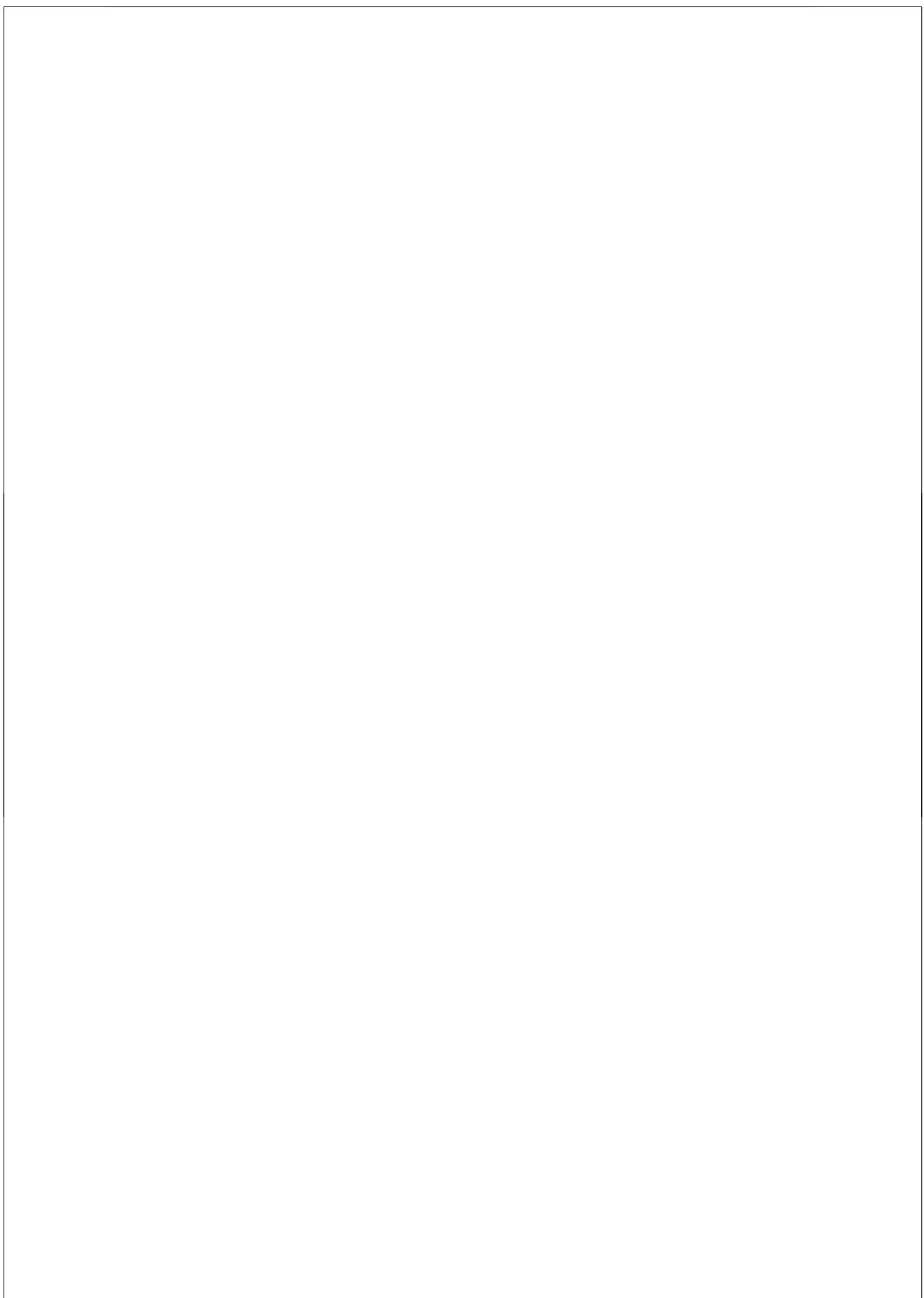
CHAPTER 5

Universality in the polarization entropy and depolarizing power of light scattering media: Experiment

---

In this Chapter we report experimental results on light depolarization due to multi-mode scattering [1]. *By means of polarization tomography, we characterize the depolarizing power and the polarization entropy of a broad class of optically scattering media and confirm the recently predicted universal behavior of these two quantities (A. Aiello and J. P. Woerdman, Phys. Rev. Lett. **94**, 090406 (2005)).*

---

[1]Based on G. Puentes, D. Voigt, A. Aiello, and J. P. Woerdman, Opt. Lett. **30**, 3216 (2005).

5.1   Introduction

Polarization aspects of light scattering are important in molecular spectroscopy, optical communication, industrial and medical applications; we focus here in particular on the phenomenon of depolarization. The depolarizing properties of a scattering medium can be characterized by two parameters; i.e. the entropy of the medium (E_M), which is an average measure of the entropy added to the field by the medium, and the index of depolarization of the medium (D_M), which is an average measure of its depolarizing power [48, 50]. In both cases the average refers to different pure polarization input states. Recently, it was theoretically predicted, on the basis of an exact derivation, that the relation between E_M and D_M is a multi-valued function. Moreover, this multi-valued relation possesses a universal character since it is valid for *any* optical depolarizing process [50]. In this Chapter we report an experimental study of the depolarizing properties of a large set of scattering media, ranging from milk to multimode optical fibers. The results confirm the theoretical predictions for the bounds of the multi-valued function $E_M[D_M]$.

5.2   The effective Mueller matrix

Within the Mueller-Stokes formalism [4], explicit expressions for D_M and E_M can be derived by using the Hermitian operator H defined as [48]:

$$H = \frac{1}{2} \sum_{\mu,\nu}^{0,3} M_{\mu\nu}(\sigma_\mu \otimes \sigma_\nu^*), \qquad (5.1)$$

where $\mathrm{Tr}H = 1$, $M_{\mu\nu}$ are the elements of the Mueller matrix and σ_i ($i = 0, 1, 2, 3$) the normalized Pauli matrices. It can be shown that any physically realizable system is characterized by a positive-semidefinite matrix H, such that its four eigenvalues satisfy $0 \leq \lambda_\nu \leq 1$ ($\nu = 0, 1, 2, 3$). It is then possible to express the polarization entropy E_M and the index of depolarization D_M as [50]:

$$E_M = -\sum_{\nu=0}^{3} \lambda_\nu \log_4(\lambda_\nu), \quad D_M = \left[\frac{1}{3} \left(4 \sum_{\nu=0}^{3} \lambda_\nu^2 - 1 \right) \right]^{1/2}. \qquad (5.2)$$

Introduction of an effective Mueller matrix allows to describe depolarization due to coupling between polarization and spatial modes of the field (see Chapter 4, this Thesis). In this way we extend the standard Mueller-Stokes formalism, which is suitable for a single spatial-mode description of the field, to the case in which N_{in} spatial modes of the field impinge on the scatterer, N_{out} modes leave from it and $D < N_{\mathrm{out}}$ modes are eventually detected. For $N_{\mathrm{in}} = 1$, and within the paraxial approximation $D << N_{\mathrm{out}}$, the effective Mueller matrix can be written as:

$$M_{eff} = \sum_{j=1}^{D} A(j) M^J(j, 1), \qquad (5.3)$$

where $j = 1, .., D$ labels the set of detected modes D, $M^J(j, 1)$ is the Mueller-Jones matrix connecting the single input mode "1" with the output mode j, and $A(j)$ is a projection matrix

whose form is determined by the actual measurement scheme. M_{eff} is then written as a sum of D Mueller-Jones matrices.

5.3   Experimental scheme

In order to measure the effective Mueller matrix M_{eff} and thus the index of depolarization D_M and the entropy E_M of a scattering medium, it is straightforward to follow a tomographic procedure: the light source is successively prepared in four pure polarization basis states of linear $(V, H, +45°)$ and circular (RHC) polarization, which are represented by four independent input Stokes vectors $\mathbf{S}_{\text{in}}$. For each of these input fields the corresponding Stokes vector $\mathbf{S}_{\text{out}}$, that represents the polarization state of the output field, is obtained by measuring the intensities of the scattered light in the same four polarization basis states. This procedure provides the 4×4 independent parameters required to determine the 16 elements $M_{\mu\nu}$ of the Mueller matrix in Eq. (5.1). Note that we actually employ two additional polarization basis states $(-45°, LHC)$ in our experiments and therefore perform 6×6 measurements, which allows us to reduce experimental errors by averaging within the over-complete data set.
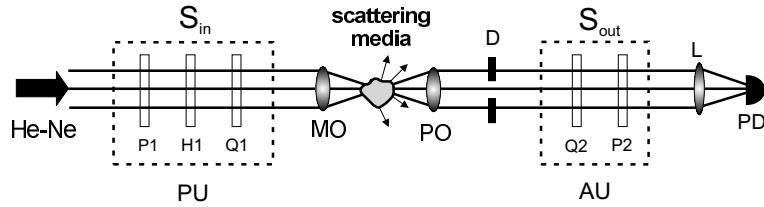

Figure 5.1: *Schematic of the polarization tomography set-up. A polarizer unit (PU), consisting of a fixed polarizer (P1), a half-wave plate (H1), and a quarter-wave plate (Q1) prepares the polarization input state. A microscope objective (MO) couples the light into the sample. The scattered light is collimated by a photographic objective (PO). An adjustable diaphragm (D) defines the amount of transverse spatial average to be performed at the detector. The analyzer unit (AU) consists of a quarter-wave plate (Q2) and a polarizer (P2). Lens (L) focuses the light coming from P2 into a photodiode (PD).*

The experimental scheme is illustrated in Fig. 5.1. The light source is a power-stabilized He-Ne laser at 632.8 nm wavelength. The input field is prepared by the polarizer unit (PU), consisting of a fixed polarizer (P1), a half-wave plate (H1), and a quarter-wave plate (Q1). A microscope objective (MO, $\times$ 50 magnification, $N.A. = 0.55$) couples the light into the sample. The scattered light is collimated by a standard photographic objective (PO, $f = 50\ mm$, $f^\sharp = 1.9$), followed by an adjustable diaphragm or pinhole (D) which fixes the number of detected spatial modes and thus defines the amount of transverse spatial averaging to be performed at the detector. The analyzer unit (AU) consists of a quarter-wave plate (Q2) and a polarizer (P2). Together with a focusing lens (L) and a photodiode (PD), it probes the polarization state of the scattered output field. As an estimate of the systematic error of the set-up, we measured the Mueller matrix of air (i.e. the identity matrix) and of well-known

deterministic optical elements such as wave plates. In all these cases, we found the deviations from the theoretically predicted matrix elements to be limited to $|\Delta M_{\mu\nu}| \leq 0.02$. We ascribe this mainly to angle-calibration errors as well as imperfections in the used wave plates. This experimental error can in turn be mapped to the corresponding error in the eigenvalues λ_i of H; in all cases we found $|\Delta\lambda_i| \leq 0.04$.

5.4 Scattering samples

The first category (a) of scattering samples that we used are *dynamic* scatterers where, e.g., Brownian motion induces temporal fluctuations within the detection integration time. Examples are milk, polystyrene micro-spheres suspended in water, optically active scattering media such as polymer-dispersed liquid crystals [57] and watery sugar solutions with suspended polystyrene micro-spheres (the micro-spheres were added to provide Mie scattering). The second category (b) consisted of *static* scatterers without temporal fluctuations: standard Lyot and wedge depolarizers [4], glass and polymer multimode optical fibers as well as optical polymer and holographic diffusers. Surface (holographic) diffusers produce a spread in the direction of propagation of the incident beam which is, on its own, hardly depolarizing. Therefore, in order to obtain considerable depolarization we combined them with birefringent wave plates of different thickness. See the caption of Fig. 5.2 for more details on the scattering samples. Several scatterer-specific tuning parameters, such as adjustable fiber bending radius, or dilution in the case of liquid samples, allowed us to realize a wide range of depolarizing media and to reveal details of their depolarizing properties. Additionally, by choosing different diaphragm diameters between 2 mm and 13 mm (far field full angular spread 2.3° and 14.6° respectively), we realized scattering systems which were described by different M_{eff}. By choosing a lower limit of 2 mm in the diaphragm diameter, special care was taken to select a sufficiently large number of speckles in the scattered output field (considering that step-index glass fiber with 50 μm core diameter showed the largest speckles of all our samples with a far field angular spread of $\approx 0.6°$).

5.5 Experimental results

Fig. 5.2 shows the measured polarization entropy (E_M) *vs.* the corresponding index of depolarization (D_M), for a large collection of scattering samples. The relatively small grey region corresponds to all physically realizable scattering processes [50]. This region is bounded and interdivided by solid curves, whose analytical expression were derived in Ref. [50]. The outermost curve connecting the cusp points **A** and **D** is special since it sets an upper bound for the entropy E_M^{max} for a given depolarizing power D_M, and it can be shown that it is associated with *isotropic* depolarizers [50]. As is apparent from the experimental data, our choice of samples allowed us to largely fill in the range of values (E_M, D_M), in good agreement with the predictions from Ref. [50]. Note, however, that we were not able to fill in the region below the inner curve connecting the points **A** and **C** in the (E_M, D_M)-plane with any data so far.

Some interesting structures are revealed by Fig. 5.2; the isotropy curve $E_M^{max}[D_M]$ is mainly covered by the dynamic scatterers (a) that we probed, as well as by polymer fibers,
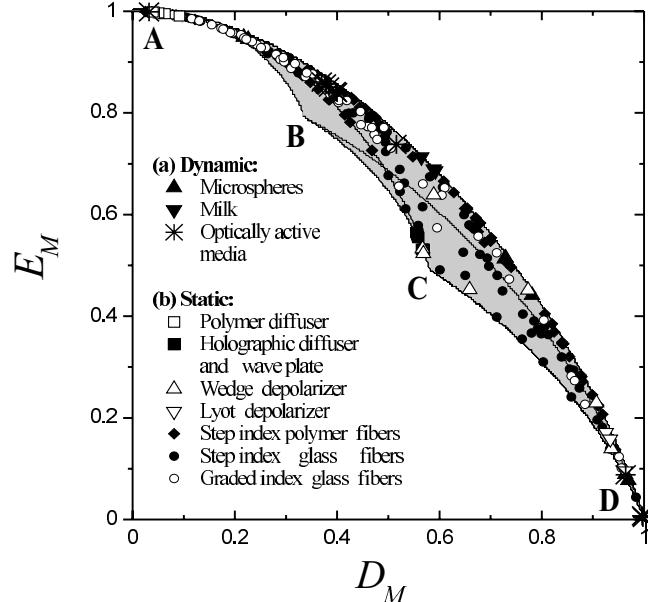
Figure 5.2: *Measured polarization entropy* (E_M) *vs. index of depolarization* (D_M) *for all samples. The theoretically possible parameter range in the* (E_M, D_M)*-plane is indicated by the grey-shaded area. Solid curves correspond to analytical boundaries predicted by theory. Cusp points are given by* $\mathbf{A} = (0, 1)$, $\mathbf{B} = (1/3, \log_4 3)$, $\mathbf{C} = (1/\sqrt{3}, 1/2)$, *and* $\mathbf{D} = (1, 0)$ *[50]. Details of samples (a)* **Dynamic***: polystyrene micro-spheres suspended in water (2 μm diameter, Duke Scientific Co., USA); milk diluted in water (fat particles* $\approx 2 - 3$ *μm [58]); sugar in watery micro-spheres suspension; polymer-dispersed liquid crystal (column thickness 2 mm, 0.1 mm and 10 μm, nematic liquid crystal E7 [57], chiral dope CB15, Merck, Germany); (b)* **Static***: polymer sheet diffusers (100 μm thickness, Zenith*^{TM}*, SphereOptics Hoffman GmbH, Germany); holographic light shaping diffusers (diffusing full angle* $\alpha = 0.5°$, $1°$, $5°$, *and* $10°$*, Physical Optics Co., USA); Quartz-wedge/Lyot depolarizers [4] (Halbo Optics, UK); step-index polymer optical fiber [59, 60] (N.A. = 0.55, core diameters 250 μm, 500 μm, 750 μm ESKA CK type, Mitsubishi Rayon, Japan); step-index glass optical fiber, (N.A. = 0.48, core diameters 200 μm, 400 μm, 600 μm FT-x-URT type, distributed by Thorlabs, Inc., USA); step-index glass optical fiber (N.A. = 0.22, core diameters 50 μm ASF50 type, distributed by Thorlabs, Inc., USA); step-index glass optical fiber (N.A. = 0.27, core diameters 62.5 μm GIF625 type, distributed by Thorlabs, Inc., USA).*

where a considerable amount of Rayleigh scattering at density fluctuations is present [59, 60]. On the other hand, the inner parts of the allowed (E_M, D_M) region, which are associated with anisotropic depolarizers, were covered by static samples (b), where the main depolarizing mechanism is given by the coupling between spatial and polarization degrees of freedom produced by the combination of multi-mode scattering with birefringence; an example of this is bending-induced birefringence in the glass optical fibers. The data obtained for samples longer than 50 cm (500 cm) in the case of polymer (glass) fibers, are close to the cusp point

A ($\lambda_{i=0,1,2,3} = 1/4$), which corresponds to total depolarization, while the data obtained for fibers shorter than 2 cm are close to cusp point **D** ($\lambda_0 = 1, \lambda_{i=1,2,3} = 0$), which corresponds to deterministic or non-depolarizing systems.

The wedge depolarizers resulted in a *non*-zero index of depolarization since they are designed to depolarize only a well defined linear input polarization [4], whereas our tomographic measurement procedure represents an average over *all* independent input polarizations. Additionally, we measured the depolarizing power of two identical wedges in cascade as a function of the relative angle α between their optical axis. In particular, complete depolarization was obtained for $\alpha = 45°$ and no depolarization occurred for $\alpha = 0°$ when the two wedges were compensated. Not surprisingly, the Lyot depolarizer was, within the experimental error, non-depolarizing since it is designed to depolarize a broadband light source, by coupling polarization with frequency degrees of freedom, while we operated with a monochromatic laser source.

5.6 Summary

In conclusion, the experimental data for our scatterers covered the theoretically allowed (E_M, D_M) domain almost completely and give thus evidence of the predicted depolarization universality in light scattering [50]. The quantities D_M and E_M provide insights into the particular depolarization mechanisms of the various media, and may provide a useful classification of optical scatterers for quantum applications, where depolarization is linked to decoherence [51].

CHAPTER 6

Tunable spatial decoherers for polarization-entangled photons

In this Chapter [1] we report a novel controllable source of spatial decoherence for twin-photons, based upon commercially available wedge depolarizers. This allows us to convert the polarization-entangled singlet state into a tunable mixed state. A full characterization of this mixed state, by means of quantum tomography, shows that such a spatial decoherer can be used for synthesizing Werner-like states on demand.

---

[1]Based on G. Puentes, D. Voigt, A. Aiello, and J. P. Woerdman, Opt. Lett. **31**, 2057 (2006).

6.1 Introduction

In the previous Chapters we analyzed polarization aspects of light scattering, in a classical context. This means, by using a classical source of light. Alternatively, in the remaining Chapters of this Thesis, we will analyze light scattering processes in a non-classical context. Again, this refers to the quantum nature of the light source. Specifically, for the experiments described in Chapters 6-9, we used polarization entangled photons as a light source.

Entanglement, the non-classical correlation between separate quantum systems, is considered a basic resource for quantum information applications including quantum teleportation [72], quantum cryptography [73], and quantum computation [74]. Most of these applications work best with quantum systems prepared in a pure maximally entangled state (i.e., a Bell state). However, practically available quantum systems are generally in mixed (non-pure) and non-maximally entangled states due to their unavoidable interaction with unobserved degrees of freedom which act as the environment. This interaction, in turn, induces decoherence and dissipation. Therefore, in recent years, much effort has been devoted to the characterization of mixed entangled states [75, 76] and to the formulation of appropriate separability criteria [77, 78].

From the experimental point of view, a consistent and systematic study of these aspects requires a reliable source of tunable decoherence, in order to engineer mixed entangled states in a controllable and reproducible way. In this context, creation and characterization of Werner states [79] and maximally entangled mixed states (MEMS) [80] based upon twin-photon generation by spontaneous parametric down conversion (SPDC) has been reported [81–85]. While Peters *et al.* [84] create these well-known families of mixed states by coupling polarization and frequency degrees of freedom (temporal decoherence), Barbieri *et al.* [85] make use of the peculiar spatial properties of their source of entangled photons to produce the desired states. In this Chapter we introduce commercially available quartz wedge depolarizers [4] as a novel source of tunable *spatial* decoherence for polarization-entangled photons. The twin-photon states are produced in a standard type-II configuration by SPDC [86] and characterized by means of quantum tomography [87]. This characterization shows that our spatial decoherer can be used to engineer Werner-like states in a reproducible manner. Our results provide evidence against the belief that spatially based decoherence is not suitable for exploring the twin-photon Hilbert space as it completely destroys entanglement [82].

6.2 Experimental scheme

The experimental set-up is shown in Fig. 6.1. A Krypton-ion laser at 413.1 nm pumps a 1-mm thick BBO crystal, where polarization-entangled photons are created by SPDC in a degenerate type II phase matching configuration at 826.2 nm. Single-mode fibers (SMF) are used as spatial filters to assure that the initial state is in a single transverse mode. Polarization controllers (PC) align the axes of the spurious birefringence along the SMFs in the SPDC crystal basis. The total retardation introduced by the SMFs and walk-off effects at the BBO crystal are compensated by additional BBO crystals (0.5 mm thick) in both signal and idler paths, together with a half-wave plate (HWP) [86]. The polarization analyzer used for quantum tomography consists of a quarter-wave plate (QWP) followed by a polarizer (P) in both arms.
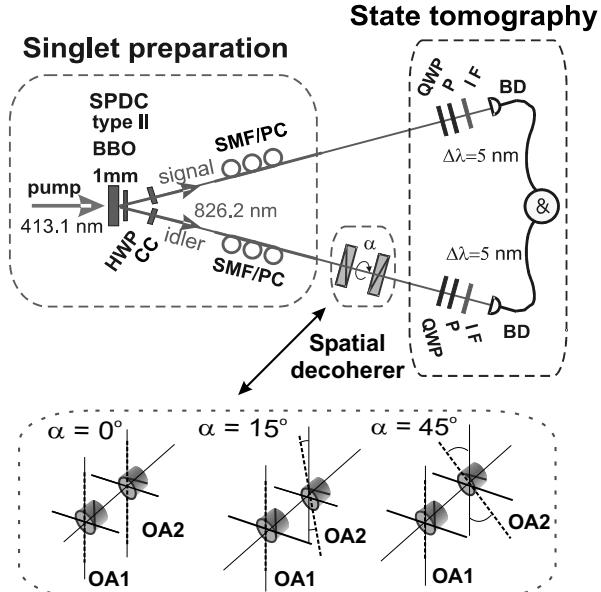
Figure 6.1: *Experimental scheme: a krypton-ion laser pumps a type-II BBO crystal. Walk-off effects are compensated by a half wave-plate (HWP) and two compensating crystals (CC). The down-converted photons are spatially filtered by single mode fibers (SMF). Additionally, interference filters (IF) are placed in both arms for bandwidth selection. A pair of wedge depolarizers in cascade (spatial decoherer) are placed in the idler path. The amount of decoherence can be controlled by varying the azimuthal angle (α) between the optical axes (OA1 and OA2) of the two wedges. The decohered twin-photon state is then analyzed by a quantum tomographic procedure by means of polarization analyzers (QWP and P) and "bucket" detectors (BD). Bottom box depicts three different settings for α.*

Additionally, $\Delta\lambda = 5$ nm interference filters (IF) are used for bandwidth selection. Finally, the photon pairs are detected in a multi-transverse mode fashion by using momentum-insensitive or "bucket" detectors (BD). Specifically, our photon counters (SPCM-AQR-1X, PerkinElmer TM) consisted of a silicon avalanche photodiode with a circular effective area of $d = 150 \ \mu$m diameter. The twin-photon state that is incident on the spatial decoherer is prepared in the singlet Bell state (see Fig. 6.2 (a)). The quality of this initial state (before the decoherer) has to be optimal, i.e., the state has to be maximally entangled and pure, in order to explore the full dynamic range with the tunable spatial decoherer.

Our tunable spatial decoherer consisted of two identical cascaded quartz-wedge depolarizers [4] (Halbo Optics, UK, model No. WDQ10M) placed at normal incidence to the idler photon (see Fig. 6.1). The beam was expanded by a magnifying telescope to approximately 1 cm, in order to maximize the depolarizing effect of the wedges. Note however, that within this beam diameter the wedges were classically not completely depolarizing. A classical

49

measurement of the average depolarizing power (*DP*) [44] of a single wedge probed with a collimated beam expanded to 1 cm ($\lambda = 811$ nm), revealed $DP \approx 0.664$ which shows 7% deviation from the ideal depolarizing power of a perfect wedge $DP = \sqrt{1/3} \approx 0.577$. Each quartz-wedge separately was contacted with a fused-silica counter wedge to minimize refraction. The azimuthal angle (α) between the optical axes (OA1 and OA2) of the two wedges was used as tuning parameter allowing us to engineer a broad range of mixed-entangled states, starting from states close to pure and maximally entangled for $\alpha = 0°$ (opposite wedges) and ending at states close to fully-mixed and non-entangled for $\alpha = 45°$ (see bottom box in Fig. 6.1).

6.3 The tomographically reconstructed polarization density matrices

The degree of entanglement and mixedness of the photon pairs were quantified by the tangle (*T*), i.e., the concurrence squared [88], and the linear entropy (S_L) [89]. These were calculated from the 4×4 polarization density matrix ρ of the scattered photons, by using $T(\rho) = (\max\{0, \lambda_1 - \lambda_2 - \lambda_3 - \lambda_4\})^2$, where $\lambda_1^2 \geq \lambda_2^2 \geq \lambda_3^2 \geq \lambda_4^2$ are the eigenvalues of $\rho(\sigma_2 \otimes \sigma_2)\rho^*(\sigma_2 \otimes \sigma_2)$, with σ_2 a Pauli matrix [88] and $S_L(\rho) = \frac{4}{3}[1 - \text{Tr}(\rho^2)]$. The density matrix ρ was in turn reconstructed via a quantum tomographic technique [87] by using $\{|H_1H_2\rangle, |H_1V_2\rangle, |V_1H_2\rangle, |V_1V_2\rangle\}$ as canonical basis. Here *H* and *V* represent the horizontal and vertical linear polarizations of the two photons, and the subscripts $\{1, 2\}$ label signal and idler, respectively. For ease of notation, subscripts will be omitted in the rest of this Chapter. Finally, all the measured data were processed by using a standard maximum likelihood estimation method [87]. In Fig. 6.2, we show the real part of some of our tomographically
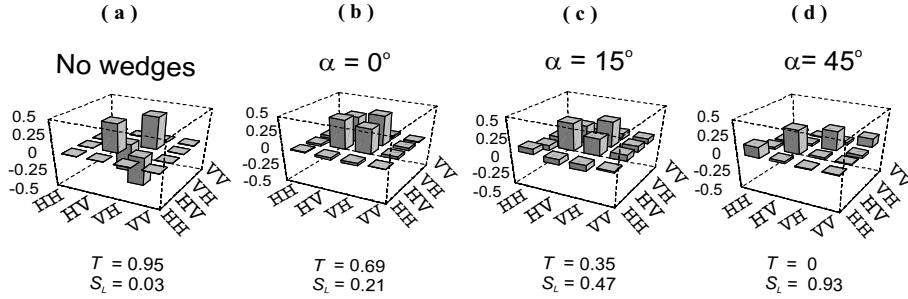

Figure 6.2: *Real part of the tomographically reconstructed polarization density matrix ρ in the $\{|H\rangle, |V\rangle\}$ basis, as well as calculated tangle T and linear entropy S_L for different relative angles (α) between the optical axes of the wedges: (a) empty set-up (no decoherers), the initial state is the singlet, (b) $\alpha = 0°$ anti-parallel wedges, (c) $\alpha = 15°$ and (d) $\alpha = 45°$, the state is a classical statistical mixture.*

reconstructed polarization density matrices ρ. Fig. 6.2 (a) shows a typical density matrix for the empty set-up, which is given by the singlet Bell-state $|\psi^-\rangle = (|HV\rangle - |VH\rangle)/\sqrt{2}$ with tangle $T \approx 95$ % and linear entropy $S_L \approx 3$ %, (b) corresponds to the measured den-

sity matrix when the wedges are anti-parallel oriented and the relative angle between their optical axis is $\alpha = 0°$. In this configuration the two wedges act as a wave-plate and only introduce a rotation in the polarization basis; this explains the change in sign of the initially negative off-diagonal elements of ρ. There is, however, a residual entanglement degradation for this setting ($T \approx 69$ %), which can be explained in terms of residual temporal decoherence by the wedges. Specifically, a chromatic polarization-interferometric analysis (see [90] for details) performed on a single wedge with a pencil-like beam (≈ 1 mm diameter), revealed a frequency-dependent phase retardation between horizontal and vertical polarizations of roughly $\pi/4$ (estimated at the center of the wedge aperture) within our detection bandwidth of $\Delta\lambda = 5$ nm. This detection bandwidth was chosen as a compromise between sufficiently low temporal decoherence and sufficiently large count rates (typical coincidence count rates were approximately 800/s). It should be noted that this initial entanglement degradation can in principle be reduced by designing the wedges on a thinner quartz substrate (the substrate width in our wedges was estimated [90] to be $\approx 300\mu m$).

Proceeding now to Fig. 6.2 (c), we show a typical density matrix for $\alpha = 15°$. From the values of S_L and T we see a further entanglement degradation to $T \approx 35$ %. Finally, in Fig. 6.2 (d) which corresponds to $\alpha = 45°$, the off-diagonal elements of ρ (i.e., the quantum correlations) have vanished and the state corresponds to a classical statistical mixture ($T = 0$). In Fig. 6.2 (d), we ascribe the deviation of the measured ρ from the identity to insufficient transverse spatial average at the wedges.

6.4 Tangle vs linear entropy plane

Fig. 6.3 shows measured data in the T-S_L plane. The dashed curve that limits the region of all physical states is given by the maximally entangled mixed states (MEMS) [80], while the solid curve is produced by Werner states [79]. Werner states $\rho_{Werner} = r|\psi^-\rangle\langle\psi^-| + (1-r)\frac{I}{4}$ represent an incoherent superposition of the singlet state $|\psi^-\rangle$ occurring with probability r ($0 \leq r \leq 1$) and the fully mixed state (i.e., the 4×4 identity I for the polarization degrees of freedom) occurring with probability $1 - r$. These states are useful to model depolarization in an isotropic noisy channel [65]. Experimental points correspond to different relative angles between the optical axes of the wedges ranging from $\alpha = 0°$ to $\alpha = 45°$, in incremental steps of $5°$. It is remarkable that all the data falls on the Werner curve within the experimental error indicated by error bars in Fig. 6.3 (see Chapter 7 for details); the latter were estimated from the standard deviation of a numerically generated Gaussian ensemble of photon counts centered around the measured data.
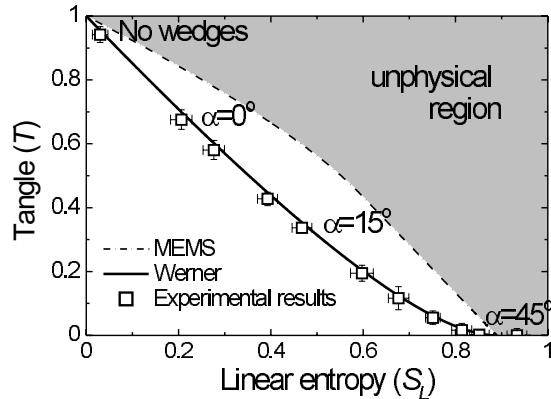
Figure 6.3: *Experimental data for spatial decoherers on the tangle (T)-linear entropy (S_L) plane. The grey area corresponds to unphysical density matrices. Dashed curve: Maximally entangled mixed states (MEMS), solid curve: Werner states. As the relative angle increases from $\alpha = 0°$ to $\alpha = 45°$, the initial singlet state is progressively decohered towards a maximally mixed state. Note that Werner states satisfy $T = 0$ for $S_L \geq 8/9$.*

6.5   Summary

In conclusion, in this Chapter we have implemented a simple tunable source of spatial decoherence with commercially available wedge depolarizers. The isotropically decohered output states fall on the Werner curve within the experimental error. We expect also pure input states of different symmetries than the singlet (i.e., the triplet), or different degrees of entanglement, to be decohered in a controllable manner by our experimental arrangement.

CHAPTER 7

Entangled mixed-state generation by twin-photon scattering

In this Chapter [1] we report experimental results on mixed-state generation by multiple scattering of polarization-entangled photon pairs created from parametric down-conversion. By using a large variety of scattering optical systems we have experimentally obtained entangled mixed states that lie upon and below the Werner curve in the linear entropy-tangle plane. We have also introduced a simple phenomenological model built on the analogy between classical polarization optics and quantum maps. Theoretical predictions from such model are in full agreement with our experimental findings.

7.1 Introduction

The study of spatial, temporal and polarization correlations of light scattered by inhomogeneous and turbid media has a history of more than a century [1]. Due to the high complexity of scattering media only single-scattering properties are known at a microscopic level [2]. Conversely, for multiple-scattering processes the emphasis is mainly on macroscopic theoretical descriptions of the correlation phenomena [92]. In most examples of the latter [93–96] the intensity correlations of the interference pattern generated by multiple-scattered light are explained in terms of *classical* wave-coherence. On the other hand, the recent availability of reliable single-photon sources has triggered the interest in *quantum* correlations of multiple-scattered light [8]. Generally speaking, quantum correlations of scattered photons depend on the quantum state of the light illuminating the sample. In Ref. [8], *spatial* quantum correlations of scattered light were analyzed for Fock, coherent and thermal input states.

In this Chapter we present the first experimental results on quantum polarization correlations of scattered photon pairs. Specifically, we study the entanglement content in relation to the polarization purity of multiple-scattered twin-photons, initially generated in a polarization-entangled state by spontaneous parametric down-conversion (SPDC). The initial entanglement of the input photon pairs will in general be degraded by multiple scattering. This can be understood by noting that the scattering process distributes the initial correlations of the twin-photons over the many spatial modes excited along the propagation in the medium. In the case of spatially inhomogeneous media the polarization degrees of freedom are coupled to the spatial degrees of freedom generating polarization dependent speckle patterns. If the spatial correlations of such patterns are averaged out by multi-mode detection, the polarization state of the scattered photon(s) is reduced to a mixture, and the resulting polarization-entanglement of the photon pairs is degraded with respect to the initial one. A related theoretical background was elaborated in [13, 14].

This Chapter is structured as follows: In section 7.2 we report our experiments on light scattering with entangled photons. First, we present our experimental set-up and briefly describe the many different optical systems that we used as scatterers. Next, we show our experimental results. The notions of generalized Werner and sub-Werner states are introduced to illustrate these results. In section 7.3 we introduce a simple phenomenological model for photon scattering that fully reproduces our experimental findings. Finally, in section 7.4 we draw our conclusions.

7.2 Experiments on light scattering with entangled photons

7.2.1 Experimental set-up

Our experimental set-up is shown in Fig. 7.1. A Krypton-ion laser at 413.1 nm pumps a 1 mm thick $\beta - BaB_2O_4$ (BBO) crystal, where polarization-entangled photon pairs at wavelength 826.2 nm are created by SPDC in degenerate type II phase-matching configuration [86]. Single-mode fibers (SMF) are used as spatial filters to assure that each photon of the initial SPDC pair travels in a single transverse mode. Spurious birefringence along the fibers is compensated by suitably oriented polarization controllers (PC). The total retardation introduced by the fibers and walk-off effects at the BBO crystal are compensated by com-

pensating crystals (CC: 0.5 mm thick BBO crystals) and half-wave plates ($\lambda/2$), in both signal and idler paths. In this way the initial two-photon state is prepared in the polarization singlet state $|\psi_s\rangle = (|HV\rangle - |VH\rangle)/\sqrt{2}$, where H and V are labels for horizontal and vertical polarizations of the two photons, respectively. The experimentally prepared ini-
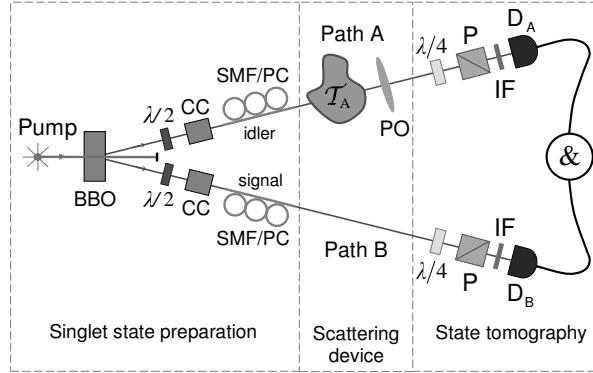

Figure 7.1: *Experimental scheme: After singlet preparation, the idler photon propagates through the scattering system $\mathcal{T}_A$. The polarization state of the scattered photon-pairs is then reconstructed via a quantum tomographic procedure (see text for details).*

tial singlet state ρ_s^{exp} has a fidelity [91] with the theoretical singlet state $\rho_s = |\psi_s\rangle\langle\psi_s|$ of $F(\rho^{\mathrm{tar}}, \rho^{\mathrm{exp}}) = |\mathrm{Tr}\left(\sqrt{\sqrt{\rho^{\mathrm{tar}}}\rho^{\mathrm{exp}}\sqrt{\rho^{\mathrm{tar}}}}\right)|^2 \sim 98\%$. In the second part of the experimental set-up the idler photon passes through the scattering device $\mathcal{T}_A$ before being collimated by a photographic objective (PO) with focal distance $f = 5$ cm. The third and last part of the experimental set-up, consists of two tomographic analyzers (one per photon), each made of a quarter-wave plate ($\lambda/4$) followed by a linear polarizer (P). Such analyzers permit a full tomographic reconstruction, via a maximum-likelihood technique [87], of the two-photon state. Additionally, interference filters (IF) put in front of each detector ($\Delta\lambda = 5$ nm) provide for bandwidth selection. Detectors D_A and D_B are "bucket" detectors, that is they do not distinguish which spatial mode a photon comes from, thus each photon is detected in a *mode-insensitive* way.

7.2.2 Scattering devices

All the scattering optical systems that we used were located in the path of only *one* of the photons of the entangled-pair (the idler one), as shown in Fig. 7.1. For this reason, we refer to such systems as *local* scatterers. Such scatterers can be grouped in three general categories according to the optical properties of the media they are made of [44] :

Type I Purely depolarizing media, or diffusers. Such media do not affect directly the polarization state of the impinging light but change the spatial distribution of the impinging electromagnetic field.

Type II Birefringent media, or retarders. These media introduce a polarization-dependent *delay* between different components of the electromagnetic field.

Type III Dichroic media, or diattenuators. Such media introduce polarization-dependent *losses* for the different components of the electromagnetic field.

Type I scattering systems produce an isotropic spread in the momentum of the impinging photons. Examples of such scattering devices are: spherical-particle suspensions (such as milk or polymer micro-spheres), polymer and glass multi-mode fibers and surface diffusers. Type II scattering systems are made of birefringent media, which introduce an optical axis that breaks polarization-isotropy. Birefringence can be classified as "material birefringence" when it is an intrinsic property of the bulk medium (for example a birefringent wave-plate), and as "topological birefringence" when it is induced by a special geometry of the system that generates polarization-anisotropy, an example of a system with topological birefringence is an array of cylindrical particles. Finally, type III scattering systems are made of dichroic media that produce polarization-dependent photon absorbtion. Examples of such devices are commonly used polarizers. A systematic characterization of all the scattering devices that we used was given in Ref. [44].

7.2.3 Experimental results
in the tangle versus linear entropy plane

The degree of entanglement and the degree of mixedness of the scattered photon pairs can be quantified by the tangle (T), namely, the concurrence squared [88], and the linear entropy (S_L) [89]. These quantities were calculated from the 4×4 polarization two-photon density matrix ρ, by using $T(\rho) = (\max\{0, \sqrt{\lambda_1} - \sqrt{\lambda_2} - \sqrt{\lambda_3} - \sqrt{\lambda_4}\})^2$, where $\lambda_1 \geq \lambda_2 \geq \lambda_3 \geq \lambda_4 \geq 0$ are the eigenvalues of $\rho(\sigma_2 \otimes \sigma_2)\rho^*(\sigma_2 \otimes \sigma_2)$, where $\sigma_2 = \begin{pmatrix} 0 & -i \\ i & 0 \end{pmatrix}$, and $S_L(\rho) = \frac{4}{3}[1 - \text{Tr}(\rho^2)]$.

Figures 7.2 (a) and (b) show experimental data reported on the linear entropy-tangle plane. The position of each experimental point in such plane has been calculated from a tomographically reconstructed [87] two-photon density matrix ρ^{exp}. The uniform grey area corresponds to non-physical states [80]. The dashed curve that bounds the physically admissible region from above is generated by the so-called maximally entangled mixed states (MEMS) [84, 85]. The lower continuous curve is produced by the Werner states [79] of the form: $\rho_W = p\rho_s + \frac{1-p}{4}I_4$, $(0 \leq p \leq 1)$, where I_4 is the 4×4 identity matrix. Figure 7.2 (a) shows experimental data generated by isotropic scatterers (type I). Specifically, our type I scatterers consisted of the following categories. (i) Suspensions of milk and micro-spheres in distilled water, where the sample dilution was varied to obtain different points; (ii) Multimode glass and polymer fibers, where the tuning parameter exploited to obtain different points was the length of the fiber (cut-back method); (iii) Surface diffusers, where the full width scattering angle was used as tuning parameter. It should be noted that suspensions of milk and micro-spheres are *dynamic* media, where Brownian motion of the micro-particles induces temporal fluctuations within the detection integration time [44].

In Fig. 7.2 (a), the experimental point at the top-left corner (nearby $T = 1$, $S_L = 0$), is generated by the un-scattered initial singlet state. The net effect of scattering systems with increasing thickness is to shift the initial datum toward the bottom-right corner ($T = 0$, $S_L = 1$), that corresponds to a fully mixed state.

Figure 7.2 (b) displays experimental data generated by birefringent scattering systems
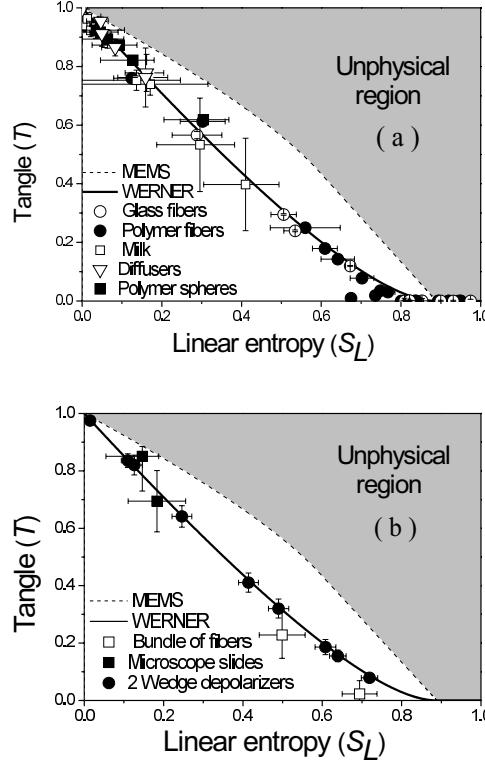
Figure 7.2: *Experimental data in the linear entropy-tangle (S_L-T) plane. The grey area corresponds to unphysical density matrices. Dashed upper curve: Maximally entangled mixed states (MEMS), continuous lower curve: Werner states. (a) Polarization-isotropic scatterers (type I). (b) Birefringent scatterers (type II).*

(type II). As an example of a system with "material birefringence" we used a pair of wedge depolarizers in cascade [4]. Different experimental points where obtained by varying the relative angle between the optical axis of the two wedges [97] (see Chapter 6, this Thesis). The systems with "topological birefringence" we considered consisted of two different devices: (i) The first one was a bundle of parallel optical fibers [98]. Translational invariance along the fibers axes restricts the direction of the wave-vectors of the scattered photons in a plane orthogonal to the common axis of the fibers. (ii) The second device was a stack of parallel microscope slides (with uncontrolled air layers in between). This optical system is depolarizing because it amplifies any initial spread in the wave-vector of the impinging photon. This photon enters via a single-mode-fiber (numerical aperture $NA = 0.12$), from one side of the stack and travels in a plane parallel to the slides.

In Fig. 7.3, experimental data generated by dichroic scattering systems (type III) are shown. We used: (i) Surface diffusers followed by a stacks of microscope slides at the Brewster angle and (ii) Commercially available polaroid sheets with manually-added sur-

face roughness on its front surface to provide for wave-vector spread. All data thus obtained fall below the Werner curve, generating what we called sub-Werner states, namely states with a lower value of tangle (T) than a Werner state, for a given value of the linear entropy (S_L).
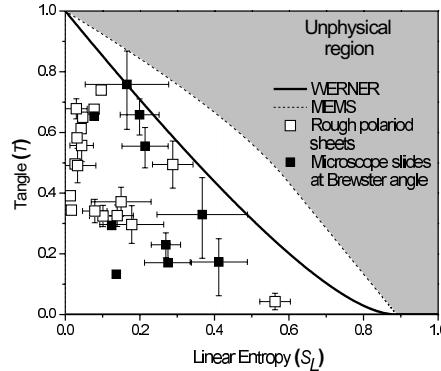

Figure 7.3: *Experimental data generated by dichroic scattering systems (type III).*

In summary, Figs. 7.2 (a)-(b) show that all data generated by type I and II scattering systems fall on the Werner curve, within the experimental error; while data generated by scattering samples type III, which are presented in Fig. 7.3, lay below the Werner curve. In Section III we shall present a simple theoretical interpretation of such results.

7.2.4 Error estimate

In order to estimate the errors in our measured data, we numerically generated 16 Monte Carlo sets N_i ($i = 1, \ldots, 16$) of 10^3 simulated photon counts, corresponding to each of the 16 actual coincidence count measurements $\{n_i^{\exp}\}$ ($i = 1, \ldots, 16$) required by tomographic analysis to reconstruct a single two-photon density matrix. Each set N_i had a Gaussian distribution centered around the mean value $\mu_i = n_i^{\exp}$, with standard deviation $\sigma_i = \sqrt{n_i^{\exp}}$. The sets N_i where created by using the "NormalDistribution" built-in function of the program Mathematica 5.2. Once we generated the 16 Monte Carlo sets N_i, we reconstructed the corresponding 10^3 density matrices using a maximum likelihood estimation protocol, to assure that they could represent physical states. Finally, from this ensemble of matrices we calculated the average tangle T^{av} and linear entropy S_L^{av}. The error bars were estimated as the absolute distance between the mean quantities (av) and the measured ones (exp): $\sigma_T = |T^{\exp} - T^{\mathrm{av}}|$, $\sigma_{S_L} = |S_L^{\exp} - S_L^{\mathrm{av}}|$. It should be noted that this procedure produces an overestimation of the experimental errors. In the cases where part of the overestimated error bars fell into the unphysical region, the length of such bars was limited to the border of the physically allowed density matrices.

7.2.5 Generalized Werner states

Close inspection of the reconstructed density matrices generated by type II scattering systems revealed that in some cases the measured states represented a generalized form of Werner states. These are equivalent to the original Werner states ρ_W with respect to their values of T and S_L, but the form of their density matrices is different. Werner states ρ_W of two qubits were originally defined [79] as such states which are $U \otimes U$ invariant: $\rho_W = U \otimes U \rho_W U^\dagger \otimes U^\dagger$. Here $U \otimes U$ is any symmetric separable unitary transformation acting on the two qubits. The generalized Werner states ρ_{GW} we experimentally generated, can be obtained from ρ_W by applying a *local* unitary operation V acting upon only one of the two qubits: $\rho_{GW} = V \otimes I \rho_W V^\dagger \otimes I$, where $I = \begin{pmatrix} 1 & 0 \\ 0 & 1 \end{pmatrix}$, and

$$V(\alpha, \beta, \gamma) = \begin{pmatrix} e^{-\frac{i}{2}(\alpha+\beta)} \cos \gamma/2 & -e^{-\frac{i}{2}(\alpha-\beta)} \sin \gamma/2 \\ e^{\frac{i}{2}(\alpha-\beta)} \sin \gamma/2 & e^{\frac{i}{2}(\alpha+\beta)} \cos \gamma/2 \end{pmatrix}, \tag{7.1}$$

where α, β, γ can be identified with the three Euler angles characterizing an ordinary rotation in $\mathbb{R}^3$ [65]. These generalized Werner states have the same values of T and S_L as the original ρ_W (since a local unitary transformation does not affect neither the degree of entanglement nor the degree of purity) but are no longer invariant under unitary transformations of the form $U \otimes U$. By using Eq. (7.1), we calculated the average maximal fidelity of the measured states ρ_{GW}^{exp} with the target generalized Werner states $\rho_{GW}^{\text{th}}(p, \alpha, \beta, \gamma)$. We found $\bar{F}(\rho_{GW}^{\text{exp}}, \rho_{GW}^{\text{th}}) \approx 96\%$, revealing that our data are well fitted by this four-parameter class of generalized Werner states.

7.3 The phenomenological model
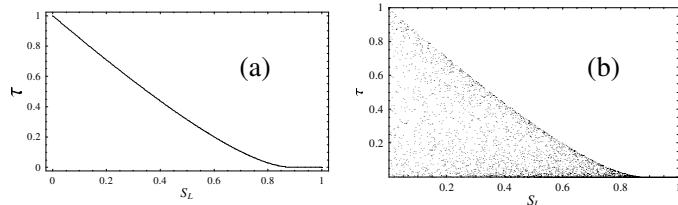
Figure 7.4: *Numerical simulation for our phenomenological model. (a) Isotropic and birefringent scattering, (b) dichroic scattering.*

In Ref. [15], a theoretical study of the analogies between classical linear optics and quantum maps was given. Within this theoretical framework it is possible to build a simple phenomenological model capable of explaining all our experimental results. To this end let us

consider the experimental set-up represented in Fig. 7.1. The linear optical scattering element $\mathcal{T}_A$ inserted across path A can be *classically* represented by some Mueller matrix $\mathscr{M}$ which describes its polarization-dependent interaction with a classical beam of light. $\mathscr{M}$ is also known as the Mueller matrix in the Standard matrix basis [71] and it is simply related to the more commonly used real-valued Mueller matrix M [101] via the change of basis matrix $\Lambda^{\dagger}$

$$M = \Lambda^{\dagger} \mathscr{M} \Lambda. \tag{7.2}$$

However, $\mathcal{T}_A$ can also be represented by a linear, completely positive, local *quantum* map $\mathscr{E} : \rho \to \mathscr{E}[\rho]$, which describes the interaction of the scattering element with a two-photon light beam encoding a pair of polarization qubits. These qubits are, in turn, represented by a 4×4 density matrix ρ. Since $\mathcal{T}_A$ interacts with only one of the two photons, the map $\mathscr{E}$ is said to be *local* and it can be written as $\mathscr{E} = \mathscr{E}_A \otimes \mathscr{I}$, where $\mathscr{E}_A$ is the single-qubit (or single-photon) quantum map representing $\mathcal{T}_A$, and $\mathscr{I}$ is the single-qubit identity map.

It can be shown that the classical Mueller matrix $\mathscr{M}$ and the single-qubit quantum map $\mathscr{E}_A$ are univocally related. Specifically, if with $\mathscr{M}$ we denote the complex-valued Mueller matrix written in the standard basis, then the following decomposition holds:

$$\mathscr{M} = \sum_{\mu=0}^{3} \lambda_{\mu} T_{\mu} \otimes T_{\mu}^{*}, \tag{7.3}$$

where $\{T_{\mu}\}$ is a set of four 2×2 Jones matrices, each representing a non-depolarizing linear optical element in classical polarization optics, and $\{\lambda_{\mu}\}$ are the four non-negative eigenvalues of the "dynamical" matrix H associated to $\mathscr{M}$.

Given Eq. (7.3), it is possible to show that the two-qubit quantum map $\mathscr{E}$ can be written as

$$\rho_{\mathscr{E}} = \mathscr{E}[\rho] \propto \sum_{\mu=0}^{3} \lambda_{\mu} T_{\mu} \otimes I \, \rho \, T_{\mu}^{\dagger} \otimes I, \tag{7.4}$$

where the proportionality symbol "$\propto$" on the right hand side of Eq. (7.4) accounts for a possible renormalization to ensure $\mathrm{Tr}(\rho_{\mathscr{E}}) = 1$. Such renormalization becomes necessary when $\mathcal{T}_A$ presents polarization-dependent losses (i.e., dichroism). We anticipate that when such re-normalization is necessary the map is considered non-trace preserving. We shall discuss this issue in detail in Chapter 9.

With these ingredients, a phenomenological polarization-scattering model can be built as follows. First we use the polar decomposition [99] to write an arbitrary Mueller matrix $\mathscr{M} = \mathscr{M}_{\Delta} \mathscr{M}_B \mathscr{M}_D$, where $\mathscr{M}_{\Delta}$, $\mathscr{M}_B$ and $\mathscr{M}_D$ represent a purely depolarizing element, a birefringent (or retarder) element, and a dichroic (or diattenuator) element, respectively. Specific analytical expressions for $\mathscr{M}_{\Delta}$, $\mathscr{M}_B$ and $\mathscr{M}_D$ can be found in the literature [4]. Second, we use Eq. (7.3) to find the quantum maps corresponding to $\mathscr{M}_{\Delta}$, $\mathscr{M}_B$ and $\mathscr{M}_D$ and, by using such maps, we calculate the scattered two-photon state $\rho_{\mathscr{E}}$. In our experimental realizations we used isotropic scatterers $\mathscr{M}_{IS} = \mathscr{M}_{\Delta}$ with isotropic depolarization factor $0 \leq \Delta < 1$, birefringent scattering media $\mathscr{M}_{BS}$, described in terms of the product of a purely birefringent

medium $\mathscr{M}_B$ and an isotropic depolarizer $\mathscr{M}_\Delta$, i.e. $\mathscr{M}_{BS} = \mathscr{M}_B\mathscr{M}_\Delta$, and finally, dichroic scattering media $\mathscr{M}_{DS} = \mathscr{M}_D\mathscr{M}_\Delta$, which are in turn described by a product of a purely dichroic medium $\mathscr{M}_D$ and a purely depolarizing medium $\mathscr{M}_\Delta$. It should be noted that these product decompositions are not unique. Other decompositions with different orders are possible but the elements of each matrix might change, since the matrices $\mathscr{M}_\Delta$, $\mathscr{M}_B$ and $\mathscr{M}_D$ do not commute.

Filling in the above expressions with random numbers selected from suitably chosen ranges, we simulated all scattering processes occurring in our experiments. Fig. 7.4 shows a numerical simulation of the scattered states in the tangle vs. linear entropy plane, obtained with the singlet two-photon state as input state. Fig. 7.4 (a) corresponds to isotropic and birefringent scatterers, and Fig. 7.4 (b) to dichroic scatterers. The qualitative agreement between this model and the experimental results shown in Fig. 7.2 and Fig. 7.3 is manifest.

7.4 Summary

In summary, in this Chapter we have presented experimental results on entanglement properties of scattered photon-pairs for three varieties of optical scattering systems. In this way we were able to generate two distinct types of two-photon mixed states; namely Werner-like and sub-Werner-like states. Moreover, we have introduced a simple phenomenological model based onto the analogy between classical polarization optics and quantum mechanics of qubits, that fully reproduces our experimental findings. In the case of sub-Werner states, the phenomenological model represents a non-trace preserving quantum map. Such description might be considered controversial since a non-trace preserving local map can in principle lead to violation of causality when it describes the evolution of a composite system made of two spatially separate subsystems [100]. However, we argue that our measured states do not violate the signaling condition as they are post-selected by the coincidence measurement, a procedure which involves classical communication between two detectors (see Chapter 9, this Thesis). Finally, we expect it to be possible to create states *above* the Werner curve (in particular MEMS) [84, 85], by post-selective detection when acting on a single photon [100]. This will be discussed in the next Chapter.

We gratefully acknowledge M. B. van der Mark for making available the bundle of parallel fibers [98].
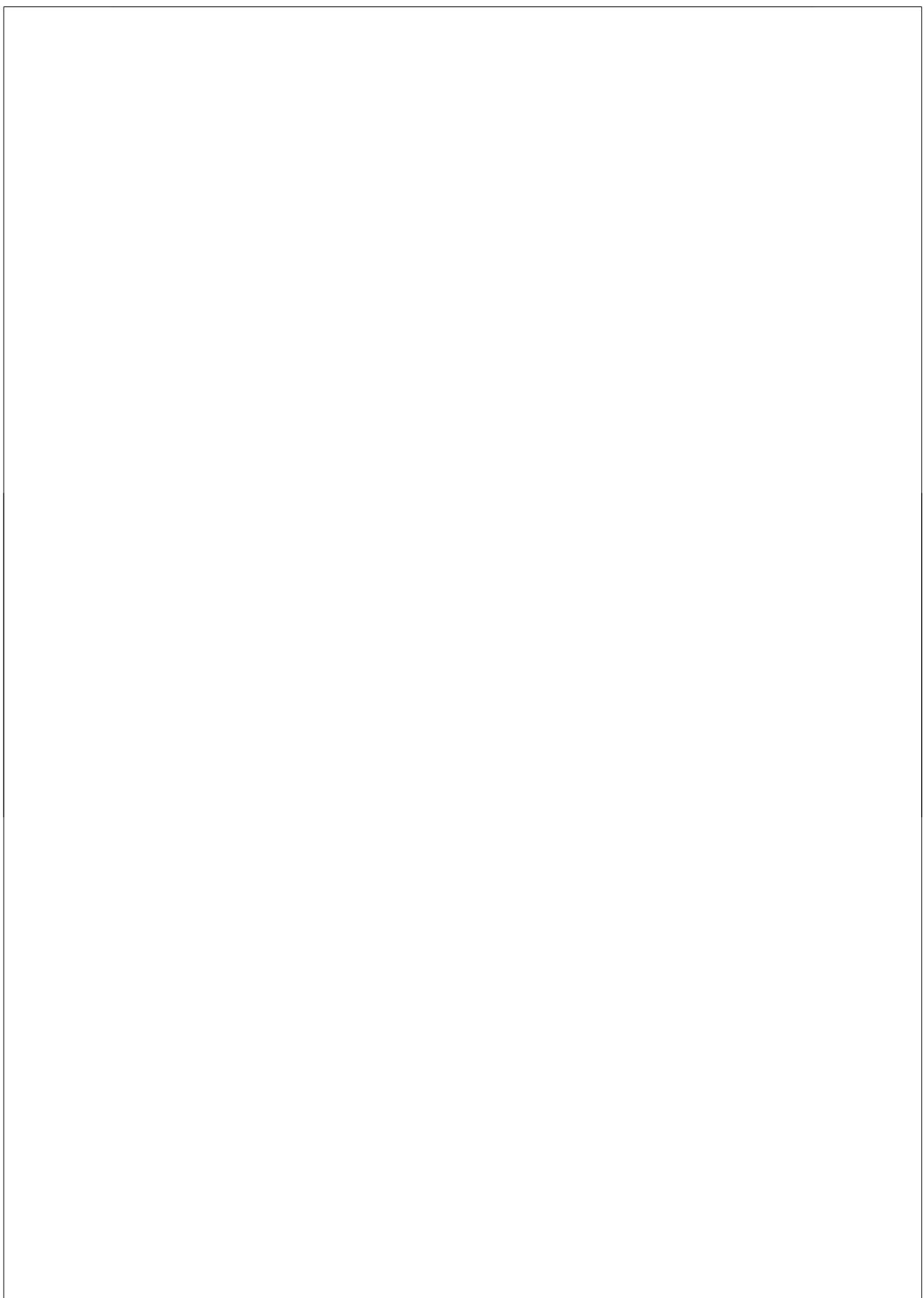
CHAPTER **8**

Maximally entangled mixed-state generation via local operations

In this Chapter [1] *we present a general theoretical method to generate maximally entangled mixed states of a pair of photons initially prepared in the singlet polarization state. This method requires only local operations upon a single photon of the pair and exploits spatial degrees of freedom to induce decoherence. We report experimental confirmation of these theoretical results.*

---

[1] Based on A. Aiello, G. Puentes, D. Voigt, and J. P. Woerdman, quant-ph/0603182 (submitted to Phys. Rev. A).

8.1 Introduction

Entanglement is perhaps the most puzzling feature of quantum mechanics and in the last two decades it became the key resource in quantum information processing [65]. Entangled qubits prepared in pure, maximally entangled states are required by many quantum-information processes. However, in a mundane world, a pure maximally entangled state is an idealization as, e.g., a plane wave in classical optics. In fact, interaction of qubits with the environment leads to decoherence that may cause a pure entangled state to become less pure (mixed) and less entangled. Thus, any *realistic* quantum-communication/computation protocol must cope with entangled mixed states and it is desirable to attain the maximum amount of entanglement for a given degree of mixedness. States that fulfill this condition are called maximally entangled mixed states (MEMS) and, recently, they have been the subject of several papers (see, e.g., [84, 85] and references therein). In this Chapter we propose a new method to create MEMS from a pair of photons initially prepared in the singlet polarization state.

Kwiat and coworkers [84] were the first to achieve MEMS using photon pairs from spontaneous parametric down conversion (SPDC). They induced decoherence in SPDC pairs initially prepared in a pure entangled state by coupling polarization and frequency degrees of freedom of the photons. At the same time, a somewhat different scheme was used by De Martini and coworkers [85] who instead used the spatial degrees of freedom of SPDC photons to induce decoherence. However, both the Kwiat and the De Martini method require operations on *both* photons of the SPDC pair. On the contrary, our technique has the advantage to require only *local* operations upon one of the two photons.

This Chapter is structured as follows: In the first part we show the relation existing between a one-qubit quantum map and a classical-optics setup on the laboratory bench. In the second part, we exploit this knowledge to design a simple linear-optical set-up to generate MEMS from a pair of photons via local operations and postselection. Finally, in the third part we provide an experimental demonstration of our method, using entangled photons from parametric down-conversion.

8.2 Classical linear optics and quantum maps

We begin by giving a brief description of the connection between classical polarization optics and quantum mechanics of qubits, as recently put forward by several authors [64, 66].

Most textbooks on classical optics introduce the concept of polarized and unpolarized light with the help of the Jones and Stokes-Mueller calculi, respectively [101]. In these calculi, the description of classical polarization of light is formally identical to the quantum description of pure and mixed states of two-level systems, respectively [69, 70]. In the Jones calculus, the electric field of a quasi-monochromatic *polarized* beam of light which propagates close to the z-direction, is represented by a complex-valued two-dimensional vector, the so-called *Jones vector* $\mathbf{E} \in \mathbb{C}^2 : \mathbf{E} = E_0 \boldsymbol{x} + E_1 \boldsymbol{y}$, where the three real-valued unit vectors $\{\boldsymbol{x}, \boldsymbol{y}, \boldsymbol{z}\}$ define an orthogonal Cartesian frame. The same amount of information about the state of the field is also contained in the 2×2 matrix J of components $J_{ij} = E_i E_j^*$, $(i, j = 0, 1)$, which is known as the *coherency matrix* of the beam [6]. The matrix J is Hermitean and pos-

itive semidefinite

$$J^\dagger = J, \qquad (\mathbf{v}, J\mathbf{v}) = |(\mathbf{v}, \mathbf{E})|^2 \geq 0, \tag{8.1}$$

for all $\mathbf{v} \in \mathbb{C}^2$. Further, J has the projection property $J^2 = J\,\mathrm{Tr}J$, and its trace equals the total intensity of the beam: $\mathrm{Tr}J = |E_0|^2 + |E_1|^2$. If we choose the electric field units in such a way that $\mathrm{Tr}J = 1$, then J has the same properties of a *density matrix* representing a two-level quantum system in a *pure* state. In classical polarization optics the coherency matrix description of a light beam has the advantage, with respect to the Jones vector representation, of generalizing to the concept of *partially polarized* light. Formally, the coherency matrix of a partially polarized beam of light is characterized by the properties detailed in Eq. 8.1, while the projection property is lost. In this case J has the same properties of a density matrix representing a two-level quantum system in a *mixed* state. Coherency matrices of partially polarized beams of light may be obtained by tacking linear combinations $\sum_N w_N J_N$ of coherency matrices J_N of polarized beams, where the index N runs over an *ensemble* of field configurations and $w_N \geq 0$. It should be noted that the off-diagonal elements of the coherency matrix are complex-valued and, therefore, not directly observables. However, as any 2×2 matrix, J can be written either in the Pauli basis X_α [102]:

$$X_0 \;\equiv\; \tfrac{1}{\sqrt{2}} \begin{pmatrix} 1 & 0 \\ 0 & 1 \end{pmatrix}, \qquad X_1 \;\equiv\; \tfrac{1}{\sqrt{2}} \begin{pmatrix} 0 & 1 \\ 1 & 0 \end{pmatrix},$$
$$X_2 \;\equiv\; \tfrac{1}{\sqrt{2}} \begin{pmatrix} 0 & -i \\ i & 0 \end{pmatrix}, \qquad X_3 \;\equiv\; \tfrac{1}{\sqrt{2}} \begin{pmatrix} 1 & 0 \\ 0 & -1 \end{pmatrix}, \tag{8.2}$$

or in the Standard basis Y_α:

$$Y_0 \;\equiv\; \begin{pmatrix} 1 & 0 \\ 0 & 0 \end{pmatrix}, \qquad Y_1 \;\equiv\; \begin{pmatrix} 0 & 1 \\ 0 & 0 \end{pmatrix},$$
$$Y_2 \;\equiv\; \begin{pmatrix} 0 & 0 \\ 1 & 0 \end{pmatrix}, \qquad Y_3 \;\equiv\; \begin{pmatrix} 1 & 0 \\ 0 & 1 \end{pmatrix}, \tag{8.3}$$

as

$$J = \sum_{\alpha=0}^{3} x_\alpha X_\alpha = \sum_{\beta=0}^{3} y_\beta Y_\beta, \tag{8.4}$$

where $x_\alpha = \mathrm{Tr}(X_\alpha J) \in \mathbb{R}$, $y_\beta = \mathrm{Tr}(Y_\beta^\dagger J) \in \mathbb{C}$ and, from now on, all Greek indices $\alpha, \beta, \mu, \nu, \ldots$, take the values $0, 1, 2, 3$. The four real coefficients x_α, called the *Stokes parameters* of the beam, can be actually measured thus relating J with observables of the optical field. Conversely, the four complex coefficients y_β are not directly measurable but have the advantage to furnish a particularly simple representation of the matrix J since $y_0 = J_{00}$, $y_1 = J_{01}$, $y_2 = J_{10}$, $y_3 = J_{11}$. The two different representations x_α and y_β are related via the matrix $\Lambda^\dagger$

$$\Lambda^\dagger = \frac{1}{\sqrt{2}} \begin{pmatrix} 1 & 0 & 0 & 1 \\ 0 & 1 & 1 & 0 \\ 0 & i & -i & 0 \\ 1 & 0 & 0 & -1 \end{pmatrix}, \tag{8.5}$$

such that $x_\alpha = \sum_\beta \Lambda^\dagger_{\alpha\beta} y_\beta$, where $\Lambda^\dagger_{\alpha\beta} = \mathrm{Tr}(X_\alpha Y_\beta)$, and $\Lambda\Lambda^\dagger = I_4 = \Lambda^\dagger\Lambda$.

8.2.1 Polarization-transforming linear optical elements

When a beam of light passes through an optical system its state of polarization may change. Within the context of polarization optics, a linear optical element is any device that performs a *linear* transformation upon the electric field components of an input light beam. Half- and quarter-wave plates, couplers, phase shifters, beam splitters, polarizers, etc., are all examples of such devices. The class of linear optical elements comprises both non-depolarizing and depolarizing devices. Roughly speaking, a *non-depolarizing* linear optical element transforms a polarized input beam into a polarized output beam. On the contrary, a *depolarizing* linear optical element transforms a polarized input beam into a partially polarized output beam [48]. A non-depolarizing device may be represented by a single 2×2 complex matrix T, the *Jones matrix*, such that $J_{\text{in}} \to J_{\text{out}} = T J_{\text{in}} T^\dagger$. In this Thesis we consider only *passive* (namely, non-amplifying) optical devices for which the relation $\text{Tr}J_{\text{out}} \le \text{Tr}J_{\text{in}}$ holds. There exist two fundamental kinds of non-depolarizing optical elements, namely *retarders* and *diattenuators*; any other non-depolarizing element can be modelled as a retarder followed by a diattenuator [99]. A retarder (also known as *birefringent* element) changes the *phases* of the two components of the electric-field vector of a beam, and may be represented by a unitary Jones matrix T_U. A diattenuator (also known as *dichroic* element) instead, changes the *amplitudes* of components of the electric-field vector (polarization-dependent losses), and may be represented by a Hermitean Jones matrix T_H.

Let $\mathscr{T}_{\text{ND}}$ denote a generic non-depolarizing device represented by the Jones matrix T, such that $J_{\text{in}} \to J_{\text{out}} = T J_{\text{in}} T^\dagger$. We can rewrite explicitly this relation in terms of components as:

$$(J_{\text{out}})_{ij} = T_{ik} T_{jl}^* (J_{\text{in}})_{kl}, \tag{8.6}$$

where, from now on, summation over repeated indices is understood and all Latin indices $i, j, k, l, m, n, \ldots$ take the values 0 and 1. Since $T_{ik} T_{jl}^* = (T \otimes T^*)_{ij,kl} \equiv \mathscr{M}_{ij,kl}$ we can rewrite Eq. (8.6) as:

$$(J_{\text{out}})_{ij} = \mathscr{M}_{ij,kl} (J_{\text{in}})_{kl}, \tag{8.7}$$

where $\mathscr{M} = T \otimes T^*$ is a 4×4 complex-valued matrix representing the device $\mathscr{T}_{\text{ND}}$, and the symbol $\otimes$ denotes the ordinary Kronecker matrix product. $\mathscr{M}$ is also known as the Mueller matrix in the Standard matrix basis [71] and it is simply related to the more commonly used real-valued Mueller matrix M [101] via the change of basis matrix $\Lambda^\dagger$

$$M = \Lambda^\dagger \mathscr{M} \Lambda. \tag{8.8}$$

For the present case of a non-depolarizing device, M is named as *Mueller-Jones* matrix. From Eqs. (8.4, 8.7) it readily follows that we can indifferently represent the transformation operated by $\mathscr{T}_{\text{ND}}$ either in the Standard or in the Pauli basis as:

$$y_\alpha^{\text{out}} = \sum_{\beta=0}^{3} \mathscr{M}_{\alpha\beta} y_\beta^{\text{in}}, \quad \text{or} \quad x_\alpha^{\text{out}} = \sum_{\beta=0}^{3} M_{\alpha\beta} x_\beta^{\text{in}}, \tag{8.9}$$

respectively.

With respect to the Jones matrix T, the Mueller matrices $\mathscr{M}$ and M have the advantage of generalizing to the representation of *depolarizing* optical elements. Mueller matrices of depolarizing devices may be obtained by taking linear combinations of Mueller-Jones matrices

of non-depolarizing elements as:

$$\mathscr{M} = \sum_A p_A \mathscr{M}_A = \sum_A p_A T_A \otimes T_A^*, \tag{8.10}$$

where $p_A \geq 0$. Index A runs over an ensemble of Mueller-Jones matrices $\mathscr{M}_A = T_A \otimes T_A^*$, each representing a non-depolarizing device. The real-valued matrix M corresponding to $\mathscr{M}$ can be easily calculated by using Eq. (8.8) [71]. In the current literature M is often written as [99]:

$$M = \begin{pmatrix} M_{00} & \mathbf{d}^T \\ \mathbf{p} & W \end{pmatrix}, \tag{8.11}$$

where $\mathbf{p} \in \mathbb{R}^3$, $\mathbf{d} \in \mathbb{R}^3$, are known as the *polarizance vector* and the *diattenuation vector* (superscript T indicates transposition), respectively, and W is a 3×3 real-valued matrix. Note that $\mathbf{p}$ is zero for pure depolarizers and pure retarders, while $\mathbf{d}$ is nonzero only for dichroic optical elements [99]. Moreover, W reduces to a three-dimensional orthogonal rotation for pure retarders. It should be noticed that if we choose $M_{00} = 1$ (this can be always done since it amounts to a trivial *polarization-independent* renormalization), the Mueller matrix of a non-dichroic optical element ($\mathbf{d} = \mathbf{0}$), is formally identical to a non-unital, trace-preserving, one-qubit quantum map (also called channel) [103]. If also $\mathbf{p} = \mathbf{0}$ (pure depolarizers and pure retarders), then M is identical to a unital, or bistochastic, one-qubit channel [65].

8.2.2 Spectral decompositions

An important theorem in classical polarization optics states that any linear optical element (either deterministic or stochastic) is equivalent to a composite device made of at most four non-depolarizing elements in parallel [46]. This theorem follows from the spectral decomposition of the Hermitean positive semidefinite matrix H [106] associated to $\mathscr{M}$. In this subsection we shortly review such theorem and illustrate its equivalence with the Kraus decomposition theorem of one-qubit quantum maps [65].

Given a Mueller matrix $\mathscr{M}$, it is possible to built a 4×4 Hermitean positive semidefinite matrix $H = H(\mathscr{M})$ by simply *reshuffling* [104] the indices of $\mathscr{M}$

$$H_{ij,kl} \equiv \mathscr{M}_{ik,jl} = \sum_A p_A (T_A)_{ij} (T_A^*)_{kl}, \tag{8.12}$$

where the last equality follows from Eq. (8.10). Equivalently, after introducing the composite indices $\alpha = 2i + j, \beta = 2k + l$, we can rewrite Eq. (8.12) as $H_{\alpha\beta} = \sum_A p_A (T_A)_\alpha (T_A^*)_\beta$. In view of the claimed connection between classical polarization optics and one-qubit quantum mechanics, it is worth noting that H is formally identical to the *dynamical* (or Choi) matrix, describing a one-qubit quantum process [107]. The spectral theorem for Hermitean matrices provides a *canonical* (or spectral) decomposition for H of the form

$$H_{\alpha\beta} = \sum_{\mu=0}^{3} \lambda_\mu (\mathbf{u}_\mu)_\alpha (\mathbf{u}_\mu^*)_\beta, \tag{8.13}$$

where $\lambda_\mu \geq 0$, $(\sum_\mu \lambda_\mu = M_{00})$, are the non-negative eigenvalues of H, and $\{\mathbf{u}_\mu\} = \{\mathbf{u}_0, \mathbf{u}_1, \mathbf{u}_2, \mathbf{u}_3\}$ is the orthonormal basis of eigenvectors of H: $H\mathbf{u}_\mu = \lambda_\mu \mathbf{u}_\mu$. If we rearrange the four components of each eigenvector $\mathbf{u}_\mu$ to form the 2×2 matrices T_μ defined as:

$$T_\mu = \begin{pmatrix} (\mathbf{u}_\mu)_0 & (\mathbf{u}_\mu)_1 \\ (\mathbf{u}_\mu)_2 & (\mathbf{u}_\mu)_3 \end{pmatrix}, \tag{8.14}$$

we can rewrite Eq. (8.13) as $H_{\alpha\beta} = \sum_\mu \lambda_\mu (T_\mu)_\alpha (T_\mu^*)_\beta$. Since Eq. (8.14) can be rewritten as $(T_\mu)_{ij} = (\mathbf{u}_\mu)_{\alpha=2i+j}$, we can go back from Greek to Latin indices and write $H_{ij,kl} = \sum_\mu \lambda_\mu (T_\mu)_{ij}(T_\mu^*)_{kl} = \sum_\mu \lambda_\mu (T_\mu \otimes T_\mu^*)_{ik,jl}$. Finally, from the latter relation and using Eq. (8.12), we obtain

$$\mathscr{M} = \sum_{\mu=0}^{3} \lambda_\mu T_\mu \otimes T_\mu^*. \tag{8.15}$$

Equation (8.15) represents the content of the *decomposition theorem* in classical polarization optics. It implies, via Eq. (8.7), that the most general operation that a linear optical element can perform upon a beam of light can be written as:

$$J_{\text{in}} \rightarrow J_{\text{out}} = \sum_{\mu=0}^{3} \lambda_\mu T_\mu J_{\text{in}} T_\mu^\dagger, \tag{8.16}$$

where the four Jones matrices T_μ represent four different non-depolarizing optical elements.

Since $\lambda_\mu \geq 0$, Eq. (8.16) is formally identical to the Kraus form [65] of a completely positive one-qubit quantum map $\mathscr{E}$. Therefore, if a single photon encoding a polarization qubit (represented by the 2×2 density matrix ρ_{in}), passes through an optical device classically described by the Mueller matrix $\mathscr{M} = \sum_\mu \lambda_\mu T_\mu \otimes T_\mu^*$, its state will be transformed according to

$$\rho_{\text{in}} \rightarrow \rho_{\text{out}} \propto \sum_{\mu=0}^{3} \lambda_\mu T_\mu \rho_{\text{in}} T_\mu^\dagger, \tag{8.17}$$

where the proportionality symbol "$\propto$" accounts for a possible renormalization to ensure $\text{Tr}\rho_{\text{out}} = 1$. Such renormalization is not necessary in the corresponding classical equation (8.16) since $\text{Tr}J_{\text{out}}$ is equal to the total intensity of the output light beam that does not need to be conserved.

By writing Eqs. (8.16, 8.17) we have thus completed the review of the analogies between linear optics and one-qubit quantum maps. In the next section we shall analyze how to use these analogies to engineer maximally entangled mixed-states (MEMS) by acting upon *one* qubit of an entangled pair.

8.3 Engineering maximally entangled mixed-states (MEMS)

Now that we have learned how to associate a quantum map to a set of at most four optical elements, we can apply this knowledge to design a simple optical scheme suitable for MEMS production. Suppose to have two qubits (encoded in the polarization degrees of freedom of two SPDC photons, say *A* and *B*), initially prepared in the state $\rho : \rho = \rho_{ij,kl}|ij\rangle\langle kl| \doteq$

$\rho^R_{ik,jl}|i\rangle\langle k|\otimes|j\rangle\langle l|$. Superscript R indicates *reshuffling* [104] of the indices: $\rho^R_{ik,jl}\equiv\rho_{ij,kl}$. Following Ziman and Bužek [105] we assume that ρ is transformed under the action of the most general *local* (that is, acting upon a single qubit) linear map $\mathcal{E}\otimes\mathcal{I}$ into the state

$$\rho_{\mathcal{E}}=\mathcal{E}\otimes\mathcal{I}[\rho]\propto\sum_{\alpha=0}^{3}\lambda_\alpha T_\alpha\otimes I\,\rho\,T_\alpha^\dagger\otimes I. \tag{8.18}$$

By writing explicitly Eq. (8.18) in the two-qubit basis $\{|ij\rangle\equiv|i\rangle\otimes|j\rangle\}$, it is straightforward to obtain $(\rho_{\mathcal{E}})_{ij,kl}\propto\sum_\alpha\lambda_\alpha\rho^R_{mn,jl}(T_\alpha)_{im}(T_\alpha^*)_{kn}$. Then, from the definition of $\mathcal{M}$ it easily follows that $(\rho_{\mathcal{E}})_{ij,kl}\propto(\mathcal{M}\rho^R)_{ik,jl}$. By reshuffling $\rho_{\mathcal{E}}$, this last result can be written in matrix form as $\rho^R_{\mathcal{E}}\propto\mathcal{M}\rho^R$ which displays the very simple relation existing between the *classical* Mueller matrix $\mathcal{M}$ and the *quantum* state $\rho_{\mathcal{E}}$. Via a direct calculation, it is possible to show that if ρ represents two qubits in the singlet state $\rho_s=\frac{1}{2}(X_0\otimes X_0-X_1\otimes X_1-X_2\otimes X_2-X_3\otimes X_3)$ [102], then the proportionality symbol in the last equation above can be substituted with the equality symbol: $\rho^R_{\mathcal{E}}=\mathcal{M}\rho^R_s$. If the initial state ρ is different from the singlet one, then $\rho_{\mathcal{E}}$ must be simply renormalized by imposing $\mathrm{Tr}(\mathcal{M}\rho^R)=1$.

Now, suppose that we have an experimental setup producing pairs of SPDC photons in the singlet state ρ_s, and we want to transform ρ_s into a given target state $\rho_{\mathcal{T}}$ via a local map $\mathcal{T}\otimes\mathcal{I}:\rho_s\to\rho_{\mathcal{T}}=(\mathcal{M}_{\mathcal{T}}\rho^R_s)^R$. All we have to do is first to invert the latter equation to obtain

$$\mathcal{M}_{\mathcal{T}}=\rho^R_{\mathcal{T}}(\rho^R_s)^{-1}, \tag{8.19}$$

and then to decompose $\mathcal{M}_{\mathcal{T}}$ as $\mathcal{M}_{\mathcal{T}}=\sum_\alpha\lambda_\alpha T_\alpha\otimes T_\alpha^*$. Thus, we get the (at most four) Jones matrices T_α representing the optical elements necessary to implement the desired transformation.

Our technique is very straightforward and we shall demonstrate its feasibility later, by applying it to design an optical setup devoted to MEMS generation. However, at this moment, some caveats are in order. To make $\mathcal{M}_{\mathcal{T}}$ a physically realizable Mueller matrix, its associated matrix $H_{\mathcal{T}}$ should be positive semidefinite. If this is not the case, then the transformation $\rho\to\rho_{\mathcal{T}}$ cannot be implemented via local operations. For example, it is easy to see that if the initial state is a Werner state $\rho_W=p\rho_s+\frac{1-p}{4}I$, $(0\le p\le 1)$ and the target state is the singlet one: $\rho_{\mathcal{T}}=\rho_s$, then such operation (known as *concentration* [108]) cannot be physically implemented by a local setup since $H_{\mathcal{T}}$ has three degenerate negative eigenvalues. Another caveat comes from the no-signalling constraint. Since $\mathcal{M}_{\mathcal{T}}$ describes a local device operating only upon photon A, a second observer should not be able to distinguish the initial state ρ_s from the transformed state $\rho_{\mathcal{T}}$ by measuring only the state of photon B, that is: $\rho^B=\mathrm{Tr}_A(\rho_s)=\mathrm{Tr}_A(\rho_{\mathcal{T}})$. This condition requires the one-qubit map $\mathcal{T}$ to be trace-preserving: $\sum_\alpha\lambda_\alpha T_\alpha^\dagger T_\alpha=I$. From Eq. (8.11), a straightforward calculation shows that such condition cannot be fulfilled if $\mathbf{d}\ne\mathbf{0}$, that is, if the device implementing $\mathcal{T}$ contains dichroic (or PDL) elements. This will be discussed in detail in Chapter 9.

With these caveats in mind, we come to the experimental validation of our method. We choose to generate MEMS I states, represented by the density matrix $\rho_I=p|\phi_+\rangle\langle\phi_+|+(1-p)|01\rangle\langle 01|$, where $|\phi_+\rangle=(|00\rangle+|11\rangle)/\sqrt{2}$ and $(2/3\le p\le 1)$. By varying the parameter p, the entanglement and mixedness of the state ρ_I change. Here, we use the linear entropy S_L [89] and the tangle T, namely, the concurrence squared [88], to quantify the degree of
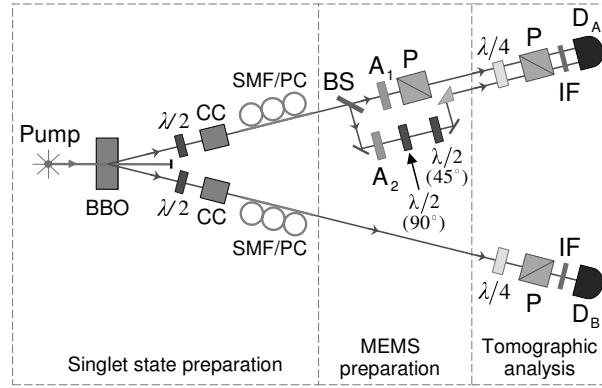
Figure 8.1: *Layout of the experimental setup. The two-path optical device acts only on photon A. Detectors D_A and D_B perform coincidence measurements.*

mixedness and of entanglement, respectively. They are defined as $S_L(\rho) = \frac{4}{3}[1 - \text{Tr}(\rho^2)]$, and $T(\rho) = [\max\{0, \sqrt{\lambda_0} - \sqrt{\lambda_1} - \sqrt{\lambda_2} - \sqrt{\lambda_3}\}]^2$, where $\lambda_0 \geq \lambda_1 \geq \lambda_2 \geq \lambda_3 \geq 0$ are the eigenvalues of $\rho(\sigma_y \otimes \sigma_y)\rho^*(\sigma_y \otimes \sigma_y)$. After applying Eq. (8.19) with $\rho_{\mathscr{T}} = \rho_\text{I}$, a straightforward calculation shows that there are only two non-zero terms in the decomposition of $\mathcal{M}_{\mathscr{T}}$, namely $\{\lambda_0 = 2(1-p),\ \lambda_1 = p\}$, $\{T_0 = \begin{pmatrix} 1 & 0 \\ 0 & 0 \end{pmatrix},\ T_1 = \begin{pmatrix} 0 & -1 \\ 1 & 0 \end{pmatrix}\}$. In physical terms, T_0 is a polarizer and T_1 is a 90° polarization rotator. The two eigenvalues $\{\lambda_0, \lambda_1\}$ give the relative intensity in the two arms of the device and are physically realized by intensity attenuators.

8.4 Experimental implementation

Our experimental set-up is shown in Fig. 8.1. Its first part (Singlet state preparation) comprises a Krypton-ion laser at 413.1 nm that pumps a 1-mm thick $\beta - \text{BaB}_2\text{O}_4$ (BBO) crystal, where polarization-entangled photon pairs at wavelength 826.2 nm are created by SPDC in degenerate type II phase-matching configuration [86]. Single-mode fibers (SMF) are used as spatial filters to assure that each photon of the initial SPDC pair travels in a single transverse mode. Spurious birefringence along the fibers is compensated by suitably oriented polarization controllers (PC) [97]. In addition, total retardation introduced by the fibers and walk-off effects at the BBO crystal are compensated by compensating crystals (CC: 0.5-mm thick BBO crystals) and half-wave plates ($\lambda/2$) in both photonic paths. In this way the initial two-photon state is prepared in the polarization singlet state $|\psi_s\rangle = (|HV\rangle - |VH\rangle)/\sqrt{2}$, where H and V are labels for horizontal and vertical polarizations of the two photons, respectively.

In the second part of the experimental set-up (MEMS preparation) the *two-term* decomposition of $\mathcal{M}_{\mathscr{T}}$ is physically realized by a *two-path* optical device. A photon enters such a device through a 50/50 beam splitter (BS) and can be either transmitted to path 1 or reflected to path 2. The two paths define two independent *spatial* modes of the field. In path 1 a neutral-density filter (A_1) is followed by a linear polarizer (P) oriented horizontally (with respect to the BBO crystal basis). When the photon goes in this path, the initial singlet is

reduced to $|HV\rangle$ with probability proportional to the attenuation ratio a_1 of A_1 ($a = P_{\mathrm{out}}/P_{\mathrm{in}}$). In path 2 a second neutral-density filter (A_2) is followed by two half wave-plates ($\lambda/2$) in cascade relatively oriented at 45°: they work as a 90° polarization rotator. When the photon goes in path 2, the singlet undergoes a local rotation with probability proportional to the attenuation ratio a_2 of A_2.

The third and last part of the experimental set-up (Tomographic analysis), consists of two tomographic analyzers (one per photon), each made of a quarter-wave plate ($\lambda/4$) followed by a linear polarizer (P). Such analyzers permit a tomographically complete reconstruction, via a maximum-likelihood technique [87], of the two-photon state. Additionally, interference filters (IF) in front of each detector ($\Delta\lambda = 5$ nm) provide for bandwidth selection. It should be noticed that detector D_A does not distinguish which path (either 1 or 2) a photon comes from, thus photon *A* is detected in a *mode-insensitive* way: This is the simple mechanism we use to induce decoherence.
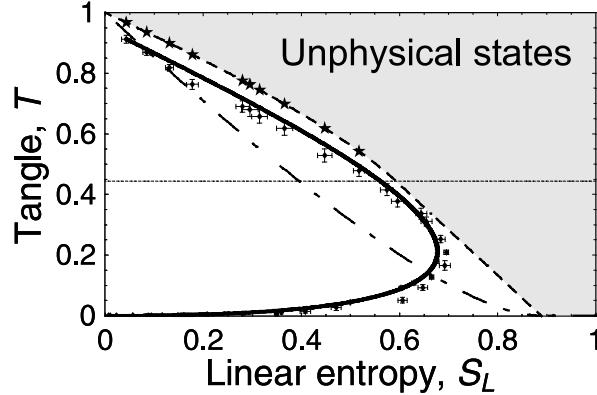
Figure 8.2: *Experimental data and theoretical prediction (continuous line) in the linear entropy-tangle plane. The gray region represents unphysical states and it is bounded from below by MEMS (dashed curve). The lower dotted-dashed curve represents Werner states. The horizontal (dotted) line at T = 4/9 separates MEMS I (above), from MEMS II (below). Stars denote MEMS I states $\rho_\star$ that have the same linear entropy as the measured states ρ_I^{exp} (i.e., the experimental points above the line T = 4/9). The agreement between experiment and theory is manifest.*

8.5 Experimental results

Experimental results are shown in Fig. 8.2 together with theoretical predictions in the linear entropy-tangle plane. The experimentally prepared initial singlet state ρ_s^{exp} has a fidelity [91] $F(\rho_s, \rho_s^{\mathrm{exp}}) = \left| \mathrm{Tr}(\sqrt{\sqrt{\rho_s}\rho_s^{\mathrm{exp}}\sqrt{\rho_s}}) \right|^2 \sim 97\%$ with the theoretical singlet state ρ_s. The continuous curve is calculated from the matrix $\rho_c : \rho_c = \mathscr{M}_\mathscr{F}(p)\rho_s^{\mathrm{exp}}$, and varying p. It represents our theoretical prediction for the given initially prepared state ρ_s^{exp}. If it were possible to achieve exactly $\rho_s^{\mathrm{exp}} = \rho_s$, then such curve would coincide with the MEMS curve

above the horizontal (dotted) line $T = 4/9$. Experimental points with $T \geq 4/9$ (ρ_I^{exp}) are obtained by varying the neutral-density filters $\mathsf{A}_1, \mathsf{A}_2$ in such a way that $a_2 \geq a_1$; while points with $T < 4/9$ are achieved for $a_2 < a_1$. Note that the latter points do not represent MEMSs, but different mixed entangled states whose density matrix is still given by ρ_I but with the parameter p now varying as $0 \leq p \leq 2/3$. The average fidelity between the measured states ρ_I^{exp} an the "target" states $\rho_\star$, is given by $\overline{F(\rho_\star, \rho_I^{\text{exp}})} \sim 80\%$. We believe that the main reason for its deviation from $\lesssim 100\%$, is due to spurious, uncontrolled birefringence and dichroism in the BS and the mirrors composing the set-up. In fact, we calculated the fidelity between the states $\rho_c(p)$ (obtained by applying the theoretically determined map $\mathscr{T} \otimes \mathscr{I}$ to the experimentally prepared initial singlet state ρ_s^{exp}), with the theoretical MEMS $\rho_I(p)$. We have found $F[\rho_I(p), \rho_c(p)] \geq 97\%$ for all $2/3 \leq p \leq 1$; thus the value of $\overline{F} \sim 80\%$ cannot be ascribed to the imperfect initial singlet preparation. However, Fig. 8.2 shows a very good agreement between theoretical predictions and experimental data.

8.6 Summary

In conclusion, in this Chapter we have presented a theoretical study of the analogies between classical linear optics and quantum maps. By using these analogies, we have theoretically proposed and experimentally tested a new, simple method to create MEMS I states of photons (it can be easily generalized to generate MEMS II states, as well). In particular, we have shown that it is possible to create MEMS from an SPDC photon pair, by acting on just a *single* photon of the pair. This task could appear, at first sight, impossible since it was recently demonstrated [105] that even the most general local operation cannot generate MEMS because this would violate relativistic causality. However, our results do not contradict Ref. [105] since we obtained them via postselection operated by coincidence measurements. This shall be will discussed in detail in Chapter 9.

CHAPTER 9

Twin-photon light scattering and causality

In this Chapter [1] we discuss some of our results on multi-mode scattering of entangled photon pairs and we motivate the description of those scattering processes in terms of trace-preserving and non-trace-preserving quantum maps. We then show that non-trace-preserving quantum maps can lead to apparent violations of causality, when the two-photon states are post-selected by coincidence measurements.

9.1   Introduction

Quantum non-locality has played a crucial role in the foundations of quantum mechanics ever since it was theoretically discovered by Einstein, Podolsky, and Rosen (EPR) in 1935 [9]. Bell's findings (1964) that these quantum non-local correlations, also referred to as entanglement, could not be explained in terms of classical local hidden variable models [109] triggered a prolific experimental activity, starting by Aspect *et al.* (1982) [110], who experimentally verified a violation of Bell's inequalities for the first time. These successful experiments have formed, in more recent years, the basis of quantum information science. Within this context it appears to be important to characterize entanglement and its robustness in different kinds of conditions.

In this spirit, we discuss some of our recent experimental results on the effects that different types of scattering processes can have on the degree of polarization-entanglement of twin-photon pairs. First, we briefly present the set-up used in our twin-photon scattering experiments. Second, we discuss some of the constraints imposed by special relativity (i.e., causality condition) on the possibly allowed experiments. Third, we motivate the description of scattering processes as trace-preserving and non-trace-preserving quantum maps [65]. Specifically, we show that non-trace-preserving maps can lead to an apparent violation of causality and that this can be explained in terms of post-selection during the quantum state reconstruction procedure. Finally we draw our conclusions.

9.2   Our experiments

In our experiments we want to analyze the effect that a given multi-mode scattering process can have over the polarization degrees of freedom of entangled photons. The pairs of photons (A-B) are initially created in the polarization singlet state by degenerate type II spontaneous parametric down conversion (SPDC) [86,97], where a pump-photon from a Krypton-ion laser at 413.1 nm is split in two twin-photons of half energy and double wavelength. Then one of the two photons (A) propagates through a local scattering medium (i.e., a scattering medium acting on only one photon). The different scattering media we analyzed range from milk to multi-mode polymer fibers [44]. The polarization density matrix (ρ_{AB}) of the scattered two-photon states are then reconstructed via a standard quantum tomographic procedure [87] (see Fig. 9.1). From this reconstructed density matrix we extract the entanglement content (i.e., the tangle [88]) and the degree of purity (i.e., the linear entropy [89]). The measured data is then displayed in a tangle vs linear entropy plane [84, 85].

In the next sections we will show what are the restrictions on any experiment aiming at quantifying entanglement, and we will discuss whether these restrictions can apparently be violated by using local scattering media and quantum tomographic detection.

9.3   Causality condition

In any kind of Bell-type measurement there are two logical loopholes that have to be closed in order to demonstrate that entanglement is a truly non-local feature of quantum mechanics, which can not be explained in terms of local hidden variable models. These are, the detection
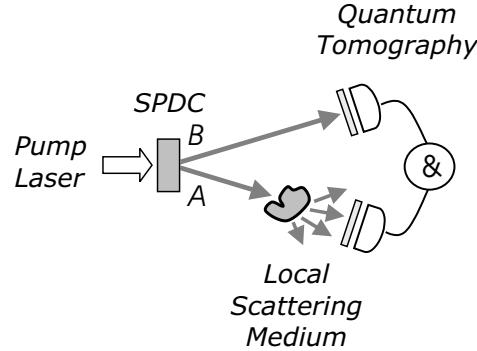
Figure 9.1: *Scheme of our experimental set-up. A high-frequency pump photon is split in two lower-frequency twin-photons (A-B) by SPDC. Photon A undergoes a local scattering process. The polarization density matrix of the scattered photon-pair is then reconstructed via a quantum tomographic procedure.*

loophole and the causality loophole (and it should be noted that they have not been closed at the same time in any experiment up to date). The first loophole refers to the detection efficiency and is grounded on the fact that all experiments so far detect only a small subset of all pairs created [111]. Closure of the second loophole demands that the measurement processes of the two observers A and B (Alice and Bob) are space-like separated events, so that they cannot signal each other [112]. There is thus no way to infer from the result of a local measurement on one wing of the experiment, which measurement has been performed on the other wing. This causality condition is also referred to as 'no-signalling condition'. This idea is schematized in Fig. 9.2. Consider a pair of photons initially created in a polarization correlated state (for instance by SPDC), which propagate in the forwards direction of the space-time diagram. Each of these photons is then detected at time t_D. Each detection event is determined by an independent choice of the polarizer setting (θ_i, $i = A, B$) symbolized by a circle. The choices of the polarizers settings have to be space-like separated enough so that their forward cone of events do not intersect before time t_D, which is the time where each photon is absorbed (a click on a detector). Moreover, each individual detection event has to be registered on both sides independently and compared only after the whole measurement procedure is finished. This does not exclude the existence of correlations between A and B, since they could result from common causes in the overlap region of their backward cone. The overlap regions, where the two cones intersect, corresponds to systems causally related. Note that in Fig. 9.1 the arrow of time stops after the detection happens at time t_D, since the photons are irreversibly absorbed during detection. After the irreversible detection process all that remains is classical information (photon counts). This fact shows dramatically how information is always at the boundary between the quantum and the classical world [113]. Once
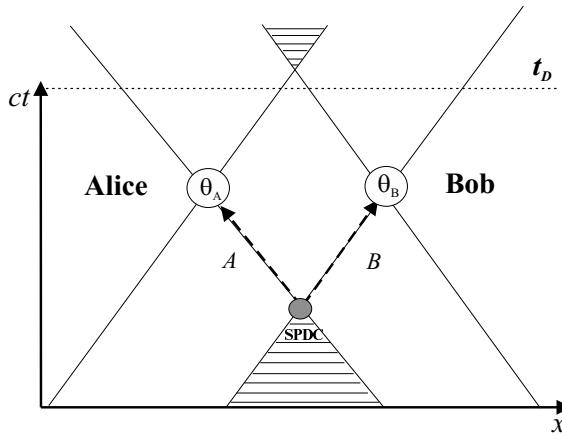
Figure 9.2: *A pair of twin-photons (A-B) produced by SPDC propagates in the forward direction of the space-time diagram. The cone of events for each photon is determined by a choice of each polarizer setting $\theta_{A,B}$. In order to satisfy the no-signalling condition the forward cones of photon A and B should not intersect before the detection time t_D.*

recorded, this classical information can be cleverly manipulated; for instance only a portion of the measured counts can be selected in order to display the desired quantum correlations. Such a selective procedure (named post-selection), involves only classical communication between Alice and Bob and is present in any type of coincidence measurement procedure. In particular it is present in standard quantum state reconstruction tomographic procedures.

9.4 Scattering processes as trace-preserving and non-trace-preserving quantum maps

The mathematical description of a multiple-scattering processes involving a quantum object (such as a photon) is somewhat cumbersome. The appropriate formulation depends among other things on a correct specification of the detection mechanism. In its most pedestrian form the state of a scattered photon can be described as a pure superposition of transverse-spatial modes with different probability amplitudes (which depend on the scatterer). If the detection system could resolve each individual transverse-mode, the state would remain pure, and the whole evolution would be described by a single unitary operator. In a more realistic scenario, the polarization state of the scattered photon is detected in a multi-transverse-mode fashion, so that the spatial mode information is averaged (or traced over) upon detection, and the state of the system is reduced to a statistical mixture represented by a density matrix [13,14]. Thus, we can effectively describe the system as if it were open, where the role of the environment is played by the unobserved internal degrees of freedom (i.e., the transverse-spatial modes of the photons). In this case the evolution of the system cannot be described by a *single* unitary operator. It has to be described in terms of a *set* of unitary operators. This set of unitary

operators is usually referred to as "super-operator"or quantum map [65]. A quantum map is a quantum operation that relates input and output density matrices. As much as the evolution operator for closed systems is considered physical only if it is unitary, a quantum operation $\mathscr{E}$ is a physical map that transforms the input density operators ρ^{in} into the output density operators $\rho^{\text{out}} \equiv \mathscr{E}(\rho^{\text{in}})$ if it satisfies [65]:

- $0 \leq \text{Tr}\{\mathscr{E}(\rho^{\text{in}})\} \leq 1$,

- $\mathscr{E}$ is a convex-linear map such that:

$$\mathscr{E}(\sum_i p_i \rho_i) = \sum_i p_i \mathscr{E}(\rho_i) \qquad (p_i \geq 0),$$

- $\mathscr{E}$ is a completely positive map.

The first condition states that $0 \leq \text{Tr}\{\rho_{\text{out}}\} \leq 1$. When no irreversible processes such as measurements (i.e., projections) or dissipation (i.e., anisotropic losses) are involved the map satisfies the condition $\text{Tr}\{\mathscr{E}(\rho^{\text{in}})\} = 1$, and it is called a trace-preserving map (also referred to as a deterministic map). In the context of polarization optics a particular kind of irreversible process is given by polarization dependent losses. This is in fact the case for dichroic media such as polarizers, which transmit an arbitrary polarization while absorbing the rest. Such type of anisotropic losses must be described by a non-trace-preserving map such that $0 \leq \text{Tr}\{\mathscr{E}(\rho^{\text{in}})\} < 1$. We will next see that these types of maps give rise to interesting questions. The second condition requires the map to be linear and to preserve probabilities, and finally the third one guarantees that ρ^{out} is positive semi-definite, so that it represents a legal density matrix.

9.5 Non-trace-preserving maps and the causality condition

In the context of quantum optics, a common way of proving entanglement between bipartite systems is by measuring the two-photon density matrix ρ_{AB} by means of quantum tomography and then extracting from it a given entanglement measure such as the concurrence or the tangle [88]. One simply infers from the causality condition that if a pair of photons are space-like separated in an initial state ρ_{AB}^{in}, they cannot communicate before detection and thus they cannot affect each other states before detection. This implies that if we act locally on only one of the two photons, say on photon A via a local map $\mathscr{E}_A$, and we measure the state of photon B after the action on photon A took place, we should not see any change in the state of subsystem B. This condition is so important that it strongly restricts the possible outcomes we can measure for the two-photon scattered state ρ_{AB}^{out}. In particular, we have experimentally demonstrated and numerically verified that a two-photon scattered state generated by a local scattering process, in the experimental configuration shown in Fig. 9.1, can only have a very particular shape; namely, it can only belong to a generalized class of Werner states [114] (see Chapter 7). This statement is quite, but not completely, general. In fact, it is only true when the scattering system applied on A has no selective losses, in other words when the action upon subsystem A can be described in terms of a trace-preserving map. On the other hand,

we have found that when selective losses are allowed, as in the case of dichroic scattering media, a class of sub-Werner states is obtained for the two-photon scattered state ρ_{AB}^{out} [114] (see Chapter 7).

What happens then when the scattering system involves selective absorption? So far, we know that this type of scattering media cannot be described by a trace-preserving map. But what is the consequence of that? As we will see, by analyzing two practical examples, non-trace-preserving maps can lead to apparent violations of causality. Consider as a first example the case of a polarization singlet input state $\rho_{AB}^{\text{in}} = |\psi^-\rangle\langle\psi^-|$ where $|\psi^-\rangle = (|HV\rangle - |VH\rangle)/\sqrt{2}$. This state contains maximal information about the bipartite correlations, but minimal information about the state of each subsystem. So, if we measure the reduced input state of B ($\rho_B^{\text{in}} = \text{Tr}_A\{\rho_{AB}^{\text{in}}\}$) or the reduced input state of A ($\rho_A^{\text{in}} = \text{Tr}_B\{\rho_{AB}^{\text{in}}\}$) we obtain in both cases a maximally mixed state (proportional to the 2×2 identity)

$$\rho_A^{\text{in}} = \rho_B^{\text{in}} = \begin{pmatrix} 1/2 & 0 \\ 0 & 1/2 \end{pmatrix}. \tag{9.1}$$

Let's imagine now that we place a polarizer (we assume for simplicity that it is oriented in the H direction) in the path of photon A, this is a typical dichroic system acting locally on subsystem A. If we then measure the bi-photon output state in a coincidence-count circuit, we will obtain $\rho_{AB}^{\text{out}} = |H\rangle\langle H|_A \otimes |V\rangle\langle V|_B$, which is a separable pure state. If we now trace over photon A, we obtain that the output state of B is also fully polarized in the V direction $\text{Tr}_A\{\rho_{AB}^{\text{out}}\} = \rho_B^{\text{out}} = |V\rangle\langle V|$; clearly, the output state of B obtained in this way is not equivalent to ρ_B^{in}, so we could claim that photon B was affected by only acting on A, thus violating causality. The reason why the state of B has apparently changed, without acting on it, is because there has been classical communication between Alice and Bob (of course the communication was *after* detection so there is no violation of causality). Such is the case in a coincidence-count type of measurement. The state of B has changed only after the tomographic procedure, which only involves local operations and classical communication.

Besides, on a more sophisticated level, non-trace-preserving maps have proved to be useful for maximally-entangled-mixed state (MEMS) engineering [100], in apparent contradiction with Ref [105]. Note that MEMS are of interest for realistic quantum information applications [84,85]. Consider the local map proposed in Ref. [100] to create maximally entangled mixed states type I (MEMS I, see Chapter 8). MEMS I can be written as:

$$\rho_{\text{MEMSI}}(p) = \begin{pmatrix} p/2 & 0 & 0 & p/2 \\ 0 & 1-p & 0 & 0 \\ 0 & 0 & 0 & 0 \\ p/2 & 0 & 0 & p/2 \end{pmatrix}, \qquad 2/3 \le p \le 1. \tag{9.2}$$

The quantum map that generates MEMS I can be implemented by using a medium with anisotropic losses (i.e., a dichroic medium). This medium should act locally on one photon of an entangled pair, initially prepared in the polarization singlet state. Subsequently, after propagation along the dichroic medium, the twin-photon state should be reconstructed via quantum tomography. In this way, it can be shown that $\rho_{AB}^{\text{out}} = \rho_{\text{MEMSI}}$ [100].

A medium with anisotropic losses naturally performs a kind of post-selective measurement, since it selectively transmits (or absorbs) a portion of the total number of photons that

passes through it [66]. These selective losses introduce a non-trivial renormalization to the measured bipartite output density matrix ρ_{AB}^{out}. This is in contrast to the trivial renormalization required for isotropic losses, given for instance by isotropic scattering, where only the total intensity diminishes (in terms of maps, isotropic or random scattering can be described by a trace-preserving map up to an overall renormalization constant). If we now want to obtain the state of photon B (after propagation of photon A through the dichroic medium) by tracing over the state of photon A, in Eq. (9.2), we will find:

$$\rho_B^{\text{out}} = \text{Tr}_A\{\rho_{AB}^{\text{out}}\} = \begin{pmatrix} p/2 & 0 \\ 0 & 1 - p/2 \end{pmatrix}. \tag{9.3}$$

By comparing Eq. (9.3) with Eq. (9.1), we see that $\rho_B^{\text{in}} \neq \rho_B^{\text{out}}$. We have apparently modified the state of B by acting only on A, which seems to violate causality. Once again the explanation is in the way in which we reconstructed the scattered state. The reconstructed density matrix of the bipartite output state ρ_{AB}^{out} will correctly describe the result of any other experiment involving coincidence measurements (as, e.g., Bell measurements), but it will *fail* when describing the result of any single-photon measurement, as it was obtained by local operations and post-selection of the coincidence counts via classical communication. Note that any classical communication between distant observers can be considered as a kind of long range interaction [113]; in this way it is apparently possible to affect the state of B at a distance. But this does *not* violate the no-signalling condition, since the communication or the 'interaction' occurs after detection, by post-selection of the counts.

9.6 Summary

In conclusion, in this Chapter we have shown that scattering processes involving twin photons can be described by quantum maps. In the case of non-trace-preserving maps, as it is the case for scattering systems with polarization dependent losses, the tomographically reconstructed bi-photon density matrices can lead to an apparent violation of the no-signalling condition. This apparent surprise can be overcome when one includes post-selective detection, which is a procedure that involves classical communication between distant observers.
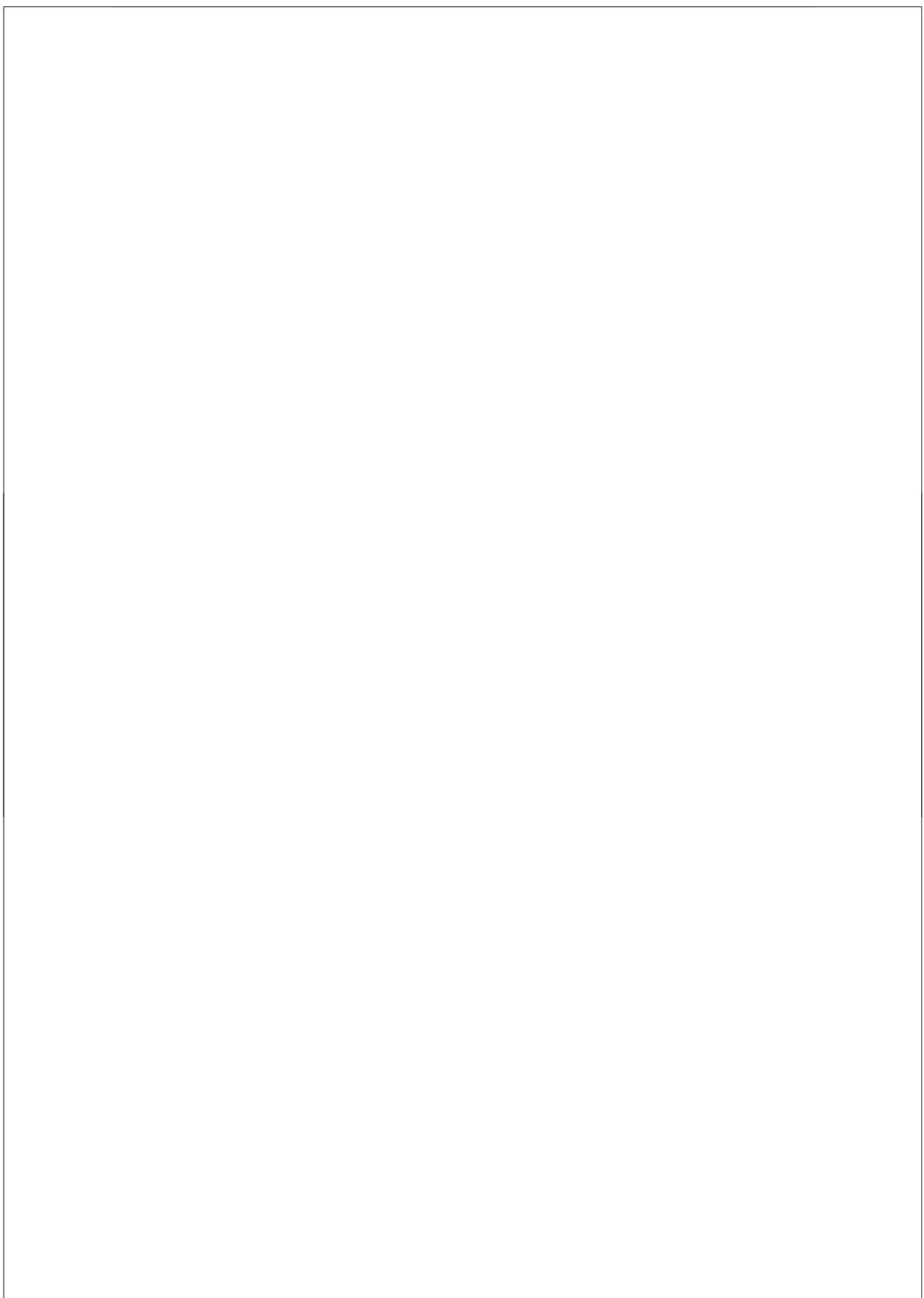
Bibliography

[1] Lord Rayleigh, 'On the light form the sky, its polarization and colour', Philos. Mag. **47**, 375 (1899); Proc. Roy. Soc. London, Ser. A **79**, 399 (1907).

[2] H.C. van de Hulst, *Light scattering by small particles* (John Wiley, N. Y., 1957).

[3] M. C. W. van Rossum, T. M. Nieuwenhuizen, *Multiple scattering of classical waves: microscopy, mesoscopy, and difussion*, Rev. Mod. Phys. **71**, 313 (1999).

[4] D. S. Kliger, J. W. Lewis, and C. E. Randall, *Polarized light in optics and spectroscopy* (Academic Press, Inc., 1990).

[5] A. E. Siegman, *Lasers* (University Science Books, Mill Valley, CA, 1996).

[6] M. Born and E. Wolf, *'Principles of Optics'* (Pergamon Press, 1984), 6th edition.

[7] C. H. Henry and R. F. Kazarinov, 'Quantum noise in photonics', Rev. Mod. Phys. **68**, 801 (1996).

[8] P. Lodahl, A. P. Mosk, and A. Lagendijk, 'Spatial Quantum Correlations in Multiple Scattered Light', Phys. Rev. Lett. **95**, 173901 (2005).

[9] A. Einstein, B. Podolsky, and N. Rosen, 'Can quantum-mechanical description of physical reality be considered complete?', Phys. Rev. Lett. **47**, 777 (1935).

[10] R. Ursin, R. Tiefenbacher, T. Schmitt-Maderbach, H. Weier, T. Scheidl, M. Lindenthal, B. Blauensteiner, T. Jennewein, J. Perdigues, P. Trojek, B. Ömer, M. Fürst, M. Meyenburg, J. Rarity, Z. Sodnik, C. Barbieri, H. Weinfurter, and A. Zeilinger, 'Free-space distribution of entanglement and single photons over 144 km', Phys. Rev. Lett. **98**, 010504 (2007).

[11] M. Aspelmeyer, H. R. Böhm, T. Gyatso, T. Jennewein, R. Kaltenbaek, M. Lindenthal, G. Molina-Terriza, A. Poppe, K. Resch, M. Taraba, R. Ursin, P. Walther, and A. Zeilinger, 'Long distance free-space distribution of quantum entanglement', Science **301**, 621 (2003).

[12] E. Altewischer, M. P. van Exter, and P. J. Woerdman, 'Plasmon-assisted transmission of entangled photons', Nature **418**, 304 (2002).

[13] A. Aiello and J. P. Woerdman, 'Intrinsic entanglement degradation by multimode detection', Phys. Rev. A **70**, 023808 (2004).

[14] J. L. van Velsen and C. W. J. Beenakker, 'Transition from pure to mixed-state entanglement by random scattering', Phys. Rev. A **70**, 032325 (2004).

[15] A. Aiello, G. Puentes, and J. P. Woerdman, 'Linear optics and quantum maps', quant-ph/0611179, submitted to Phys. Rev. A (2006).

[16] G. Puentes, A. Aiello and J. P. Woerdman, 'Ray splitting in paraxial optical cavities', Phys. Rev. E **69**, 036209 (2004).

[17] A. Kohler, G. H. Killesreiter, and R. Blümel, 'Ray splitting in a class of chaotic triangular step billiards', Phys. Rev. E **56**, 2691 (1997).

[18] L. Couchman, E. Ott, and T. M. Antonsen, 'Quantum chaos in systems with ray splitting', Phys. Rev. A **46**, 6193 (1992).

[19] J.U. Nöckel and R.K. Chang, 'Experimental Methods in the Physical Sciences', from *2D-Microcavities: Theory and Experiments* (Academic Press, San Diego, 2002).

[20] J.H. Jensen, 'Chaotic scattering of light by a dielectric cylinder', J. Opt. Soc. Am A **10**, 1204 (1993).

[21] M. Hentschel and K. Richter, 'Quantum chaos in optical systems: The annular billiard', Phys. Rev. E **66**, 056207 (2002).

[22] P. Cvitanović, *Classical and Quantum Chaos* (www.nbi.bk/ChaosBook/, 2002).

[23] E. Ott, *Chaos in Dynamical Systems* (Cambridge University Press, 2002), 2nd edition.

[24] S. Bleher, C. Grebogi, E. Ott, and R. Brown, 'Fractal boundaries for exit in Hamiltonian dynamics', Phys. Rev. A **38**, 930 (1988).

[25] S. Ree and L. E. Reichl, 'Fractal analysis of chaotic classical scattering in a cut-circle billiard with two openings', Phys. Rev. E **65**, 055205(R) (2002).

[26] D. Sweet, E. Ott and J. A. Yorke, 'Topology in chaotic scattering', Nature **399**, 315 (1999).

[27] P. Gaspard, 'Chaos, *Scattering and Statistical Mechanics* (Cambridge University Press, 1998), 1st edition.

[28] S. Bleher and C. Grebogi and E. Ott, 'Bifurcation to chaotic scattering', Physica D **46**, 87 (1990).

[29] A. Aiello, M.P. van Exter, and J. P. Woerdman, 'Ray chaos in optical cavities based upon standard laser mirrors', Phys. Rev. E **68**, 046208 (2003).

[30] S. Longhi, 'Stability of periodic paraxial optical systems', Phys. Rev. E **65**, 027601 (2002).

[31] J. Schneider, T. Tél, and Z. Neufeld, 'Dynamics of leaking Hamiltonian systems', Phys. Rev. E **66**, 066218 (2002).

[32] J. Aguirre and M. A. F. Sanjuán, 'Limit of small exits in open Hamiltonian systems', Phys. Rev. E **67**, 056201 (2003).

[33] G. Benettin and J. M. Strelcyn, 'Numerical experiments on the free motion of a point mass moving in a plane convex region: Stochastic transition and entropy', Phys. Rev. A **17**, 773 (1978).

[34] H. Fustenberg, 'Noncommuting random products', Trans. Amer. Math. Soc. **108**, 377 (1963).

[35] A. Crisanti, G. Paladin and A. Vulpani, *Products of Random Matrices* (Springer-Verlag, 1993).

[36] P. Gaspard and G. Nicolis, 'Transport properties, Lyapunov exponents, and entropy per unit time', Phys. Rev. Lett. **65**, 1693 (1990).

[37] G. Puentes, A. Aiello and J. P. Woerdman, 'Chaotic ray dynamics in an optical cavity with a beam splitter', Opt. Lett. **29**, 929 (2004).

[38] R. E. Prange, E. Ott, T. M. Antonsen, Jr., B. Georgeot and R. Blümel, 'Smoothed density of states for problems with ray splitting', Phys. Rev. E **53**, 207 (1996).

[39] R. Blümel, T. M. Antonsen, Jr., B. Georgeot, E. Ott and R. E. Prange, 'Ray splitting and quantum chaos', Phys. Rev. Lett. **76**, 2476 (1996).

[40] A. Kohler, G. H. M. Killesreiter and R. Blümel,'Ray splitting in a class of chaotic triangular step billiards', Phys. Rev. E **56**, 2691 (1997).

[41] A. Kohler and R. Blümel, 'Annular ray-splitting billiard', Phys. Lett. A **238**, 271 (1998).

[42] J. Aguirre and M. A. F. Sanjuán, 'Limit of small exits in open Hamiltonian systems', Phys. Lett. E **67**, 056201 (2003).

[43] C. Jung, C. Mejia-Monasterio and T. H. Seligman, 'Scattering one step from chaos', Phys. Lett. A **198**, 306 (1995).

[44] G. Puentes, D. Voigt, A. Aiello, and J. P. Woerdman, 'Experimental observation of universality in depolarized light scattering', Opt. Lett. **30**, 3216 (2005).

[45] L. Mandel and E. Wolf, *Optical coherence and quantum optics* (Cambridge University Press, 1995), 1st edition.

[46] D. G. M. Anderson, and R. Barakat,'Necessary and sufficient conditions for a Mueller matrix to be derivable from a Jones matrix', J. Opt. Soc. Am. A **11**, 2305 (1994).

[47] S. R. Cloude, E. Pottier, 'Concept of polarization entropy in optical scattering', Optical Engineering, **34**, 1599 (1995).

[48] F. Le Roy-Brehonnet and B. Le Jeune, 'Utilization of Mueller matrix formalism to obtain optical targets depolarizatino and polarization and polarization properties', Prog. Quant. Electr. **21**, 109 (1997).

[49] J. J. Gil and E. Bernabeu, 'Depolarization and polarization indices of an optical system ', Optica Acta **33**, 185 (1986).

[50] A. Aiello and J. P. Woerdman, 'Physical bounds to the entropy-depolarization relation in random light scattering', Phys. Rev. Lett. **94**, 090406 (2005).

[51] M Legré, M. Wegmüller and N. Gisin, 'Quantum measurement of the degree of polarization of a light beam', Phys. Rev. Lett. **91**, 167902 (2003).

[52] E. Wolf,'Unified theory of coherence and polarization of random electromagnetic beams', Phys. Lett. A **312**, 263 (2003).

[53] V. B. Berestetskiĭ, E. M. Lifshitz, and L. P. Pitaevskiĭ, *Relativistic quantum theory* (Pergamon Press, Oxford, 1971), 1st Edition.

[54] A. Peres, *Quantum theory: concepts and methods* (Kluwer Academic Publihser, 1998).

[55] T. C. Wei, K. Nemoto, P. M. Goldbart, P. G. Kwiat, W. J. Munro, and F. Verstraete, 'Maximal entanglement versus entropy for mixed quantum states', Phys. Rev. A **67**, 022110 (2003).

[56] K. Życzkowski, 'Renyi extrapolation of Shannon entropy', Open Syst. Inf. Dyn. **10**, 297 (2003).

[57] Chi-Huang Lin, A. Ying-Guey Fuh, Tin-Shan Mo, and Chi-Yen Huang,'Scattering light interference from liquid crystal polymer dispersion films', Jpn. J. Appl. Phys. **41**, 7441 (2002).

[58] T. Okamoto and T. Asakura, 'Multiple light scattering from a moving layer of Brownian particles: comparison with a rigid phase screen', Waves in Random Media **3**, 211 (1993).

[59] C. Emslie, 'Review of polymer optical fibers', J. Mat. Sci. **23**, 2281 (1988).

[60] C. Koeppen, R. F. Shi, W. D. Chen, and A. F. Garito, 'Properties of plastic optical fibers', J. Opt. Soc. Am. B **15**, 727 (1998).

[61] K. Kim, L. Mandel, and E.Wolf, 'Relationship between Jones and Mueller matrices for random media', J. Opt. Soc. Am. A **4**, 433 (1987).

[62] J. J. Gil, 'Characteristic properties of Mueller matrices', J. Opt. Soc. Am. A **17**, 328 (2000).

[63] P. Lodahl and A. Lagendijk, 'Transport of quantum noise through random media', Phys. Rev. Lett. **94**, 153905 (2005).

[64] A. Aiello, G. Puentes, D. Voigt, and J. P. Woerdman, 'Maximum-likelihood estimation of Mueller matrices', Opt. Lett. **31**, 817 (2006).

[65] M. A. Nielsen and I. L. Chuang, *Quantum computation and quantum information*, (Cambridge University Press, Cambridge, 2000).

[66] N. Brunner, A. Acín, D. Collins, N. Gisin, and V. Scarani, 'Optical telecom networks as weak quantum measurements with postselection', Phys. Rev. Lett. **91**, 180402 (2003).

[67] J. B. Altepeter, D. Branning, E. Jeffrey, T. C. Wei, P. G. Kwiat, R. T. Thew, J. L. O'Brien, M. A. Nielsen, and A. G. White, 'Ancilla-assisted quantum process tomography', Phys. Rev. Lett. **90**, 193601 (2003).

[68] M. F. Sacchi, 'Extremal equation for optimal completely positive maps', Phys. Rev. A **63**, 054104 (2001).

[69] D. L. Falkoff and J. E. McDonald, J. Opt. Soc. Am. **41**, 'On the Stokes parameters for polarized radiation', 861 (1951).

[70] U. Fano, 'A Stokes-parameter technique for the treatment of polarization in quantum mechanics', Phys. Rev. **93**, 121 (1954).

[71] A. Aiello, and J. P. Woerdman, 'Linear Algebra for Mueller Calculus', math-ph/0412061 (2004).

[72] C. H. Bennet, 'Teleporting an unknown quantum state via dual classical and Einstein-Podolsky-Rosen channels', Phys. Rev. Lett. **70**, 1895 (1992).

[73] A. K. Ekert, 'Quantum cryptography based on Bells theorem', Phys. Rev. Lett. **67**, 661 (1991).

[74] D. Bouwmeester, A. Ekert, and A. Zeilinger, *The physics of quantum information* (Springer, 2000).

[75] W. A. T. Nogueira, S. P. Walborn, S. Pádua, and C. H. Monken, 'Generation of a Two-Photon Singlet Beam', Phys. Rev. Lett. **92**, 043602 (2004).

[76] M. D'Angelo, Y. H. Kim, S. P. Kulik, and Y. Shih, 'Identifying Entanglement Using Quantum Ghost Interference and Imaging', Phys. Rev. Lett. **92**, 233601 (2004).

[77] A. Peres, 'Separability Criterion for Density Matrices', Phys. Rev. Lett. **77**, 1413 (1996).

[78] M. Horodecki, P. Horodecki, and R. Horodecki, 'Mixed-State Entanglement and Distillation: Is there a Bound Entanglement in Nature?', Phys. Rev. Lett. **80**, 5239 (1998).

[79] R. F. Werner, 'Quantum states with Einstein-Podolsky-Rosen correlations admitting a hidden-variable model', Phys. Rev. A **40**, 4277 (1989).

[80] W. J. Munro, D. F. V. James, A. G. White, and P. G. Kwiat, 'Maximizing the entanglement of two mixed qubits', Phys. Rev. A **64**, 030302(R) (2001).

[81] P. G. Kwiat, S. Barraza-Lopez, A. Stefanov, and N. Gisin, 'Experimental entanglement distillation and 'hidden' non-locality', Nature **409**, 1014 (2001).

[82] A. G. White, D. F. V. James, W. J. Munro, and P. G. Kwiat, 'Linear optical controlled-NOT gate in the coincidence basis', Phys. Rev. A **65**, 012301 (2001) [5 pages].

[83] Y. S. Zhang, Y. F. Huang, C. F. Li, and G. C. Guo, 'Experimental preparation of the Werner state via spontaneous parametric down-conversion', Phys. Rev. A **66**, 062315 (2002).

[84] N. A. Peters, J. B. Altepeter, D. Branning, E. R. Jeffrey, T.-C. Wei, and P. G. Kwiat, 'Maximally Entangled Mixed States: Creation and concentration', Phys. Rev. Lett. **92**, 133601 (2004).

[85] M. Barbieri, F. De Martini, G. Di Nepi, and P. Mataloni, 'Generation and characterization of Werner states and maximally entangled mixed states by a universal source of entanglement', Phys. Rev. Lett. **92**, 177901 (2004).

[86] P.G. Kwiat, K. Mattle, H. Weinfurter, A. Zeilinger, A.V. Sergienko, and Y. Shih, 'New high-intensity source of polarization-entangled photon pairs', Phys. Rev. Lett. **75**, 4337 (1995).

[87] D. F. V. James, P. G. Kwiat, W. J. Munro, and A. G. White, 'Measurement of qubits', Phys. Rev. A **64**, 052312 (2001).

[88] W. K. Wootters, 'Entanglement of formation of an arbitrary state of two qubits', Phys. Rev. Lett. **80**, 2245 (1998).

[89] S. Bose, and V. Vedral, 'Mixedness and teleportation', Phys. Rev. A **61**, 040101(R) (2000).

[90] P. S. K. Lee, J. B. Pors, M. P. van Exter, and J. P. Woerdman, 'Simple method for accurate characterization of birefringent crystals', Appl. Opt. **44**, 866 (2005).

[91] R. Jozsa, 'Fidelity for mixed quantum states', J. Mod. Opt. **41**, 2315 (1994).

[92] M. C. W. van Rossum and Th. M. Nieuwenhuizen, 'Multiple scattering of classical waves: microscopy, mesoscopy, and diffusion ', Rev. Mod. Phys. **71**, 313 (1999).

[93] M. P. Van Albada, and A. Lagendijk, 'Observation of weak localization of light in a random medium ', Phys. Rev. Lett. **55**, 2692 (1985).

[94] A. A Chabanov, M. Stoytchev, and A. Z. Genack, 'Statistical signatures of photon localization', Nature (London) **404**, 850 (2000).

[95] G. L. J. A. Rikken and B. A. van Tiggelen, 'Observation of magnetically induced transverse diffusion of light', Nature (London) **381**, 54 (1996).

[96] F. Scheffold and G. Maret, 'Universal conductance fluctuations of light', Phys. Rev. Lett. **81**, 5800 (1998).

[97] G. Puentes, D. Voigt, A. Aiello, and J. P. Woerdman,'Tunable spatial decoherers for polarization entangled photons', Opt. Lett. **31**, 2057 (2006).

[98] M. B. van der Mark, 'Propagation of light in disordered media', PhD Thesis, Univ. Amsterdam (1990).

[99] S. Y. Lu and R. A. Chipman, 'Interpretation of Mueller matrices based on polar decomposition', J. Opt. Soc. Am. A **13**, 1 (1996).

[100] A. Aiello, G. Puentes, D. Voigt, and J. P. Woerdman, 'Maximally entangled mixed-state generation via local operations', quanth-ph/0603182, submitted to Phys. Rev. A (2006).

[101] J. N. Damask, *Polarization Optics in Telecommunications* (Springer, 2005).

[102] J. J. Sakurai, *Modern Quantum Mechanics* (Addison Wesley, 1994).

[103] M. B.Ruskai, S. Szarek, and E. Werner, 'An analysis of completely positive trace preserving maps on 2×2 matrices', Linear Algebr. Appl. **347**, 159 (2002).

[104] K. Zyczkowski, and I. Bengtsson, *Qeometry of quanutm states: An introduction to quantum entanglement* (Cambridge University Press, 2006).

[105] M. Ziman, and V.Bužek, 'Concurrence versus purity: Influence of local channels on Bell states of two qubits', Phys. Rev. A **72**, 052325 (2005).

[106] R. Simon, 'The connection between Mueller and Jones matrices of polarization optics ', Optics Comm. **42**, 293 (1982).

[107] M.-D. Choi, 'Completely positive maps on complex matrices', Linear Algebra Appl. **10**, 285 (1975).

[108] R. T. Thew, and W. J. Munro, 'Entanglement manipulation and concentration', Phys. Rev. A **63**, 030302(R) (2001).

[109] J. S. Bell, 'On the EinsteinPodolskyRosen paradox', Physics (Long Island City, N.Y.) **1**, 195 (1965).

[110] A. Aspect, J. Dalibard and G. Roger, 'Experimental test of Bell's inequalities using time-varying analyzers ', Phys. Rev. Lett. **49**, 1804 (1982).

[111] P. Pearle, 'Hidden-variable example based upon data rejection ', Phys. Rev. D **2**, 1418 (1970).

[112] G. Weihs, T. Jennewein, C. Simon, H. Weinfurter and A. Zeilinger, 'Violation of Bell's inequality under strict Einstein locality conditions', Phys. Rev. Lett. **81**, 5039 (1998).

[113] A. Peres and D. R. Terno, 'Quantum information and reltivity theory', Rev. Mod. Phys. **76**, 93 (2004).

[114] G. Puentes, A. Aiello, D. Voigt and J. P. Woerdman, 'Entangled mixed-state generation by twin-photon scattering', Phys. Rev. A **75**, 032319 (2007).

Summary

In this summary the reader will find a brief introduction to the central subject in the Thesis, namely, light scattering with entangled photons. The intention of this summary is to make the topic of the Thesis as accessible to the inexpert reader as possible, so, as a general rule, priority is given to simplicity.

Summary

Light scattering with entangled photons: an heuristic approach

When a beam of light propagates in an homogenous material it follows a straight trajectory. If during its propagation light encounters an inhomogeneity it can be scattered. The main effect of a scattering event is to change the direction of propagation (or momentum k) of the light beam (see Fig. 1). An inhomogeneity or scatterer can be an atom or a molecule, a particle with different refractive index (with respect to the background homogeneous medium) or a density fluctuation in a liquid or gas. Such a transformation in the momentum of light by scattering is always accompanied by a transformation in the polarization of light, since polarization is a transverse degrees of freedom. That is, transverse to the momentum k (as indicated by the small transverse arrow in Fig. 1). When a scattering process involves many
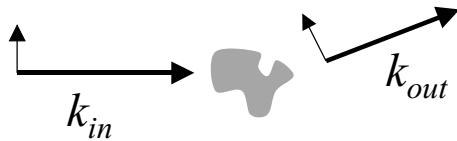
Figure 1: *The main effect of a scattering event is to change the direction of propagation of light. The polarization direction is indicated by the small transverse arrow.*

directions of propagation k, the so called multi-mode scattering, there is not a single well defined transverse plane which characterizes the polarization of the scattered light. When such is the case the polarization and the momentum of light are said to be coupled, so this is an example of how a scattering process can affect the polarization degrees of freedom of light.

Another typical example of the connection between scattering processes and polarization is Rayleigh scattering of sunlight by small particles at the atmosphere (see Fig. 2). Rayleigh scattering is not only the reason why the sky looks blue, but it is also the reason why it is partially polarized. Most of us have experienced the polarized nature of the sky when we use polaroid sunglasses and we partially block the scattered sunlight. Polarization of skylight is also used for navigation by insects, such as bees, and there are claims that Vikings already had a navigation system based on the polarization of light, more that 1000 years ago!

So, it is clear that scattering processes do have an effect on polarization degrees of freedom of light. Now we could ask ourselves what would happen if we performed a light scattering experiment when the quantum nature of light is essential. A prominent example of 'quantum light' are entangled photon pairs. So we could ask ourselves the question of what would happen if we performed a scattering experiment with polarization-entangled photons?.
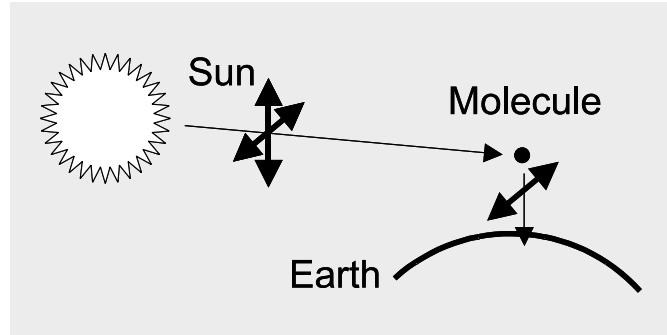
Figure 2: *Rayleigh scattering by molecules at the atmosphere.*

That is indeed the question that we want to answer in this Thesis.

In order to answer this question, lets first see how can we create polarization-entangled photon pairs. These photon pairs, also called twin-photons, can be created in the laboratory by the process of spontaneous parametric down-conversion. This is a non-linear process which happens in a special kind of crystal, called BBO (as an abbreviation to Beta Barium Borate), in which a pump photon is split into two twin photons of half of the energy (see Fig. 3 (a)). These two photons (labelled 1 and 2) are completely correlated. Actually, because of
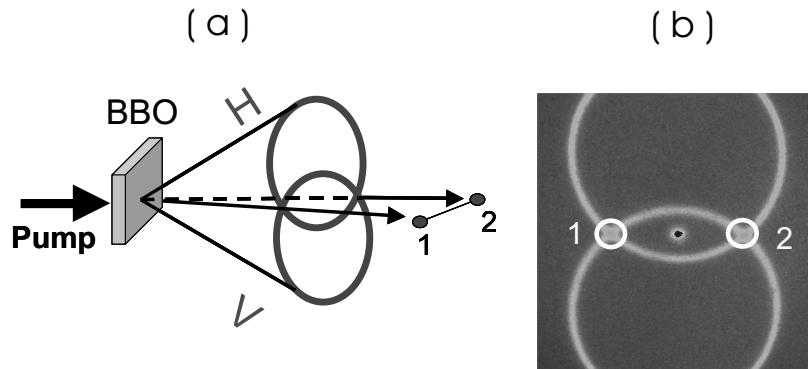
Figure 3: *(a) Scheme of twin-photons created by spontaneous parametric down-conversion. (b) Far-field intensity pattern of down-converted photons. The polarization-entangled photon pairs are selected from the crossings of the two rings.*

the way in which they are created (at the crystal) they are completely anti-correlated, so they should rather be called 'anti-twin photons'! The anti-correlation is such that when one of the two photons is polarized in the direction P_1, the other photon in the pair must be polarized in the direction $P_2 \perp P_1$, and this is true for any value of P_1, which is the intrinsically non-

89

classical feature of this correlation. This quantum correlation in the polarization degrees of freedom of photons is called polarization-entanglement. It is important to note that this quantum correlation exist for any separation between the photons, which is the so called non-local character of entanglement. The photon pairs created by down-conversion are emitted in two intersecting cones which are orthogonally polarized (for instance, one cone is vertically polarized V and the other cone is horizontally polarized H). These cones, when projected on a fixed plane, look like two intersecting rings. The polarization-entangled photon pairs are selected from the crossings if these two rings (see Fig. 3 (b)). So that individual photons coming from the ring-crossings do not have a fix polarization (half of them are V and the other half are H), but photon pairs coming at the same time from the two crossings must have relative orthogonal polarization.
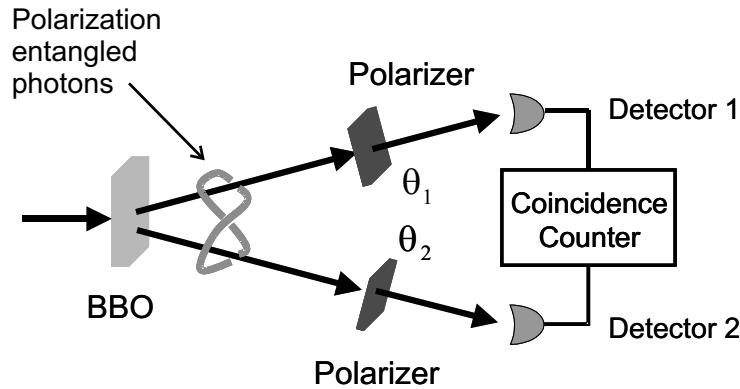
Figure 4: *Scheme for the detection of polarization entanglement of twin-photons.*

How can we detect this non-local anti-correlation between the polarization-entangled photon pairs? A way of doing this is by placing a linear polarizer in the path of each one of the two photons belonging to the pair. In such a way that polarizer P_1 is oriented at θ_1 and polarizer P_2 is oriented at θ_2. The idea is to then detect the photons transmitted by each polarizer in a coincidence count circuit (see Fig. 4). A coincidence count is registered whenever the two independent detectors (labelled 1 and 2) detect an incoming photon at the same time (in reality it is never exactly at the same time but within a very very small, 2 or 3 nanoseconds, coincidence-time interval). So, taking into account that the relative polarization of the two photons is anti-parallel, we should expect to see many coincidences when $\theta_2 \perp \theta_1$ and almost no coincidences when $\theta_2 \parallel \theta_1$, and this should be the case for any orientation of P_2 (or P_1). That is indeed what one sees in the laboratory, and what is shown in Fig. 5. The different experimental curves (called visibility curves) correspond to fixing polarizer P_2 at $\theta_2 = 0°$ (squares) and at $\theta_2 = 45°$ (circles), while rotating P_1. Such strong modulation in the coincidence counts is a signature of the polarization entanglement between the two-photons.

So, we already know that scattering process affect polarization degrees of freedom of light, we also know how to create polarization-entangled photons and we even know how to detect this entanglement. So we are ready to answer the question 'what happens when
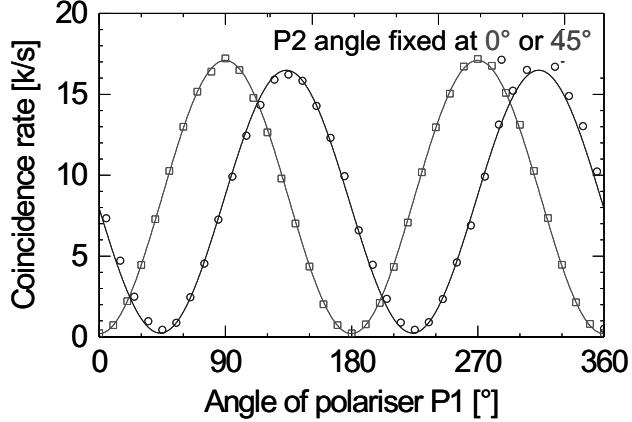
Figure 5: *Coincidence counts measurements fixing polarizer P_2 at $\theta_2 = 0°$ (squares) and at $\theta_2 = 45°$ (circles).*

we perform a scattering experiment with polarization-entangled photons'. Let's imagine that we create a pair polarization-entangled photons by parametric down-conversion. The two entangled photons (labelled 1 and 2) are created in such a way that they propagate with well defined momenta k_1 and k_2. Then we can place a scattering medium in the path of photon 1 (we could also place a scattering medium in the path of photon 2 but, conceptually, this would not add anything new to the problem). As the photon propagates in the medium it undergoes multiple scattering events. Each scattering event transforms the direction of propagation, in such a way that the momentum of the outgoing scattered photon is in a superposition of many momenta k_{out}, each one with a different polarization plane attached to it (see Fig. 6). So the scattering process couples the polarization and the momentum degrees of freedom of the incoming photon. If we then detect the scattered photon pairs in coincidence counts but with a momentum insensitive detector, this can be done by using detectors with a large detecting surface, then all the spatial information (contained in the directions of propagation k_{out}) is averaged or traced over, and the polarization of the scattered photon is reduced to a mixture. This happens, of course, because the scattering process has coupled the polarization and the spatial degrees of freedom of the light, so that upon detection the spatial degrees of freedom act as a bath. Such transition from pure to mixed polarization state does unavoidably affect the polarization entanglement of light.

In this Thesis we analyzed the degradation of polarization entanglement by different scattering processes, ranging from Rayleigh scattering in multi-mode polymer optical fibers to scattering by fat particles suspended in milk. The reason why we wanted to use different types of scattering media is because each media provides a particular coupling mechanism, which in principle can induce a particular entanglement decay.

Finally, how can we detect this entanglement decay by scattering. A straightforward way would be to measure the visibility after the scattering process, and quantify how much
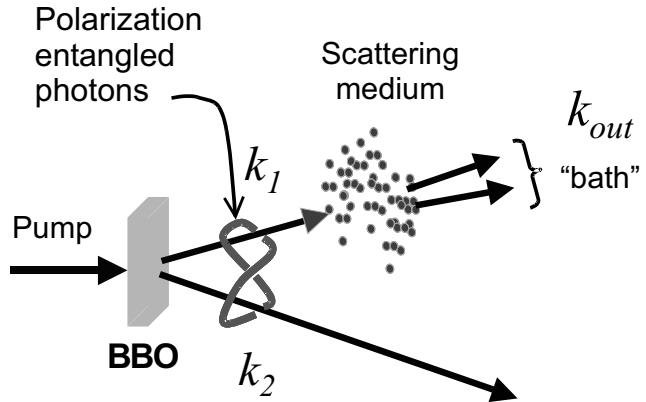
Figure 6: *One photon belonging to a pair of polarization-entangled photons undergoes a multi-mode scattering process. When the scattered photon is detected in a momentum-insensitive way, the spatial degrees of freedom k_{out} act as a bath, and leave the scattered photon in a mixed polarization state.*

it has dropped. Now, a complication can arise since some of the scattering media that we analyzed had polarization anisotropy, for instance birefringence or dichroism. In order to fully quantify the entanglement degradation in these cases, we would have had to measure the visibility in many different polarization basis. A systematic way of doing this is by measuring the 4×4 polarization density matrix of the two photons, by means of a technic called quantum tomography; this is the quantum analogue of CT ('Computed Tomography') medical scan. Different entanglement (and mixedness) measures can then be extracted from the tomographically reconstructed two-photon polarization density matrix. That is indeed the way in which we analyzed our data.

Samenvatting

Deze samenvatting bevat een korte inleiding tot het centrale onderwerp van dit proefschrift, namelijk het verstrooien van verstrengelde fotonen. Het is de bedoeling dat deze samenvatting het onderwerp van dit proefschrift zo toegankelijk mogelijk maakt voor de leek, met als gevolg dat eenvoud in het algemeen een hoge prioriteit heeft gekregen.

Lichtverstrooiing met verstrengelde fotonen: een heuristische benadering

Een lichtbundel die propageert in een homogeen medium volgt een recht pad. Als zich een inhomogeniteit bevindt in dit pad, dan kan het licht daaraan verstrooien. Het belangrijkste effect dat optreedt tijdens verstrooiing, is dat de propagatierichting (of de impuls k) van de lichtbundel verandert (zie Fig. 1). Zo'n inhomogeniteit of verstrooier kan een atoom, een molecuul, een deeltje met een andere brekingsindex (dan van het homogene medium) of een dichtheidsfluctuatie in een vloeistof of gas zijn. Een impulsverandering van het licht door de verstrooier gaat altijd samen met een verandering van de polarisatierichting van het licht, aangezien deze ook een vrijheidsgraad is die loodrecht (transversaal) staat op de impuls k (zoals aangegeven met de kleine transversale pijl in Fig. 1). Verstrooiing waar meerdere
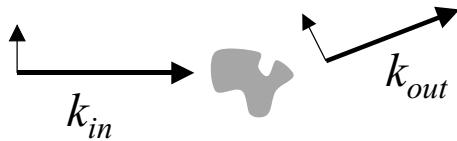
Figuur 1: *Het grootste effect van verstrooiing is dat de propagatierichting van het licht verandert. De polarisatierichting is aangegeven met de kleine transversale pijl.*

propagatierichtingen k bij betrokken zijn, noemen we multi-mode verstrooiing. Bij dit proces is er niet slechts één enkel transversaal vlak waarin het verstrooide licht gepolariseerd is. In dit geval zegt men dat de impuls en de polarisatie van het licht gekoppeld zijn. Dit is dus een voorbeeld van hoe een verstrooiingsproces de polarisatie van het licht kan beïnvloeden.

Een ander voorbeeld is Rayleigh verstrooiing van zonlicht door kleine deeltjes in de atmosfeer (zie Fig. 2). Deze vorm van verstrooiing is niet alleen verantwoordelijk voor de blauwe kleur van de lucht, maar zorgt er ook voor dat zonlicht gedeeltelijk gepolariseerd is. De meeste mensen kennen dit verschijnsel wel door het gebruik van een polaroid zonnebril, die een gedeelte van het verstrooide zonlicht blokkeert. De polarisatie van zonlicht wordt ook door insecten zoals bijen gebruikt om te navigeren, en er wordt zelfs beweerd dat de Vikingen duizend jaar geleden al beschikten over een navigatie systeem dat gebruik maakte van de polarisatie van zonlicht!

Het is nu duidelijk dat verstrooiingsprocessen invloed hebben op de polarisatie vrijheidsgraad van licht. Een voor de hand liggende vraag is wat er zou gebeuren in een verstrooiingsexperiment, wanneer het kwantumkarakter van het licht essentieel is. Een belangrijk voorbeeld van 'kwantum licht' is een verstrengeld fotonpaar. We vragen ons derhalve af wat er zou gebeuren als we een verstrooiingsexperiment zouden uitvoeren met polarisatieverstren-
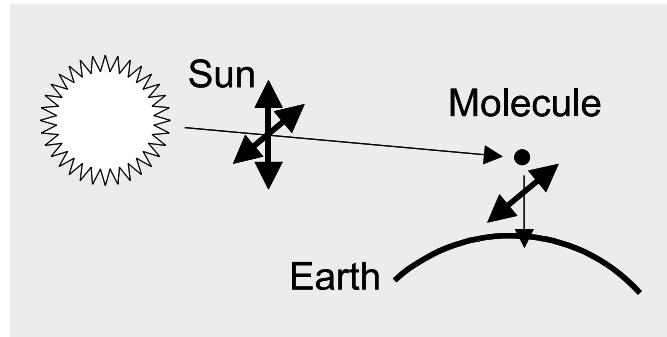
Figuur 2: *Rayleigh verstrooiing door moleculen in de atmosfeer.*

gelde fotonen. Dit is precies de vraag die we willen beantwoorden in dit proefschrift.

Om deze vraag te beantwoorden, bekijken we eerst hoe zo'n polarisatieverstrengeld fotonpaar gemaakt wordt. Zulke fotonparen, ook tweelingfotonen genoemd, kunnen gecreëerd worden in het lab met behulp van spontane parametrische splitsing. Dit is een niet-lineair optisch proces dat plaatsvindt in een speciaal soort kristal, genaamd BBO (van Beta Barium Boraat), waarbij een pompfoton wordt opgesplitst in twee tweelingfotonen met ieder de helft van de originele energie (zie Fig. 3 (a)). Deze twee fotonen (1 en 2 gelabeld) zijn volledig
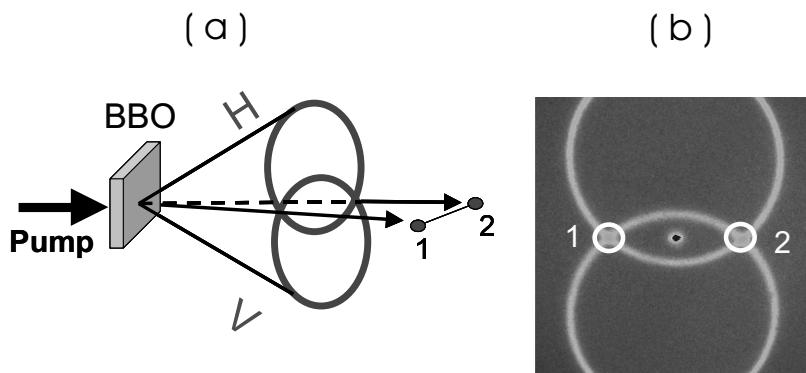
Figuur 3: *(a) Schematische voorstelling van het creatieproces van tweelingfotonen door spontane parametrische splitsing. (b) Verre veld intensiteitspatroon van gesplitste fotonen. De polarisatieverstrengelde fotonparen worden geselecteerd uit de kruisingen van de twee ringen.*

gecorreleerd. Sterker nog, door de manier waarop zij gecreëerd zijn (in het kristal), zijn ze compleet antigecorreleerd, en zouden ze eigenlijk 'anti-tweelingfotonen' genoemd moeten worden! De anticorrelatie is zodanig dat als een van de twee fotonen gepolariseerd is in de

richting P_1, het andere foton van het paar gepolariseerd is in de richting $P_2 \perp P_1$. Dat dit geldt voor elke waarde van P_1, is een intrinsiek niet-klassieke eigenschap van deze correlatie. Deze kwantumcorrelatie van de polarisatievrijheidsgraden van de fotonen wordt polarisatie-verstrengeling genoemd. Merk op dat deze kwantumcorrelatie onafhankelijk is van de afstand tussen de twee fotonen, hetgeen het niet-lokale karakter van de verstrengeling aantoont. De fotonparen die ontstaan bij de splitsing worden uitgezonden in twee elkaar doorsnijdende kegels, die onderling loodrecht gepolariseerd zijn (de ene kegel is bijvoorbeeld verticaal *V* gepolariseerd zodat de andere kegel horizontaal *H* gepolariseerd is). Eenmaal geprojecteerd op een transversaal vlak zien deze twee kegels eruit als twee elkaar snijdende ringen. De polarisatieverstrengelde fotonparen worden geselecteerd uit de kruisingen van deze twee ringen (zie Fig. 3 (b)). Op deze manier hebben de individuele fotonen die vanuit deze kruisingen komen geen vaste polarisatie. Echter, het foton uit de ene kruising vormt een paar met het foton uit de andere kruising en het enige dat vast staat is dat ze in relatie tot elkaar loodrecht gepolariseerd zijn.
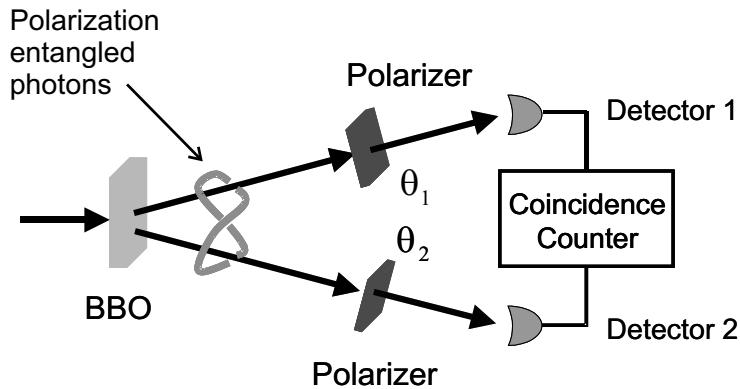
Figuur 4: *Schematische voorstelling van de detectie van polarisatieverstrengeling van tweelingfotonen.*

Hoe kunnen we deze niet-lokale anticorrelatie tussen de polarisatieverstrengelde fotonen detecteren? Een manier om dit te bewerkstelligen is door in het pad van elk foton een lineaire polarisator te plaatsen. De ene polarisator P_1 wordt georiënteerd onder een hoek θ_1 en de andere polarisator P_2 onder een hoek θ_2. Vervolgens worden de fotonen die door te polar-isatoren worden doorgelaten gedetecteerd met behulp van detectoren die aangesloten zijn op een coïncidentiecircuit (zie Fig. 4). Een coïncidentiedetectie wordt geregistreerd wanneer de twee onafhankelijke detectoren (1 en 2 gelabeld) beide gelijktijdig een foton detecteren. In werkelijkheid arriveren de fotonen nooit gelijktijdig bij de corresponderende detector, maar wel binnen een zeer klein tijdsinterval van 2 of 3 nanoseconden. Er rekening mee houdend dat de polarisatie van de twee fotonen anti-parallel is, verwachten we dat we veel coïncidenties detecteren wanneer $\theta_2 \perp \theta_1$ en bijna geen detecteren wanneer $\theta_2 \parallel \theta_1$, en dit zou het geval moeten zijn voor elke willekeurige oriëntatie van P_2 (of P_1). Dit laatste is inderdaad het resultaat van een experiment, getoond in Fig. 5. De verscheidene experimentele curves (zo-

genaamde contrastcurves) corresponderen met een vaste oriëntatie $\theta_2 = 0°$ (vierkanten) en $\theta_2 = 45°$ (cirkels) van polarisator P_2, terwijl de oriëntatie van P_1 gevarieerd wordt. De aanwezigheid van de sterke modulatie in het aantal coïncidenties in beide curven, is karakteristiek voor de polarisatieverstrengeling van de tweelingfotonen.
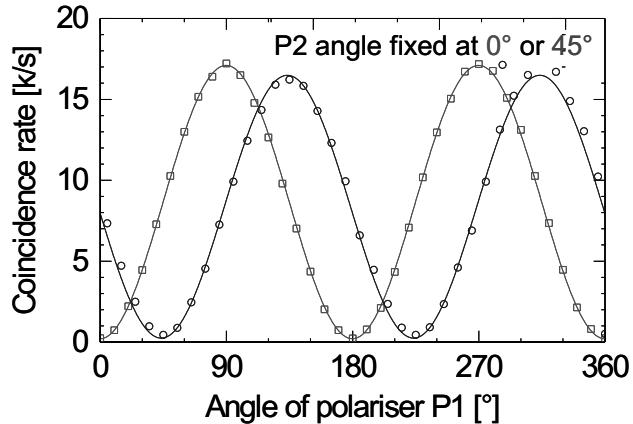
Figuur 5: *Coïncidentiemetingen voor twee vaste instellingen van polarisator P_2, namelijk $\theta_2 = 0°$ (vierkanten) en $\theta_2 = 45°$ (cirkels).*

We weten nu dat verstrooiingsprocessen invloed hebben op de polarisatie van licht, we weten hoe we polarisatieverstrengelde fotonen moeten maken en hoe we de verstrengeling moeten detecteren. We zijn nu dus gereed om de vraag te beantwoorden wat we zouden meten als we een verstrooiingsexperiment zouden uitvoeren met polarisatieverstrengelde fotonen. Stel dat we zo'n verstrengeld fotonpaar creëren. De twee polarisatieverstrengelde fotonen (1 en 2 genoemd) propageren dan met duidelijk gedefinieerde impulsen k_1 en k_2. Vervolgens plaatsen we een verstrooiend medium in het pad van foton 1. We zouden ook een verstrooier kunnen plaatsen in het pad van foton 2, maar dit heeft geen meerwaarde voor het beantwoorden van de vraag. Terwijl foton 1 propageert door het medium, zal het meerdere malen verstrooid worden. Elke verstrooiing verandert de richting van het foton in een superpositie van meerdere impulsen k_{out}, elk met een ander polarisatievlak (zie Fig. 6). Het verstrooiingsproces heeft dus de polarisatie- en impulsvrijheidsgraden van het inkomende foton gekoppeld. Vervolgens detecteren we het verstrooide fotonpaar in coïncidentie, met een detector die ongevoelig is voor de impuls van de fotonen. Hiervoor gebruiken we detectoren met een groot oppervlak, zodat over alle ruimtelijke informatie (over de richtingen k_{out}) wordt gemiddeld (of eigenlijk, zodat het spoor over alle ruimtelijke informatie wordt genomen) en de polarisatietoestand van het verstrooide foton wordt gereduceerd tot een gemengde toestand. Dit gebeurt uiteraard omdat het verstrooiingsproces de polarisatie en impuls heeft gekoppeld zodat bij detectie, de ruimtelijke vrijheidsgraden als bad fungeren. Deze overgang van een zuivere naar een gemengde polarisatietoestand heeft uiteraard invloed op de polarisatieverstrengeling van het licht.
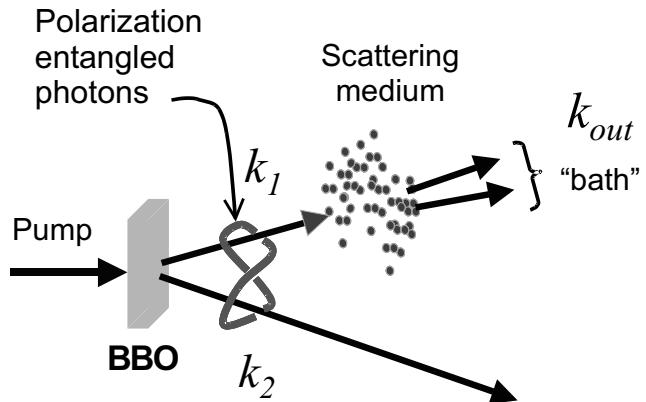
Figuur 6: *Een van de fotonen van een polarisatieverstrengeld fotonpaar ondergaat een multi-mode verstrooiingsproces. Als het verstrooide foton wordt gedetecteerd op een manier die ongevoelig is voor zijn impuls, dan zullen alle ruimtelijke vrijheidsgraden k_{out} fungeren als een bad, zodat de polarisatie van het verstrooide foton vervalt in een gemengde toestand.*

In dit proefschrift onderzoeken we de degradatie van polarisatieverstrengeling bij verschillende verstrooiingsprocessen, van Rayleigh verstrooiing in multi-mode polymeren fibers tot verstrooiing aan vetdeeltjes in melk. Ieder van de gebruikte verstrooiingsmedia heeft een eigen koppelingsmechanisme, dat in principe een specifieke degradatie van verstrengeling teweeg kan brengen.

Tot slot bekijken we dus hoe deze verstrengeling degradeert. Een eenvoudige manier om deze te bestuderen is om na het verstrooiingsproces, het contrast van de coïncidentiecurve te kwantificeren. Hier treedt mogelijk een complicatie op, aangezien enkele van de verstrooiers polarisatieanisotropie vertonen, zoals dubbelbrekendheid of dichroisme. Om de degradatie van verstrengeling in die gevallen volledig te kwantificeren, zouden we het contrast moeten meten in vele, verschillende polarisatiebases. Een systematische manier om dit te bewerkstelligen is door het meten van de 4×4 polarisatie dichtheidsmatrix van het fotonpaar, volgens een techniek die bekend staat als kwantumtomografie; dit is een kwantum analogon van de medische CT ('Computed Tomography') scan. Verschillende maten van verstrengeling (en gemengdheid) kunnen dan worden bepaald uit deze tomografisch gereconstrueerde dichtheidsmatrix. Dit is ook de manier waarop wij onze data hebben geanalyseerd.

List of publications

- **Optical simulation of quantum algorithms using programmable liquid crystal displays**
  G. Puentes, C. La Mela, S. Ledesma, C. Iemmi, J. P. Paz, and M. Saraceno, Phys. Rev. A **69**, 42319 (2004).

- **Ray splitting in paraxial optical cavities**
  G. Puentes, A. Aiello, and J. P. Woerdman, Phys. Rev. E **69**, 036209 (2004).

- **Chaotic ray dynamics in an optical cavity with a beam splitter**
  G. Puentes, A. Aiello, and J. P. Woerdman, Opt. Lett. **29**, 929 (2004).

- **Experimental observation of universality in depolarized light scattering**
  G. Puentes, D. Voigt, A. Aiello, and J. P. Woerdman, Opt. Lett. **30**, 3216 (2005).

- **Maximum-likelihood estimation of Mueller matrices**
  A. Aiello, G. Puentes, D. Voigt, and J. P. Woerdman, Opt. Lett. **31**, 817 (2006).

- **Tunable spatial decoherers for polarization-entangled photons**
  G. Puentes, D. Voigt, A. Aiello, and J. P. Woerdman, Opt. Lett. **31**, 2057 (2006).

- **Entangled mixed-state generation by twin-photon scattering**
  G. Puentes, A. Aiello, D. Voigt, and J. P. Woerdman, Phys. Rev. A **75**, 032319 (2007).

- **Maximally entangled mixed-state generation via local operations**
  A. Aiello, G. Puentes, D. Voigt, and J. P. Woerdman, quant-ph/0603182 (submitted to Phys. Rev. A).

- **Linear optics and quantum maps**
  A. Aiello, G. Puentes, and J. P. Woerdman, quant-ph/0611179 (submitted to Phys. Rev. A).

- **Twin-photon light scattering and causality**
  G. Puentes, A. Aiello, and J. P. Woerdman (to appear in Proceedings of the conference "Beyond the Quantum" held at Lorentz Institute, Leiden University, The Netherlands, June 2006); to be published by World Scientific (Singapore).

Curriculum Vitae

I was born the 3rd of January of 1977 in Buenos Aires (Argentina). I started my undergraduate Physics studies in March 1996, at the University of Buenos Aires (UBA). In September 2002, I completed my 'Licenciado' Thesis (equivalent to a Master's Thesis) at UBA, working on the theory of quantum algorithms and quantum maps under the supervision of Professors M. Saraceno and J. P. Paz. This work allowed me to finish my Master's studies with a honors degree. After this, I received a six month grant to join the Imaging Processing Laboratory at UBA, where I investigated experimental optical implementations of quantum algorithms. On April 2003, I was employed by the 'Stichting voor Fundamenteel Onderzoek der Materie' (FOM) to do my PhD research work at the Quantum Optics and Quantum Information Group directed by Professor J. P. Woerdman, in Leiden University (The Netherlands). For the first year of my graduate studies, I worked on the theory of chaotic optical cavities, and for the last three years, I worked on light scattering experiments with entangled photons. During my PhD, I attended three international summer schools: 'Quantum Logic and Communications'-France (2004), 'Quantum Computers, Algorithms and Chaos'-Italy (2005) and 'ICAP06'-Austria (2006). I also presented talks at: Veldhoven and Lunteren (The Netherlands), Imperial College and Oxford University (UK), University of Innsbruck (Austria) and ICFO-Barcelona (Spain). Additionally, during my PhD years, I worked as a teaching assistant in an undergraduate course on Quantum Mechanics and in a Master's level course on Quantum Theory, at Leiden University.

As of July 2007, I have been appointed as a Postdoctoral Research Assistant at Oxford University (UK), in the group of Professor I. Walmsley.

Acknowledgements